Chem Soc Rev

REVIEW ARTICLE

View Article Online
View Journal | View Issue

Cite this: *Chem. Soc. Rev.*, 2026, **55**, 3687

Heteroatom doping in carbon macrocycles for advanced synthesis and applications

Chao Liu,[a] Shuangyi Li,[a] Xin Chen,[a] Tonglin Yang,[a] Ying Wei,*[a] Linghai Xie,*[ab] Erik V. Van der Eycken*[cd] and Wei Huang*[abe]

Received 11th November 2025

DOI: 10.1039/d5cs01268f

rsc.li/chem-soc-rev

Macrocycles have garnered significant research interest due to their tunable structures, unique physicochemical properties, and broad range of applications in areas such as aggregation-induced emission (AIE), molecular recognition, bioimaging, and photocatalysis. While conventional carbon-rich macrocycles depend mainly on ring-size adjustments for property modulation, the incorporation of heteroatoms (N, O, and S) allows precise control over electronic structure, band gap, and functionality. This review summarizes recent advances (2020–2025) in the synthesis and applications of heteroatom-doped (N-, O-, S-, N,O-, and N,S-doped) macrocycles. It covers metal-catalyzed (Pd, Ni, Pt, Cu, Ti, Sn, and Fe) and metal-free (acidic/basic) strategies, post-synthetic modifications, and emerging applications in host–guest systems, sensors, OLEDs, OFETs, OPVs, and (photo)catalysis, aiming to advance the field and serve as a reference for cross-disciplinary researchers.

[a] *Center for Molecular Systems & Organic Devices (CMSOD), State Key Laboratory of Flexible Electronics (LoFE) & Institute of Advanced Materials (IAM), Nanjing University of Posts & Telecommunications, Nanjing 210023, China. E-mail: iamywei@njupt.edu.cn, iamlhxie@njupt.edu.cn*

[b] *School of Flexible Electronics (SoFE) and Henan Institute of Flexible Electronics (HIFE), Henan University, Zhengzhou 450046, China*

[c] *Laboratory for Organic & Microwave-Assisted Chemistry (LOMAC), Department of Chemistry, University of Leuven (KU Leuven), Leuven, Belgium. E-mail: erik.vandereycken@kuleuven.be*

[d] *Department of Organic Chemistry, Peoples' Friendship University of Russia (RUDN University), Miklukho-Maklaya street 6, Moscow 117198, Russia*

[e] *Frontiers Science Center for Flexible Electronics (FSCFE), MIIT Key Laboratory of Flexible Electronics (KLoFE), Northwestern Polytechnical University, Xi'an 710072, China. E-mail: iamwhuang@nwpu.edu.cn*

1. Introduction

Macrocycles have attracted wide research interest owing to their versatile chemical modifications, outstanding physicochemical properties, and distinctive ring architectures.[1–4] These remarkable structures have demonstrated diverse applications in aggregation-induced emission (AIE),[5] molecular recognition,[6] molecular machines,[7] bioimaging,[8] chemical sensing,[9] drug delivery,[10] and photocatalysis.[11] Therefore, various approaches have been developed for the synthesis of new macrocycles. This has not only promoted the advancement of organic chemistry but also driven the development of materials science.

Chao Liu

Chao Liu obtained his MSc degree in chemistry from Soochow University in 2019. He received his PhD degree in organic chemistry from the University of Leuven (KU Leuven) in 2022, under the supervision of Professor Erik V. Van der Eycken. He finished his post-doctoral research in the same group in 2023. Currently, he is an associate professor at the Nanjing University of Posts and Telecommunications in China. He is working in the area of transition metal catalysis, heterocyclic chemistry and macrocycles.

Ying Wei

Ying Wei received her PhD degree from Northeast Normal University in 2014. She then joined the Key Laboratory for Organic Electronics & Information Displays and Institute of Advanced Materials (IAM), Nanjing University of Posts & Telecommunications. Currently, she is an associate professor at the Nanjing University of Posts and Telecommunications. Her research mainly focuses on the design, synthesis, and applications of organic and polymer optoelectronic materials for organic/plastic electronics.

In 1970s, calixarenes were first named and characterized by Gutsche.[12] Thereafter, various crown-ethers,[13] pillararenes,[14,15] cucurbiturils,[16] and cyclodextrins (CDs),[17] all exhibiting unique characteristics in host–guest chemistry and materials science, were also reported. Among these, carbon-rich macrocycles derived from benzene or polycyclic aromatic hydrocarbon (PAH) units primarily regulate their properties by adjusting the size of the macrocyclic rings.[18] However, this reliance on ring-size tuning significantly limits the further application and development of these materials. Subsequently, main-group elements, including sulfur (S), boron (B), oxygen (O), and nitrogen (N), have been extensively incorporated into macrocyclic frameworks to create functional molecules and broaden applications.[19] By varying the type, count, and spatial arrangement of heteroatoms, this strategy allows for fine-tuning of the electronic structure and highest occupied molecular orbital (HOMO)–lowest unoccupied molecular orbital (LUMO) band gap, thereby enabling systematic modulation of macrocycle properties.[1,2] For instance, N doping can lower the LUMO energy level, while B incorporation can significantly modulate absorption and emission profiles, thereby tailoring optoelectronic properties for specific applications. Moreover, heteroatoms (*e.g.*, N, O, and S) serve as critical handles for introducing rich non-covalent interactions. For example, N and O atoms enable directional hydrogen bonding and metal-ion coordination, while the S atom not only participates in coordination but also engages in directional chalcogen-bonding interactions (*e.g.*, S···S). However, compared to all-carbon macrocycles, the synthesis of heteroatom-containing macrocycles presents several distinct challenges.[3] For example, the precise control over the heteroatom type, number, and position during monomer design often leads to regioisomeric mixtures. The heteroatoms themselves can act as reactive sites that poison catalysts or promote side reactions during critical cyclization steps, significantly reducing yields. Additionally, managing the solubility and stability of sensitive intermediates requires precise condition control, and final purification often demands advanced techniques such as recycling gel-permeation chromatography (GPC). Notably, incorporating boron atoms into calixarenes, pillararenes, and crown-ether scaffolds has enabled the synthesis of various boron-doped macrocycles for diverse applications. These derivatives demonstrate distinct guest–recognition capabilities and unprecedented catalytic functions compared to their all-carbon analogues, as thoroughly summarized by Lu *et al.* in a recent review.[20] Furthermore, as reviewed by Yang,[21] borondipyrromethene (BODIPY)-based macrocycles applied in sensing, bioimaging, and photodynamic therapy show that alterations in macrocyclic linking units significantly modulate their photophysical behaviors, geometric properties, and practical applications.

This review will highlight the advances made in recent years (2020–2025) in the synthesis and applications of heteroatom-

Linghai Xie

Linghai Xie is a full professor at the Nanjing University of Posts and Telecommunications. He received his PhD from Fudan University in 2006. He then joined the Key Laboratory for Organic Electronics & Information Displays and Institute of Advanced Materials (IAM), Nanjing University of Posts & Telecommunications. His research mainly focuses on the design, synthesis, and applications of organic and polymer optoelectronic materials for organic/plastic electronics. He is also interested in the exploration of novel materials and processes for molecular electronics.

Erik V. Van der Eycken

Erik V. Van der Eycken received his PhD degree (1987) in organic chemistry from the University of Ghent, under the supervision of Professor Maurits Vandewalle. From 1988 to 1992 he worked as a scientific researcher at the R&D laboratories of AGFA-Gevaert, Belgium and moved back to the University of Ghent in 1992. In 1997 he became a Doctor Assistant at the University of Leuven (KU Leuven). He spent time as a visiting scientist at the University of Graz (C. Oliver Kappe), at The Scripps Research Institute (K. Barry Sharpless), and at Uppsala University (Mats Larhed, Anders Hallberg). He was appointed Professor at the University of Leuven (KU Leuven) in 2007 and is presently a Full Professor.

Wei Huang

Wei Huang received his PhD from Peking University in 1992. In 2001, he was appointed as a chair professor at Fudan University, where he founded and chaired the Institute of Advanced Materials (IAM). After that he became the vice president of Nanjing University of Posts & Telecommunications and then the president of Nanjing Tech University. He was elected as an Academician of the Chinese Academy of Sciences in 2011. His research interests include organic/plastic/flexible electronics, nanomaterials, nanotechnology, etc.

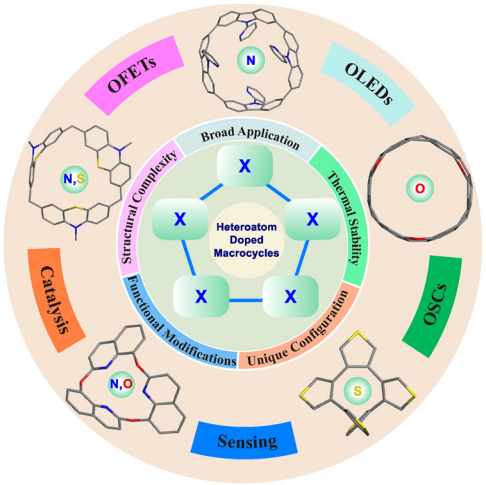

Fig. 1 Synthesis and applications of heteroatom-doped macrocycles.

doped (*e.g.*, N-, O-, S-, N,O-, and N,S-doped) macrocycles, while excluding less common types such as phosphorus-doped systems, because their synthetic methodologies and demonstrated applications remain limited (Fig. 1). Metal-catalyzed macrocyclization reactions using catalysts such as Pd, Ni, Pt, Cu, Ti, Sn, and Fe for constructing diverse macrocyclic scaffolds will be presented. Metal-free strategies, including acidic (Lewis and Brønsted acids) and basic conditions, for the synthesis of heteroatom-doped macrocycles, are also emphasized. Further transformations to access novel macrocycles will also be highlighted. Finally, their applications in host–guest chemistry, sensing, organic light-emitting diodes (OLEDs), organic field effect transistors (OFETs), (photo)catalysis, and organic solar cells (OSCs) will be introduced. We believe that this review will pave the way for new advancements in heteroatom-doped macrocycles and serve as a valuable resource for researchers in chemistry, materials science, biology, and related disciplines.

2. N-doped macrocycles

Classical N-doped macrocycles, including porphyrins, phthalocyanines, cyclens, and calixpyrroles, exhibit promising applications across multiple disciplines. Porphyrins and phthalocyanines are aromatic macrocycles with pyrrole rings, enabling metal coordination critical for biological functions and modern applications in catalysis, photodynamic therapy, and light-harvesting materials.[22,23] Cyclen, a tetraazamacrocycle bearing four N-atoms for versatile functionalization, has emerged as a pivotal scaffold for constructing artificial nucleases and biological nucleotide sensors, enabling precise manipulation and detection of nucleic acids.[24] Calixpyrroles, with flexible, bowl-shaped cavities, have roles as neutral/monoanionic ligands for metal coordination and anion recognition, with hybrid structures facilitating applications in catalysis and supramolecular chemistry.[25] Recent advancements in synthetic methods allow precise construction of functionalized N-doped macrocycles, controlling the ring size, substitution patterns, and heteroatom integration to create complex, tailored frameworks for diverse applications.[26,27]

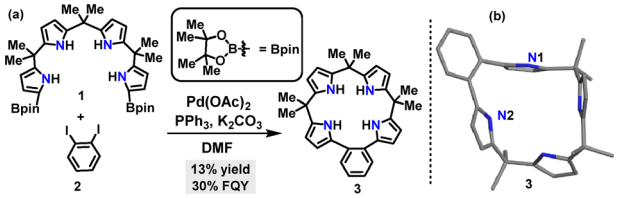

Scheme 1 (a) Synthesis and (b) crystal structure of calix[4]pyrrole **3**.

2.1. Metal catalysis

2.1.1. Palladium catalysis. In 2021, Panda's group synthesized calix[4]pyrrole **3** in 13% yield *via* a palladium-catalyzed [1+1] Suzuki coupling reaction between the diborylated tetrapyrrane **1** and 2-diiodobenzene **2** (Scheme 1a).[28] Crystal structure analysis revealed that macrocycle **3** adopted a slightly irregular 1,3-alternate conformation (Scheme 1b). The N1-linked pyrrole unit, connected to the *o*-phenylene spacer, displayed near-orthogonal geometry relative to the benzene ring plane (dihedral angle: 81°), whereas the N2-linked pyrrole unit exhibited a more coplanar arrangement (dihedral angle: 26°), suggesting potential for extended π-conjugation.

In the same year, Yasuda reported an efficient method to synthesize a thermally activated delayed fluorescence (TADF) π-conjugated macrocycle incorporating electron-donor (D) and acceptor (A) units (Scheme 2a).[29] Macrocycle **6** was obtained in 18% yield *via* a palladium-catalyzed Suzuki–Miyaura cross-coupling reaction. The photoluminescence (PL) peak wavelengths (λ_{PL}) of macrocycle **6** exhibited a bathochromic shift in intramolecular charge transfer (ICT) absorption compared to linear **7** (Scheme 2b). Upon photoexcitation, macrocycle **6** emitted green PL at 496 nm (λ_{PL}), while **7** produced deep-blue PL at 468 nm (Scheme 2c). Owing to its rigid macrocyclic structure, macrocycle **6** displayed a smaller full width at half-maximum in its PL spectrum and lower reorganization energy than linear **7**. Notably, macrocycle **6** achieved a 77% absolute photoluminescence quantum yield (PLQY) in toluene, surpassing **7**'s 49%, attributed to its TADF characteristics.

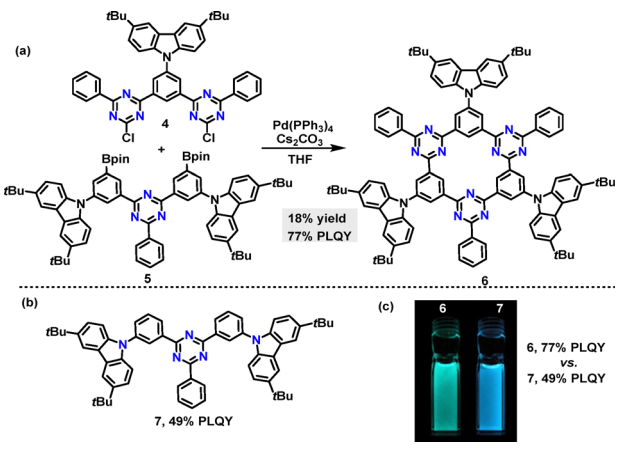

Scheme 2 (a) Synthesis of TADF π-conjugated macrocycle **6**, (b) structure of linear **7**, and (c) photograph of PL emissions under UV illumination at 365 nm. Adapted from ref. 29 with permission from Wiley-VCH, copyright 2021.

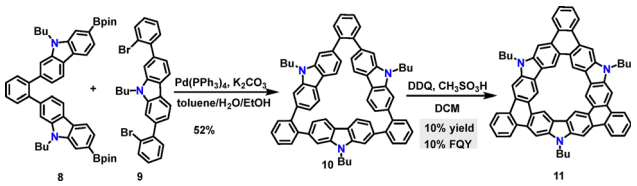

Scheme 3 Synthesis and modification of carbazole-fused macrocycle **10**.

Later, Miao and co-workers reported a Suzuki coupling reaction between substrates **8** and **9**, which afforded the carbazole-fused macrocycle **10** in 52% yield (Scheme 3).[30] Under DDQ/CH_3SO_3H conditions, the fused macrocycle **11** was obtained in 10% yield *via* a regioselective Scholl reaction at the C-3 position of the carbazole moiety. Computational studies revealed significant bond-length alternation in the bowl structure of macrocycle **11**, which was attributed to structural strain (34.7 kcal mol^{-1}) and localized aromaticity. As an orange solid, macrocycle **11** dissolved in dichloromethane (DCM) to form a yellow solution that exhibited green fluorescence under UV irradiation, with a measured FQY of 10%.

In 2023, Toyota[31] reported two synthetic routes for acridone-incorporated arylene-ethynylene macrocycles **14** utilizing palladium catalysis (Scheme 4a). Macrocycle **14a**, featuring three acridone-2,7-diyl units and three 1,3-phenylene units, was synthesized *via* Sonogashira coupling of **12** and **13** with a 15% yield. To streamline the synthesis, alternative monomeric precursors were explored, affording **14b** in 9.9% and **14c** in 3.4% yields. Crystal structure analysis confirmed that the trimeric macrocycle **14b** adopted a near-planar framework with a cavity defined by three carbonyl groups (Scheme 4b).

Subsequently, D–A conjugated macrocycle **19** was synthesized in 2% yield by Jiang *via* a one-step Suzuki coupling reaction of 2,8-dibromophenazine **17** and 3,5-diborate-*N*,*N*-dihexylaniline **18** (Scheme 5).[32] The synthetic yield was relatively low due to the formation of numerous by-products, such as linear polymers and oligomers. Notably, macrocycle **19** exhibited a remarkable Stokes shift of 12 422 cm^{-1} (361 nm) in DCM, with ultraviolet (UV) absorption at 388 nm and near-infrared (NIR) emission at 749 nm.

In 2023, Lu[33] synthesized conjugated macrocycles **22** (20%) and **24** (7%) containing four carbazole units, *via* Suzuki

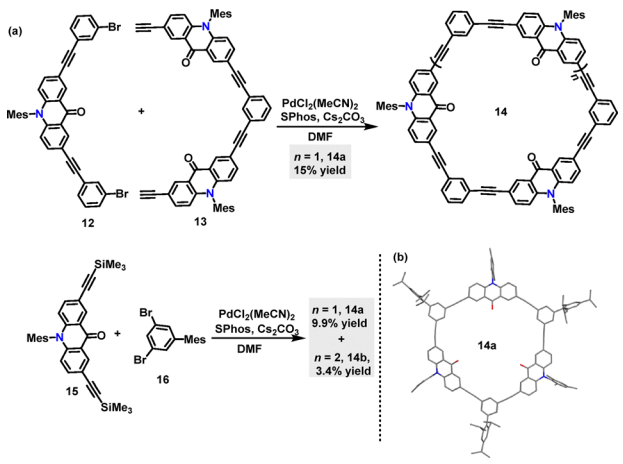

Scheme 4 Synthesis of macrocycles **14** and the crystal structure of **14a**.

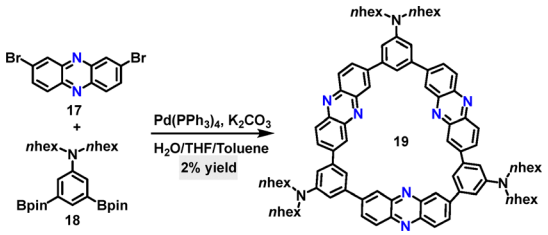

Scheme 5 Synthesis of D–A conjugated macrocycle **19**.

coupling reactions. Macrocycle **24** could be further transformed into the π-conjugated species **26** *via* a Wittig reaction and $Bi(OTf)_3$-mediated cyclization process (Scheme 6a). Crystal structure analysis revealed that **22** adopted a herringbone packing motif without π–π overlap between adjacent molecules (Scheme 6b). In contrast, although **25** also exhibited a herringbone packing motif, it featured effective π–π stacking (Scheme 6c). Thermogravimetric analysis (TGA) revealed that both **22** and **25** exhibited high thermal stability, with 5% weight loss decomposition temperatures exceeding 350 °C (Scheme 6d). UV-vis absorption spectra indicated that **25** displayed a red-shifted absorption (314 nm) compared to **22** (303 nm), along with a narrowed optical bandgap (Scheme 6e). Additionally, **25** exhibited a higher PLQY (12.9% *vs.* 5.6% for **22**) and a longer fluorescence lifetime (10.8 ns *vs.* 4.5 ns for **22**), which were ascribed to reduced nonradiative decay due to its structural rigidity.

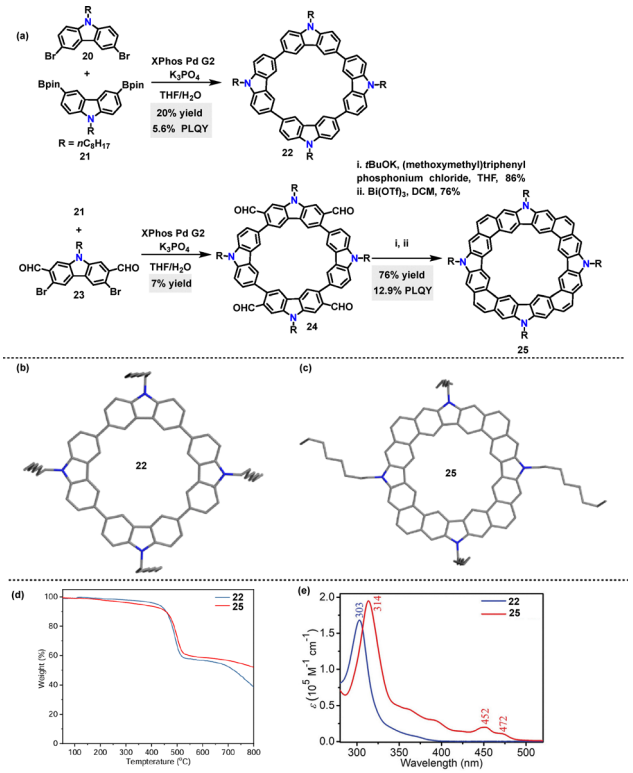

Scheme 6 (a) Synthesis of macrocycles **22**, **24**, and **25**, (b) and (c) crystal structures of **22** and **25**, (d) TGA curves of macrocycles **22** and **25**, and (e) absorption spectra of macrocycles **22** and **25** in DCM. Adapted from ref. 33 with permission from Wiley-VCH, copyright 2023.

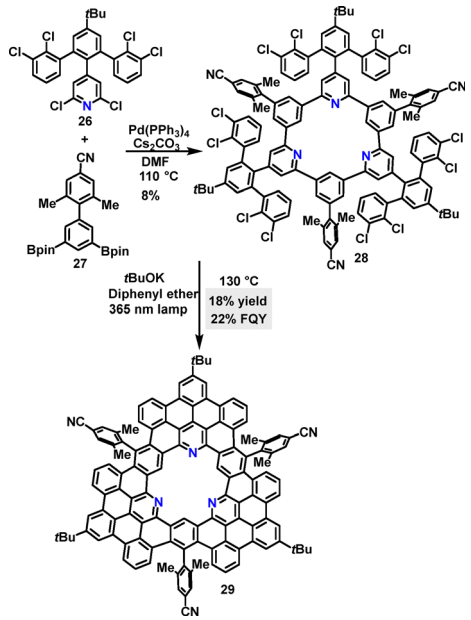

Scheme 7 Synthesis and modification of tri-*N*-containing macrocycle **28**.

Following the same strategy, Tan synthesized the tri-*N*-containing macrocycle **28** in 8% yield *via* a palladium-catalyzed cross-coupling reaction (Scheme 7).[34] Macrocycle **28** was further transformed into nanographene **29**, featuring a central *N*-containing cavity in 18% yield under 365 nm LED irradiation. DFT simulations revealed that **29** adopted a twisted propeller-shaped molecular conformation due to the steric hindrance of the 4-cyano-2,6-dimethylphenyl group. Macrocycle **29** exhibited a FQY of 22% and a lifetime of 7.6 ns.

In 2024, Chen[35] reported a palladium-catalyzed cross-coupling reaction, enabling the preparation of the achiral biscyclic **32** and chiral **33** in 11% and 8% yields, respectively (Scheme 8). According to DFT calculations, the two tetracyclic carbazole moieties are oriented nearly orthogonally, displaying a highly symmetric geometry. In contrast, **33**, featuring a 2,2′,7,7′-substituted bicarbazole core, can't achieve perpendicular rotation due to increased steric constraints and electronic repulsion. Instead, the molecule adopted a figure-eight conformation. Compared to **32** with an absorption maximum of 302 nm and a FQY of 13%, the figure-of-eight biscyclic **33** exhibits a red-shifted absorption maximum (311 nm) and a higher FQY (32%), which can be attributed to enhanced conjugation in the carbazole-phenyl-bridged **33** framework. Additionally, the circularly polarized luminescence (CPL) brightness of **33** was quantified as 26.0 M^{-1} cm^{-1}.

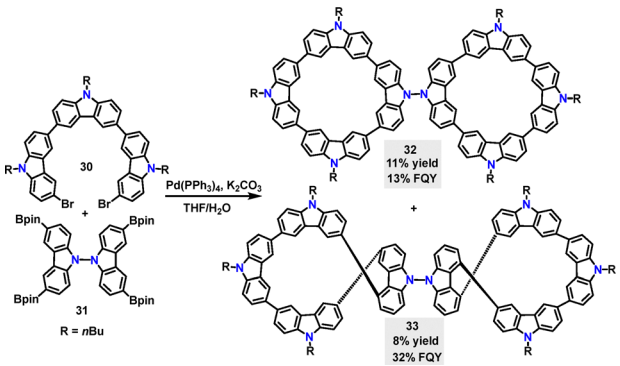

Scheme 8 Synthesis of achiral biscyclic macrocycle **32** and chiral macrocycle **33**.

Recently, Tang[36] designed and synthesized an AIE-active macrocycle **36** incorporating triphenylamine (TPA) and carbazole (Cz) units. The desired product **36** was generated in 8% yield *via* a palladium-catalyzed Suzuki coupling of **34** and **35** (Scheme 9a). DFT calculations revealed that **36** adopted a highly twisted conformation, where the torsion angle was significantly enhanced by the *ortho*-methyl group, thereby promoting AIE characteristics. The HOMO of **36** was localized on the TPA unit, whereas the LUMO was distributed over the phenylcyano group (Scheme 9b). This spatial separation ensured efficient charge separation and facilitated energy transfer processes. Moreover, both **34** and **36** exhibited AIE properties, with enhanced fluorescence intensity in THF/H_2O mixtures. Superior photocatalytic performance was demonstrated by ALHS **36** in mediating cross-dehydrogenative coupling (CDC) reactions within an aqueous environment (Scheme 9b).

Beyond C–C coupling reactions, C–N bond formation reactions have also witnessed remarkable advancements in the synthesis of macrocycles. In 2020, Minakata[37] disclosed a palladium-catalyzed C–N coupling strategy to synthesize dibenzo[*a*,*j*]phenazine-based π-conjugated macrocycle **43**, in 45% yield (Scheme 10a). Macrocycle **43** incorporated two U-shaped electron-accepting cores (dibenzo[*a*,*j*]phenazine) and two electron-donating units

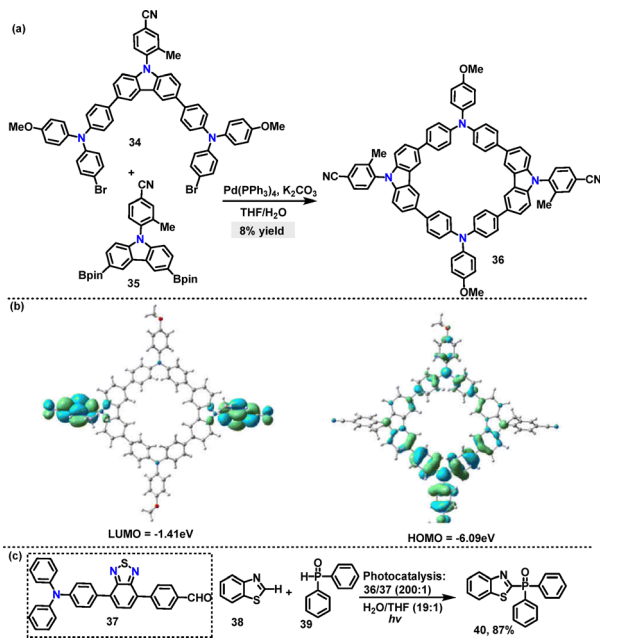

Scheme 9 (a) Synthesis, (b) molecular orbital, and (c) photocatalytic activity of AIE-active macrocycle **36**. Reproduced from ref. 36 with permission from The Royal Society of Chemistry, copyright 2025.

(*N*,*N*′-diphenyl-*p*-phenylenediamine) and displayed emission behaviors and structural conformations influenced by polymorphism. Steady-state spectroscopy revealed that macrocycle **43** exhibited solvent-dependent emission, displaying green fluorescence in cyclohexane (Em: 540 nm, PLQY: 31%) and orange fluorescence in toluene (Em: 595 nm, PLQY: 28%). In contrast, linear **44** showed broader emission with a larger red shift (Em: 615 nm in toluene, PLQY: 20%), which was attributed to its conformational flexibility (Scheme 10b). Degassed solutions of **43** exhibited a 66% increase in emission intensity compared to aerated conditions, indicating significant delayed fluorescence (DF), whereas linear **44** showed only a 24% intensity increase.

In 2021, Giuseppone[38] reported a palladium-catalyzed intermolecular coupling reaction to synthesize an S_6-symmetric triarylamine-based macrocycle **47** in 87% yield (Scheme 11). Upon treatment with trifluoroacetic acid (TFA), this product underwent PMB deprotection to afford macrocycle **48** in 87% yield. Optoelectronic property studies revealed that macrocycle **48** exhibited a red-shifted absorption maximum (343 nm), compared to its protected counterpart **47** (331 nm), primarily attributed to electronic inductive effects arising from the conversion of tertiary amides to secondary amides. Additionally, unbound amide side chains on macrocycle **48** enable its supramolecular polymerization, forming an axially aligned nanotubular architecture with π–π stacking interactions between phenyl rings of adjacent macrocycles along the elongation direction.

Recently, the synthesis of azaparacyclophanes **50** was developed by Bonifazi *via* palladium-catalyzed Buchwald–Hartwig macrocyclization.[39] Diverse monomers carrying aromatic moieties, electron-donating or -withdrawing groups, and other functional groups like pinacol boronates worked well, generating the

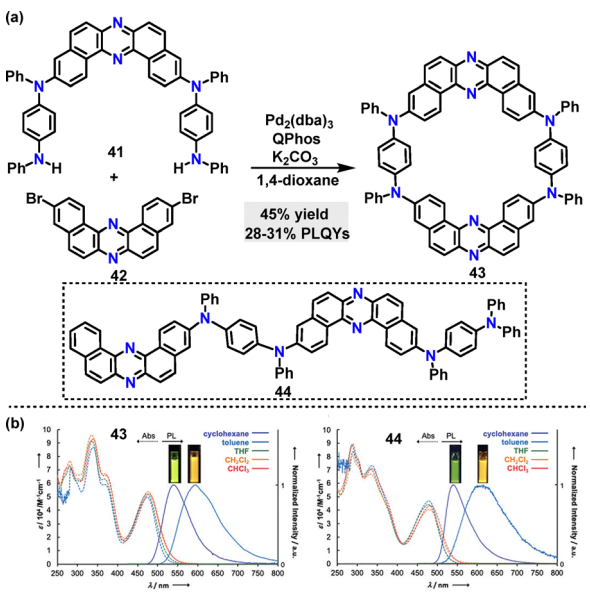

Scheme 10 (a) Synthesis of π-conjugated macrocycle **43** and (b) steady-state UV-vis absorption (Abs) and photoluminescence (PL) spectra of dilute solutions (purple, cyclohexane; sky blue, toluene; green, THF; orange, DCM; red, $CHCl_3$) of compounds **43** and **44**. Adapted from ref. 37 with permission from American Chemical Society, copyright 2020.

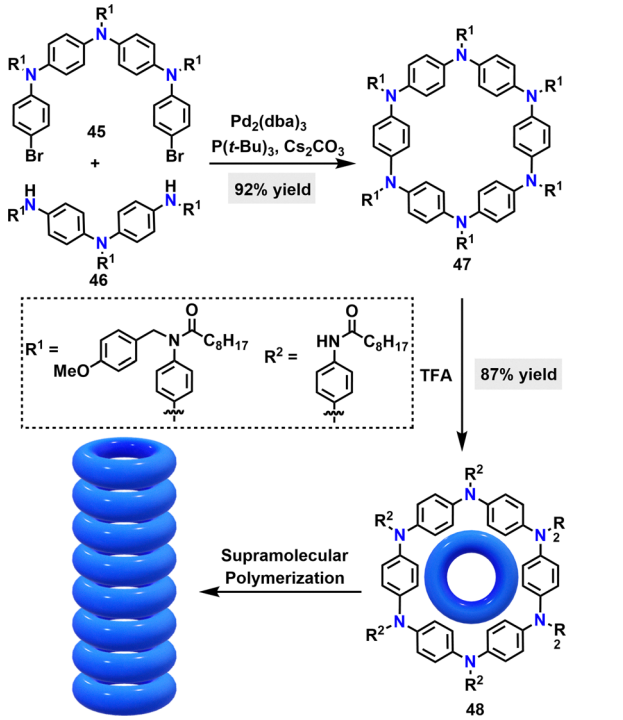

Scheme 11 Synthesis of π-conjugated macrocycles **47 and 48** and supramolecular polymerization of **48**.

desired products **50** in 68–98% yields under mild reaction conditions (Scheme 12a). It was discovered that monomers bearing fused biphenyl endocyclic moieties like fluorene mainly yield 4-membered rings. The monomers bearing a carbazole moiety give a mixture of 4-, 5-, and 6- membered rings. Crystal structure analysis showed that **50a** and **50b** had a six-membered ring structure with endocyclic aryl moieties in a propeller-type conformation and coplanar N-atoms. Compound **50c** displayed a four-membered square macrocycle structure with a specific conformation of the fluorene/carbazole units and coplanar N-atoms (Scheme 12b). Spectroscopic measurements showed that all compounds **50** had similar absorption ranges of 344–393 nm.

2.1.2. Nickel catalysis. In 2021, Huang[40] synthesized a cyclic tetracarbazole **52** in 19% yield *via* a one-pot Yamamoto coupling of a dibrominated carbazole monomer **51** (Scheme 13a). Under identical conditions, **52** exhibited more efficient ultralong phosphorescence with a phosphorescence lifetime (τ_p) of 3.41 ms, surpassing both monomer **53** (τ_p: 1.45 ms) and its linear conjugate **54** (τ_p: 2.24 ms) (Scheme 13b). DFT and time-dependent (TD)-DFT calculations revealed that linear conjugation increased the number of intersystem crossing (ISC) channels, whereas cyclization further reduced the energy gap between singlet and triplet states (ΔE_{ST}) and fostered a more rigid molecular structure.

In 2024, a nanohoop incorporating a stereogenic Tröger's base skeleton was developed by Saito.[41] The Ni(0)-mediated Yamamoto coupling reaction of ***rac*-55a** and **(*S*,*S*)-55b** monomers afforded the cyclization products ***rac*-56a** and **(*S*,*S*)-56b** in 50% and 67% yields, respectively (Scheme 14a). Deprotection of ***rac*-56a** and **(*S*,*S*)-56b** with *n*-BuNF, followed by reductive aromatization promoted by $SnCl_2$ and HCl, yielded ***rac*-57a** and

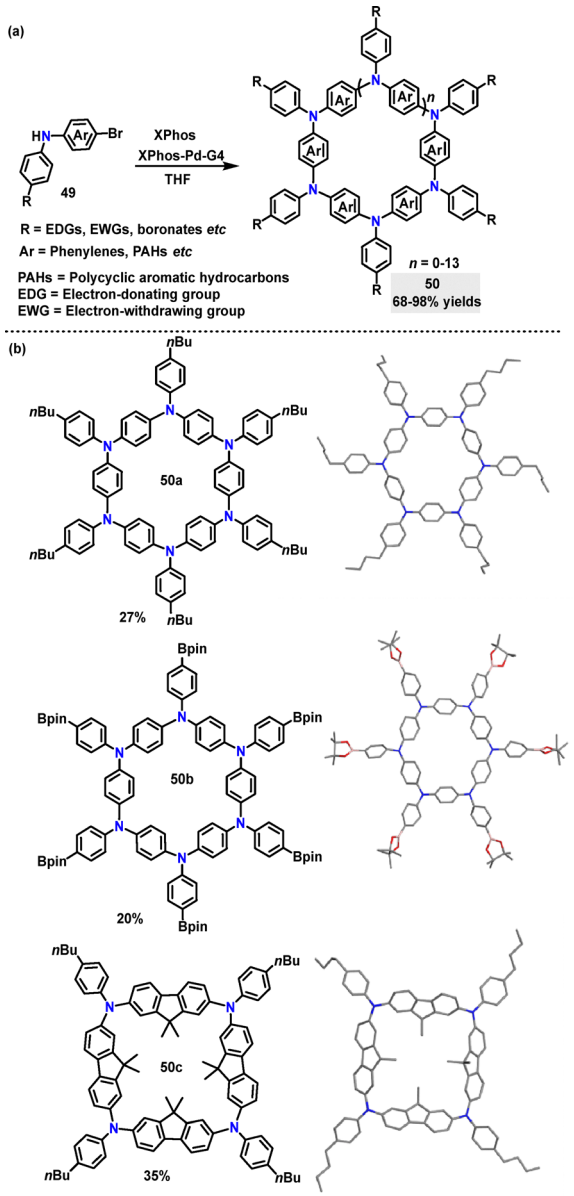

Scheme 12 (a) Synthesis of azaparacyclophane **50** and (b) crystal structures of **50a and b**.

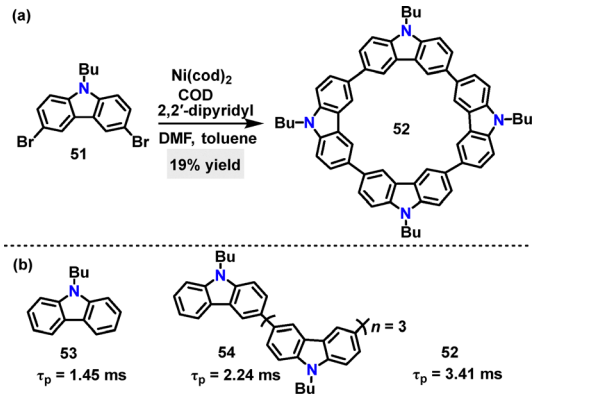

Scheme 13 (a) Synthesis of cyclic tetracarbazole **52** and (b) phosphorescence lifetime (τ_p) of cyclic tetracarbazole **52**, monomer **53**, and linear conjugate **54**.

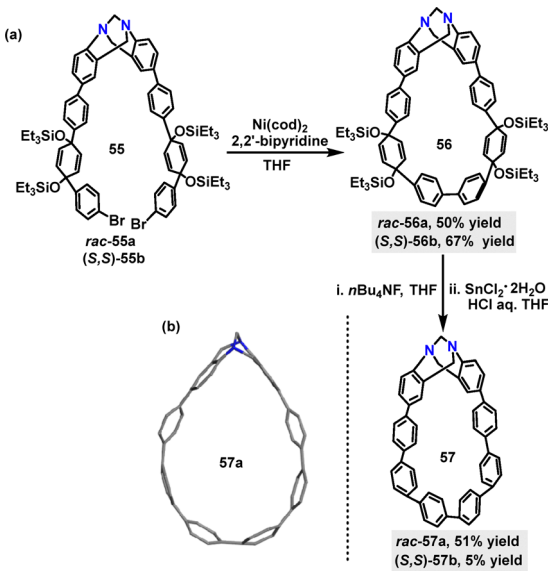

Scheme 14 (a) Synthesis of **56** and **57** and (b) crystal structure of **57a**.

(***S*,*S*)-57b** in 51% and 5% yields respectively. Crystal structure analysis showed that ***rac*-57a** adopted a teardrop-like structure owing to the V-shaped Tröger's base moiety, where the dihedral angle between the two phenylene rings of the Tröger's base unit measures 90° (Scheme 14b).

2.1.3. Platinum catalysis. In 2024, Poriel and Quinton[42] reported the synthesis of three nanohoops in 5% to 61% yields *via* a platinum-catalyzed cyclization, followed by reductive elimination (Scheme 15a). Crystal structures showed that the pyrimidine substituent in **59c** was nearly coplanar with the carbazole moiety, due to hydrogen-bonding interactions, whereas the pyridine group in **59b** exhibited reduced coplanarity (Scheme 15b). The dihedral angles between carbazole and substituents also differ significantly, affecting π-conjugation and electronic properties. UV-vis absorption spectra of the three nanohoops indicated that substituents profoundly influence absorption bands and transition characteristics (Scheme 15c). For example, the absorption maximum undergoes a blue shift from 341 nm in **59a** to 335 nm and 330 nm in **59b** and **59c**, respectively. In emission, the broad unresolved spectra of **59a**, **59b**, and **59c** centered at 501 nm, 490 nm, and 495 nm, respectively, demonstrated minimal substituent effects on emission wavelengths. Those nanohoops exhibited comparable radiative and non-radiative decay rates, as is evidenced by similar FQY (18%) and singlet lifetimes ($\tau_s \approx$ 0.18 ns and 7 ns, respectively).

2.1.4. Iron catalysis. In 2020, Yang reported an $FeCl_3 \cdot 6H_2O$-catalyzed cyclization reaction for the synthesis of N-embedded cubane.[43] Under these conditions, the desired product **61** was obtained in 40% yield (Scheme 16a). However, when other catalysts such as trifluoroacetic acid, $BF_3 \cdot OEt_2$, and *p*-toluenesulfonic acid were tested, little to no product was observed. Crystal structure analysis revealed that macrocycle **61** exhibited a cubic

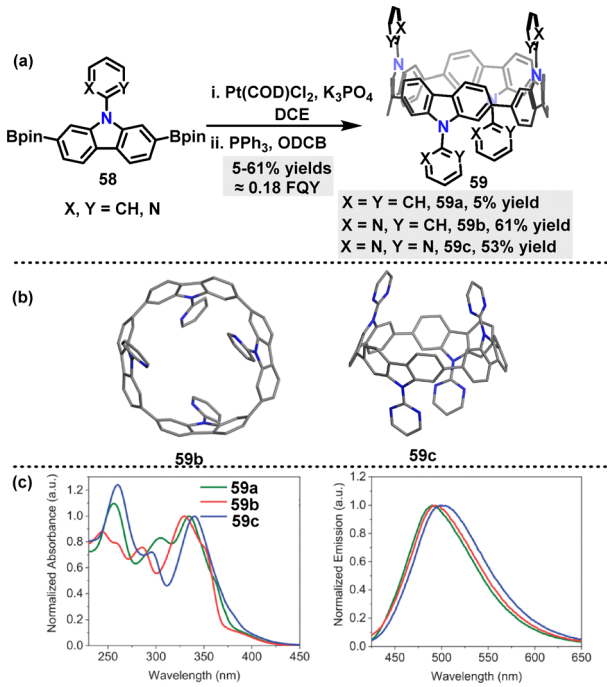

Scheme 15 (a) Synthesis of nanohoops **59** and (b) crystal structures of **59b** and **59c**, (c) absorption in DCM at 350 nm (left) and emission (right) in DCM at 340 nm for **59**. Adapted from ref. 42 with permission from Wiley-VCH, copyright 2024.

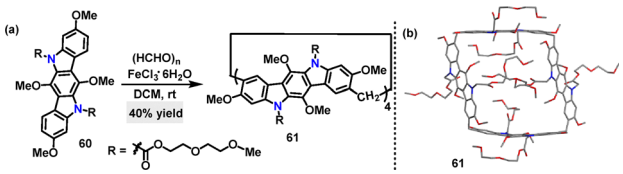

Scheme 16 (a) Synthesis and (b) crystal structure of macrocycle **61**.

architecture, where four indolocarbazole units were bridged by methylene groups at the 2,8-positions (Scheme 16b). The cavity measures 13.96 Å vertically and 9.01 Å horizontally, significantly larger than the cavities of pillar[5]arene (5 Å) and pagoda[4]-arene (7.9 Å). DFT calculations confirmed its energy-minimized cubic conformation, with dihedral angles of 72–102° reflecting a nonplanar geometry.

Later, Chen[44] reported an $FeCl_3{\cdot}6H_2O$-catalyzed one-pot condensation of substituted 9-phenylcarbazoles **62** and paraformaldehyde in DCM, affording macrocycles **63a** and **63b** in 65% and 73% yields, respectively (Scheme 17a). A novel N-doped aromatic belt **64** incorporating a [6]cycloparaphenylene (CPP) skeleton was then synthesized in 51% yield *via* the transformation of macrocycle **63a**. Crystal structure analysis revealed that three carbazole subunits within macrocycle **63b** were oriented on the identical side, thereby giving rise to bowl-shaped architecture (Scheme 17b). Macrocycle **64** adopted a slightly elliptical macrocyclic structure, featuring an average diameter of 7.719 Å and a deep cavity (7.948 Å in depth) (Scheme 17c). It exhibited intense green fluorescence (Em: 534 nm) with a quantum yield of 0.39 and a large Stokes shift (170 nm), which was attributed

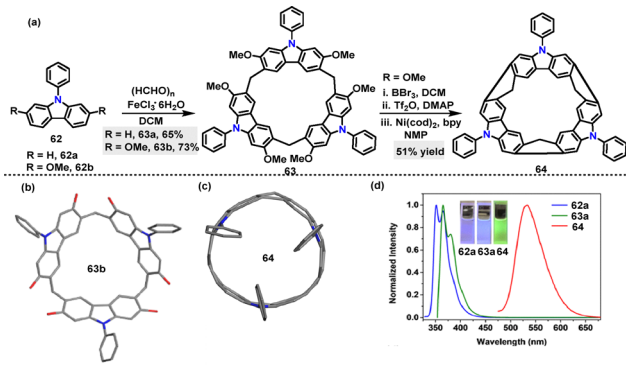

Scheme 17 (a) Synthesis of macrocycles **63** and **64** and (b) and (c) crystal structures of N-doped aromatic belts **63b** and **64**, and (d) fluorescence spectra of **62a**, **63**, and **64**. Adapted from ref. 44 with permission from Wiley-VCH, copyright 2021.

to structural relaxation in the excited state (Scheme 17d). UV-vis spectroscopy revealed a narrow HOMO–LUMO energy gap (2.02 eV), significantly smaller than those of undoped [6]CPP (3.13 eV) and methylene-bridged [6]CPP (2.66 eV).[45] This observation highlighted the enhanced conjugation induced by N-doping.

In 2022, Chen[46] synthesized the luminescent macrocycle **66** in 30% yield *via* an $FeCl_3{\cdot}6H_2O$-catalyzed one-pot Friedel–Crafts (F–C) alkylation reaction between *s*-triphenyltriazine-derived acridan **65** and paraformaldehyde (Scheme 18a). In the crystal structure of **66**, the twisted geometry between the *s*-triphenyltriazine acceptor units and acridan donor units facilitates spatial separation of the HOMO and LUMO (Scheme 18b), thereby reducing the ΔE_{ST}. DFT and TD-DFT calculations revealed small ΔE_{ST} values for both cone and partial-cone conformers (Scheme 18c). The experimental ΔE_{ST} value, measured from fluorescence and phosphorescence spectra in neat film at 77 K, was 12 meV, in good agreement

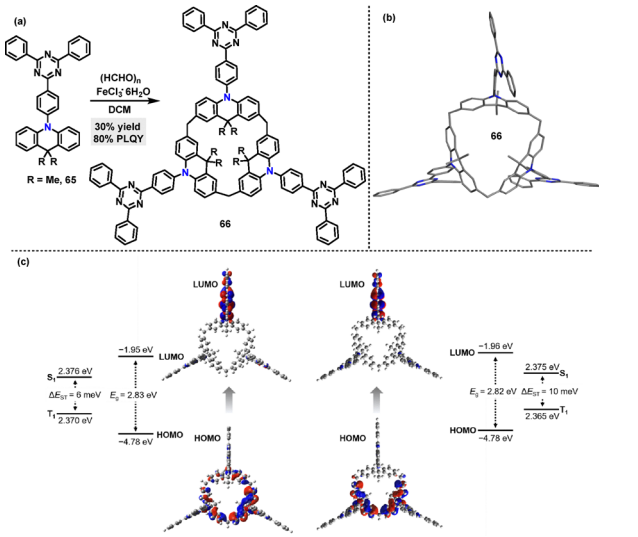

Scheme 18 (a) Synthesis and (b) crystal structures of luminescent macrocycle **66**, (c) calculated energy levels of macrocycle **66**: cone conformer and partial-cone conformer.[46] Reproduced from ref. 46 with permission from The Royal Society of Chemistry, copyright 2022.

with theoretical analysis. Moreover, macrocycle **66** exhibited excellent TADF emission with a PLQY of 80%.

2.2. Metal-free strategies

2.2.1. Lewis acid catalysis. In 2023, Dessie[47] reported a one-pot [2+2] condensation of substrate **67** and paraformaldehyde for the synthesis of a giant-cavity macrocycle **68** (Scheme 19a). The desired product **68** was obtained in 38% yield using CF_3SO_3H as the catalyst in DCM. Crystal structure analysis revealed that **68** adopted a rigid, stretched hexagonal structure (Scheme 19b). The two naphthalene diimide groups were oriented nearly face-to-face with 17.109 Å between them, while the distance between the methylene-linked carbon atoms of adjacent 1,4-dimethoxybenzene units measured 18.769 Å. These dimensions define a giant cavity with a width of 18.769 Å and a height of 17.109 Å.

Later, Wang[48] reported a $BF_3{\cdot}Et_2O$-catalyzed [3+3] condensation of compound **69** with formaldehyde to construct Tröger's base-based [3]arenes **70** in 6–12% yields (Scheme 20a). TGA revealed that **70a** and **70b** exhibited no significant weight loss below 300 °C, indicating excellent thermal stability. Additionally, **70a** and **70b** demonstrated outstanding iodine-adsorption properties.[49,50]

Recently, Sue[51] reported a $BF_3{\cdot}Et_2O$-catalyzed cyclization of triphenylamine-derivatized monomers **71** with paraformaldehyde for the synthesis of various triphenylamine[3]arenes **72**. The bromine-substituent not only promoted the cyclization reaction (99% yield) but also provided opportunities for further transformations. For instance, treatment with *t*-BuLi in THF/MeOH converted **72** into H-terminated macrocycles **73a** (56%) and **73b** (74%). Cyanation reactions with CuCN yielded **73c** and

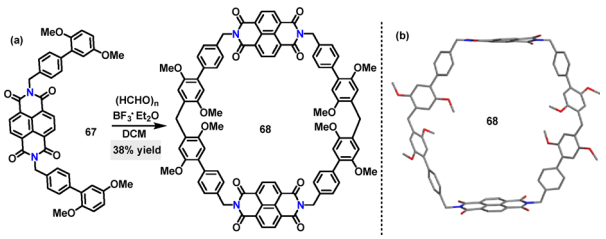

Scheme 19 (a) Synthesis and (b) crystal structures of giant-cavity macrocycle **68**.

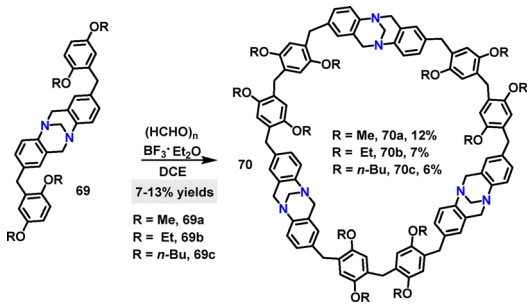

Scheme 20 Synthesis of Tröger's base-based [3]arenes **70**.

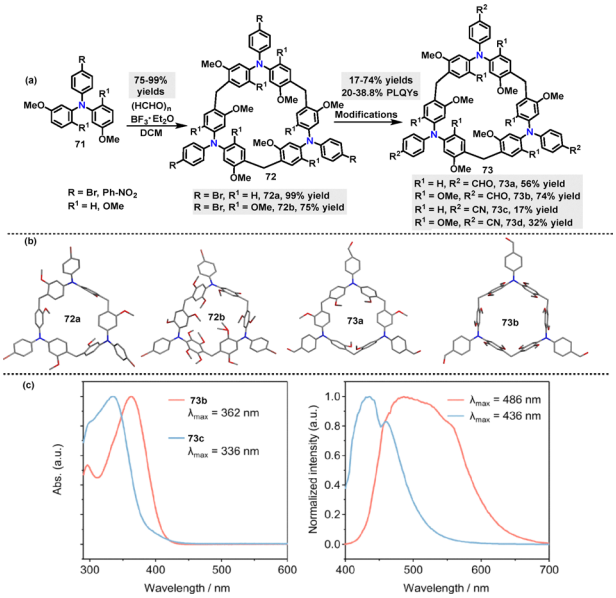

Scheme 21 (a) Synthesis of triphenylamine[3]arenes **72–73** and (b) crystal structures of **72a–b** and **73a–b**, (c) UV-vis and corresponding delayed fluorescence spectra of **73b–c**. Reproduced from ref. 51 with permission from Wiley-VCH, copyright 2024.

73d in 17% and 32% yield, respectively (Scheme 21a). Crystal structure analysis revealed that these macrocycles adopted cylindrical propeller-like structures with approximately threefold symmetry, though not perfectly symmetric (Scheme 21b). For example, macrocycle **73b** exhibited narcissistic chiral self-sorting behavior, maintaining an interlayer distance of 7.0 Å. The structure featured large one-dimensional petal-like channels (13 Å in width) and a solvent-accessible volume ratio of 56.5%. In toluene solution, **73b** and **73c** displayed (n–π*) transition bands at 362 nm and 336 nm, respectively, in their UV-vis absorption spectra. Their PL spectra showed strong steady-state emissions at 486 nm (**73b**) and 436 nm (**73c**) (Scheme 21c). Moreover, macrocycle **73c** exhibited a PLOY of 38.8%.

Given the crucial role of N-atoms in influencing the structures and properties of macrocycles, the azo-moiety has been employed to synthesize intriguing complex macrocyclic scaffolds. In 2020, Huang[52] reported a $BF_3{\cdot}Et_2O$-mediated cyclization strategy for the synthesis of azo-based macrocycles. Various derivatives with azo-groups at different substitution positions were prepared in 7–62% yields, showcasing the method's synthetic versatility (Scheme 22a). The crystal structure (Scheme 22b) analysis revealed that ***E*,*E*-75** adopted an oblate hexagonal geometry with dimensions of 17.60 Å in length and 9.76 Å in width. The structure of ***E*,*E*-75** is stabilized by diverse non-covalent interactions, including C–H···O, C–H···N, and C–H···π contacts, as well as face-to-face π–π stacking. Analogously, ***E*,*E*-77** and ***E*,*E*-79** exhibited distinct structural features and characteristic non-covalent interactions, highlighting the substituent-dependent structural diversity.

2.2.2. Brønsted acid catalysis. In 2020, Gokulnath[53] synthesized a carbazole-based macrocycle **83** in 40% yield *via* a CF_3COOH-catalyzed [3+1] condensation reaction followed by

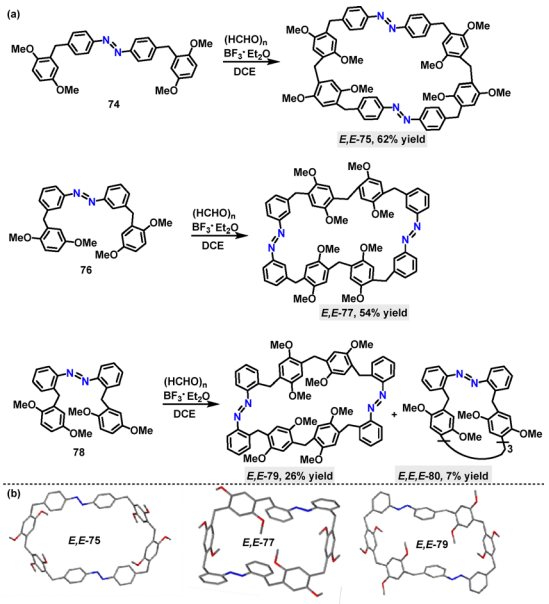

Scheme 22 (a) Synthesis of azo-macrocycles **75**, **77**, **79**, and **80** and (b) crystal structures of **75**, **77**, and **79**.

oxidation with DDQ (Scheme 23). The FQY of macrocycle **83** was determined to be 28.9%.

Later, our group[54] reported a Brønsted acid-catalyzed F–C reaction for the stereoselective synthesis of various macrocycles **85** (Scheme 24a). Kinetic control *via* ultrafast quenching (within 1 min) favored *meso*-configurations as the dominant product, while prolonged reaction times allowed thermodynamic equilibrium to shift toward *rac*-isomers or oligomerization (*e.g.*, *meso*-selectivity decreased from 75.6% de to 19.0% de over 54 h). The oxygen atom in methoxy substituents played a critical role in stabilizing *meso*-selective pathways through hydrogen-bond-enhanced aggregation, while methyl-based substrates exhibited *rac*-selectivity due to weaker intermolecular interactions. The crystal structures of *meso*- and *rac*-configured **85** revealed distinct centrosymmetric and asymmetric characteristics. ***Meso*-85a-1** featured a C2-symmetric backbone, exhibiting a rigid, extended conformation with minimized intermolecular coulombic repulsion due to centrosymmetric packing (Scheme 24b). On the other hand, ***rac*-85b-1** presented an asymmetric folded scaffold that promoted compact packing and enhanced infrared vibrational intensities for asymmetric modes (Scheme 24c).

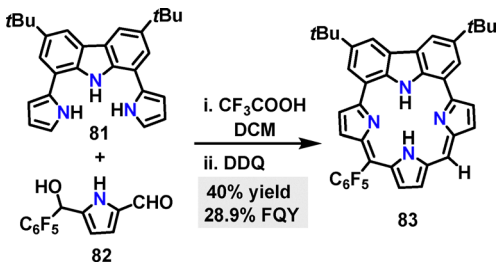

Scheme 23 Synthesis of carbazole-based macrocycle **83**.

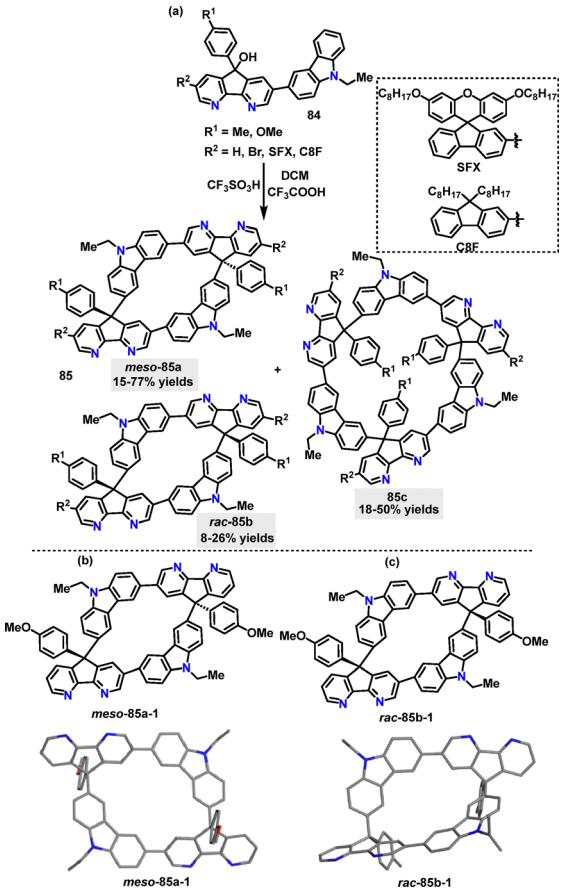

Scheme 24 (a) Synthesis of macrocycles **85** and (b) crystal structures of ***meso*-85a-1** and ***rac*-85b-1**.

In 2022, Würthner[55] reported an efficient protocol for the synthesis of chiral perylene bisimide (PBI) heterocyclophane incorporating a chiral binaphthol bisimide (BBI) moiety (Scheme 25a). Enantiomers **88** were synthesized in 8% yield *via* macrocyclization of perylene diimide **86** and racemic **87** under mild conditions. When **88** was excited at 380 nm, nearly quantitative FRET occurs due to the perfect spectral overlap between the BBI emission and PBI absorption bands (Scheme 25b). This led to the FQYs and lifetimes of **88** ranging from 80 to 98% and 6.9 to 7.7 ns in different solvents (*e.g.*, $CHCl_3$) (Scheme 25c).

In the same year Lei[56] reported a propionic acid-catalyzed condensation of the 3,6-carbazole precursor **89** with benzaldehyde, followed by oxidation with DDQ to construct macrocycle **91a** in 12% yield (Scheme 26a). However, macrocycle **91a** exhibited poor solubility in common organic solvents. Replacing benzaldehyde with 4-*tert*-butylbenzaldehyde improved solubility, affording the desired macrocycle **91b** in 15% yield. Additionally, the corresponding BODIPY-like complex **92** was synthesized in 33% yield by reacting macrocycle **91b** with excess boron trifluoride etherate in toluene. Crystal structure analysis revealed that macrocycle **91a** adopted a nonplanar, saddle-like structure, with carbazole moieties twisted upward and dipyrrin moieties twisted downward, stabilized by intramolecular hydrogen-bonding interactions (Scheme 26b). In contrast, **92** featured a bowl-like conformation

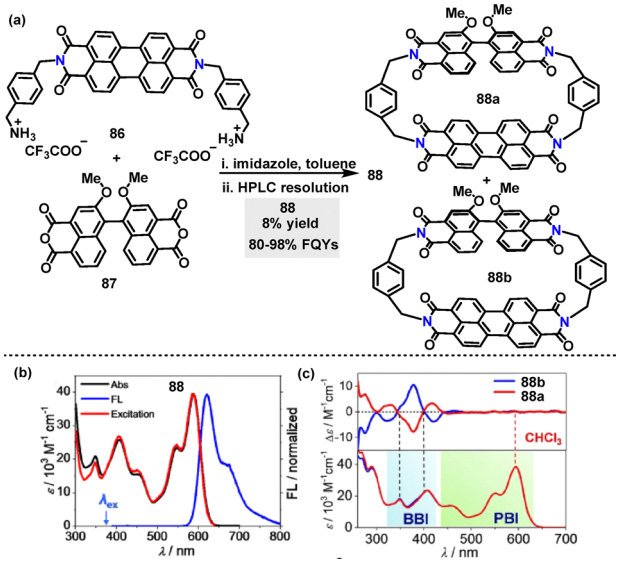

Scheme 25 (a) Synthesis of chiral perylene bisimide heterocyclophane **88**, (b) UV-vis (black line), FL (blue line, λ_{ex} = 380 nm) and excitation spectra (red line, λ_{em} = 650 nm) of **88**, (c) CD spectra of enantiomers **88** in $CHCl_3$. Adapted from ref. 55 with permission from Wiley-VCH, copyright 2022.

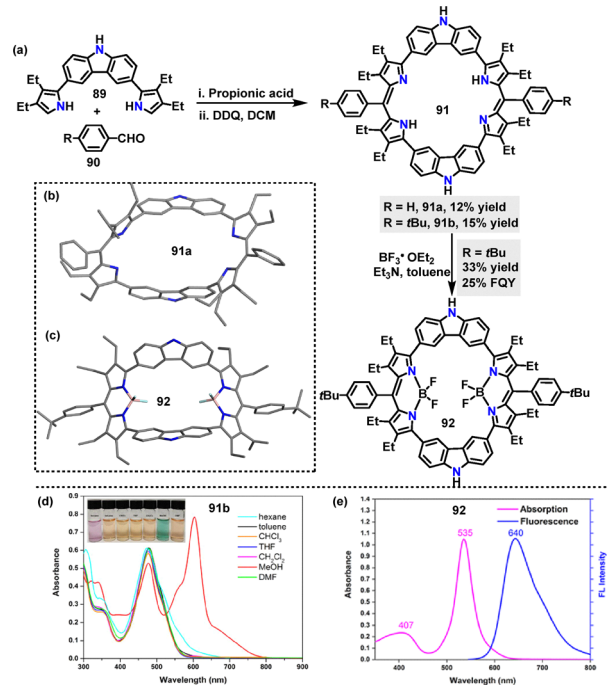

Scheme 26 (a) Synthesis of macrocycles **91** and **92**, (b) and (c) crystal structures of **91a** and **92**, (d) UV-vis absorption spectra of **91b** in different solvents, and (e) UV-vis absorption (pink line) and fluorescence (blue line) spectra of **92** in THF. Adapted from ref. 56 with permission from American Chemical Society, copyright 2022.

with two inverted pyrrole rings, where BF_2 coordination enforced planarity around the boron-dipyrrin subunits (Scheme 26c). The UV-vis spectrum of complex **91b** displayed a broad Soret-like absorption band at 477 nm (Scheme 26d). In contrast, BF_2 complex **92** showed strong absorption at 535 nm and emitted red light at 640 nm with a large Stokes shift (Scheme 26e). It possessed an FQY of 25% and an excited-state lifetime of 6.7 ns, highlighting its potential for optoelectronic applications.

In 2022, Rath[57] reported a *p*-toluenesulfonic acid (*p*-TSA)-catalyzed [3+1] oxidative condensation of *N*-confused *N*-methyl tripyrrane **93** and *N*-confused *N*-methyl dicarbinol **94**, affording *N*-confused oxocalix[4]phyrin **95** in 40% yield, and *N*-confused calix[5]phyrin **96** in 4% yield, respectively (Scheme 27a). Doubly *N*-confused mono-oxo porphyrinoid **97** was obtained in 95% yield by dehydrogenating **95** with Al_2O_3. Using chloranil and DDQ as oxidants, **95** was transformed into **98** (90% yield) and **99** (60% yield), respectively (Scheme 27b). Crystal structure analysis of **95** showed a highly distorted molecular conformation, while **99** displayed a greater deviation from planarity than **95** (Scheme 27c).

In 2023, Cong[58] developed the F–C reaction for the synthesis of a 3-symmetric rigid macrocycle. Macrocycle **101** was formed in 36% yield using methanesulfonic acid catalysis. This could be further transformed into macrocycle **103** *via* a Suzuki–Miyaura cross-coupling reaction and subsequent deprotection of tri(*tert*-butyl ester) using TFA as the catalyst (Scheme 28a). Crystal structure analysis of **103** showed a flattened cone-like geometry, where each macrocycle connects with three adjacent cones along radial directions through intermolecular double

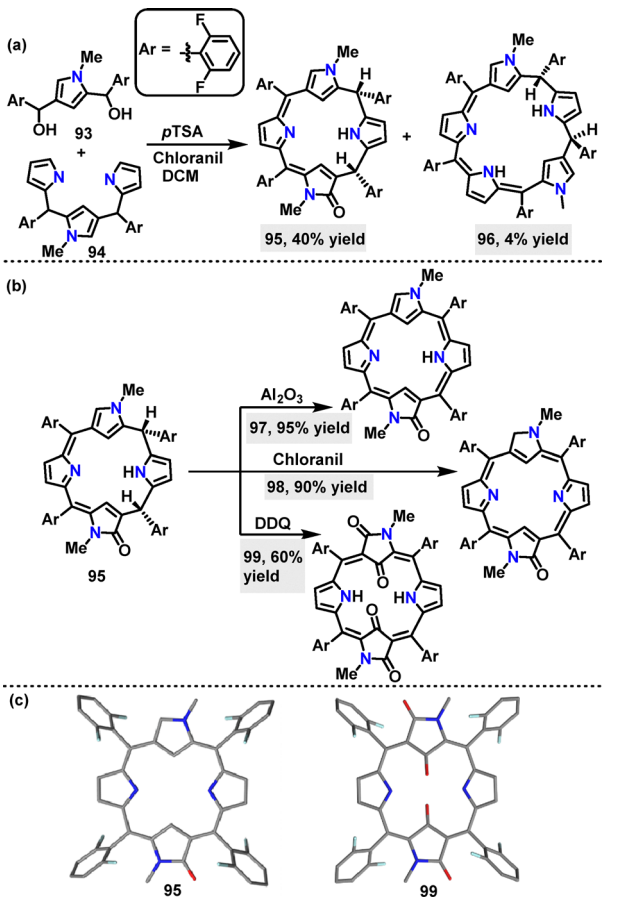

Scheme 27 (a) Synthesis and (b) modifications of macrocycles **95–99**, and (c) crystal structures of **95** and **99**.

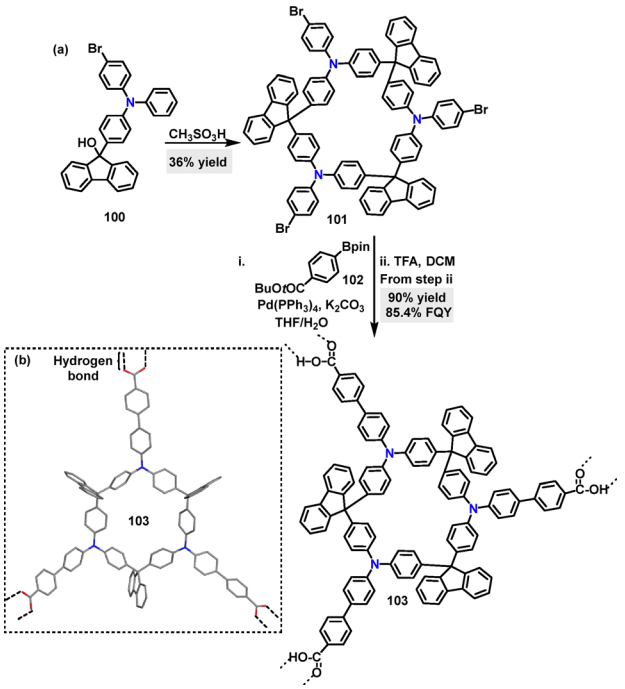

Scheme 28 (a) Synthesis of macrocycles **101** and **103**, and (b) crystal structure of **103**.

hydrogen-bonding interactions between carboxylic acid groups at the end of each radial arm (Scheme 28b). In THF solution, **103** exhibited strong Em at 455 nm, a high FQY of 85.4%, and dual emission lifetimes of 0.34 ns and 2.80 ns.

Recently, Ma[59] reported the synthesis of carbazole-based macrocycles **105** (11–16% yields), comprising 5-(9*H*-carbazol-9-yl)isophthalonitrile (D) and 1,4-dimethoxybenzene (A) *via* a Suzuki–Miyaura coupling reaction (Scheme 29a). The structures

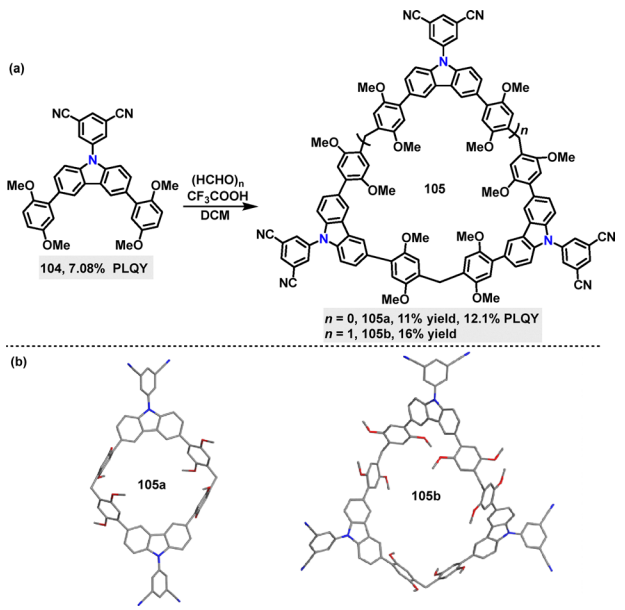

Scheme 29 (a) Synthesis and (b) crystal structures of carbazole-based macrocycles **105**.

of **105a** and **105b** were confirmed by single-crystal X-ray diffraction analysis (Scheme 29b). In various solvents, the PL spectra of **105a** and **105b** exhibited a bathochromic shift from toluene to DCM, indicative of ICT characteristics. The fluorescence and phosphorescence spectra recorded at 77 K in toluene solution were used to calculate the ΔE_{ST}, yielding values of 0.063 eV for **105a** and 0.066 eV for **105b**. DFT and TD-DFT calculations further confirmed the charge transfer nature and small ΔE_{ST} of these macrocycles, suggesting typical TADF properties. In the solid state, **105b** emits at approximately 480 nm, while **105a** shows a red-shifted emission peak at 510 nm, likely attributed to stronger intermolecular interactions. These intermolecular interactions restrict intramolecular motion and suppress non-radiative decay, contributing to enhanced PLQY in the solid state. For example, **105a** displayed a PLQY of 12.1%, significantly higher than its monomer counterpart **104** (7.08%).

Recently, Yang, Yu, Wu, and co-workers[60] developed a novel Mannich-type macrocyclization strategy for the synthesis of henacetin[3]arenes **107** (Scheme 30). The synthesis method involved a one-pot condensation under $BF_3{\cdot}Et_2O$ conditions, generating three substituted macrocycles in 7.8–25.9% yields. The yield improvement for **107b** of 25.9% was attributed to the higher nucleophilicity of the benzamide nitrogen, which enhanced the initial imine formation and suppressed competing F–C pathways.

2.2.3. Brønsted base catalysis. In 2020, Wang reported a chiral macrocycle through the [1+1] condensation between a bis-amine and a bis-isothiocyanate (Scheme 31).[61] Employing triethylamine as the base, macrocycle **110** was generated on a multi-gram scale in 71% yield. The high yield was attributed to the preorganized geometry of the building blocks and the driving force of multiple intramolecular hydrogen bonds (C═S···H–N), which favored cyclization over oligomerization.

In 2021, Zang[62] reported the synthesis of a fluorescent tetraphenylethene (TPEM)-based macrocycle **113** with AIE properties,

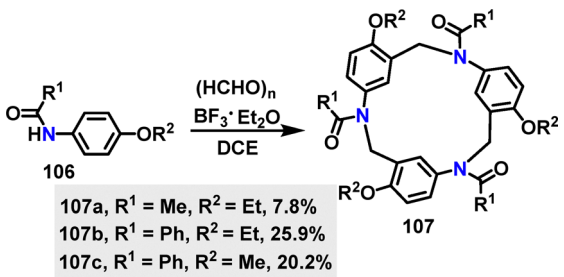

Scheme 30 Synthesis of macrocycles **107**.

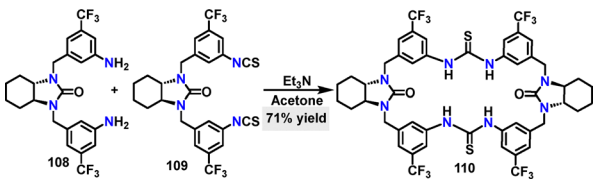

Scheme 31 Synthesis of chiral macrocycle **110**.

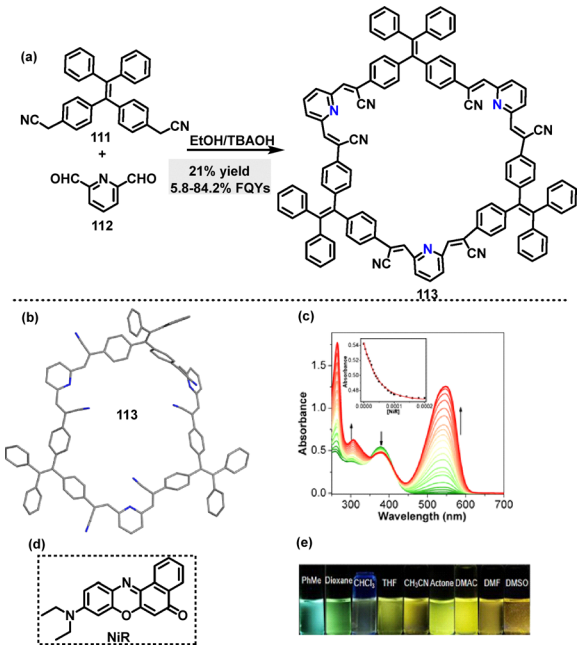

Scheme 32 (a) Synthesis and (b) crystal structure of tetraphenylethene-based **113**, (c) changes in the UV-vis spectrum of TPEM in $CHCl_3$ with the addition of NiR, (d) structure of NiR, and (e) fluorescence images. Reproduced with permission from ref. 62. American Chemical Society, copyright 2022.

enabling bright customized-color CPL. Macrocycle **113** was obtained in 21% yield *via* a facile Knoevenagel condensation of dibenzyl cyanide **111** with 2,6-pyridinedicarboxaldehyde **112** in ethanol (EtOH) containing tetrabutylammonium hydroxide (TBAOH) (Scheme 32a). Crystal structure analysis showed that macrocycle **113** featured a large cavity capable of encapsulating guest molecules to construct host–guest supramolecular systems (Scheme 32b). For instance, changes in absorbance were observed in the UV-vis spectra upon adding Nile red (NiR) to macrocycle **113** (Scheme 32c), indicating ground-state intermolecular interactions between TPEM and NiR (Scheme 32d). In tetrahydrofuran (THF), **113** exhibited a main absorption band at 376 nm, with its fluorescence emission color transitioning from blue to green and finally to yellow, as solvent polarity increases, indicating an ICT effect (Scheme 32e). Macrocycle **113** exhibited AIE characteristics with a low FQY of 5.8% in pure THF. This increased significantly to 84.2% in a 95% water–THF mixture.

In 2024, Kumagai[63] reported an efficient method for the construction of a macrocyclic diamide incorporating two indole units. Macrocycle **115** was obtained in 95% yield using Movassaghi's pyridine/quinoline-forming protocol (Scheme 33a). Further transformations of **115** yielded diverse new architecture macrocycles **116** containing two indole and two quinoline moieties in 25–42% yields. Macrocycles **116** can act as ligands due to the multiple N atoms, forming neutral Zn^{2+} complexes. Crystal structure analysis revealed that both **116g** and the **116g**/Zn^{2+} complex adopted saddle-shaped structures with C_2 symmetry (Scheme 33b). In acetonitrile (ACN), macrocycles **116a–g** exhibited absorption maxima ranging from 307 to 342 nm, with

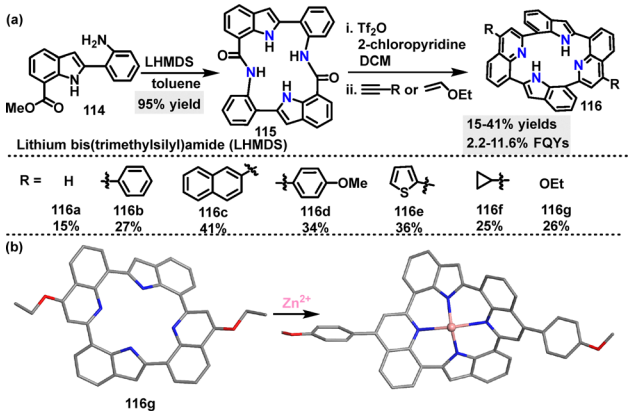

Scheme 33 (a) Synthesis and modification of macrocycle **115** and (b) crystal structures of **116g** and the **116g**/Zn^{2+} complex.

molar absorptivity values of 1.46–2.95 × 10^4 M^{-1} cm^{-1}. These derivatives (**116a–f**) were emissive in both the solution (FQYs: 2.5–11.6%) and the solid state (FQYs: 2.2–5.8%). Notably, **116g** bearing ethoxy substituents showed a relatively high FQY of 11.6% in ACN, likely attributed to the electron-donating nature of the ethoxy groups, which enhance intramolecular charge transfer.

Recently, Gale[64] reported an efficient and synthetically straightforward strategy for constructing tetra-urea macrocycle **118**, achieving a 21% yield through a [2+2] cyclization under $NaHCO_3$ and subsequent KPF_6 conditions (Scheme 34). Macrocycle **118** had eight electron-withdrawing chlorine substituents, which enhanced its anion-binding capability.

2.2.4. Other conditions. In 2024, Hamedani[65] reported a one-pot condensation of an aldehyde **119** with diethylenetriamine **120** for the synthesis of a pyrrole-based macrocycle **121**, achieving an 82% yield using methanol (MeOH) as the solvent (Scheme 35). The Cd^{2+} complex ([Cd**121**]) could be formed by reacting **121** with $Cd(NO_3)_2{\cdot}6H_2O$. Additionally, both **121** and

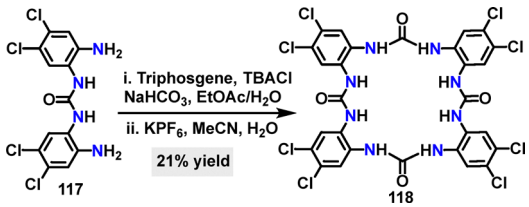

Scheme 34 Synthesis of the tetra-urea macrocycle **118**.

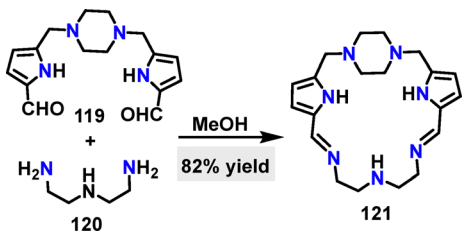

Scheme 35 Synthesis of pyrrole-based macrocycle **121**.

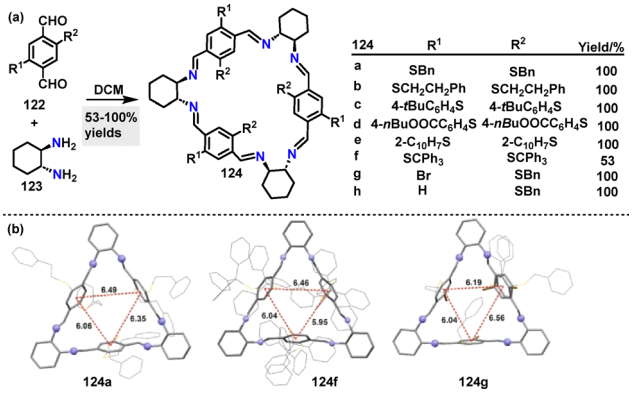

124	R^1	R^2	Yield/%
a	SBn	SBn	100
b	SCH_2CH_2Ph	SCH_2CH_2Ph	100
c	4-*t*BuC_6H_4S	4-*t*BuC_6H_4S	100
d	4-*n*Bu$OOCC_6H_4S$	4-*n*Bu$OOCC_6H_4S$	100
e	2-$C_{10}H_7S$	2-$C_{10}H_7S$	100
f	$SCPh_3$	$SCPh_3$	53
g	Br	SBn	100
h	H	SBn	100

Scheme 36 (a) Synthesis of chair-type macrocycles **124** and (b) crystal structures of **124a**, **124f**, and **124g**. Reproduced from ref. 67 with permission from Springer Nature, copyright 2025.

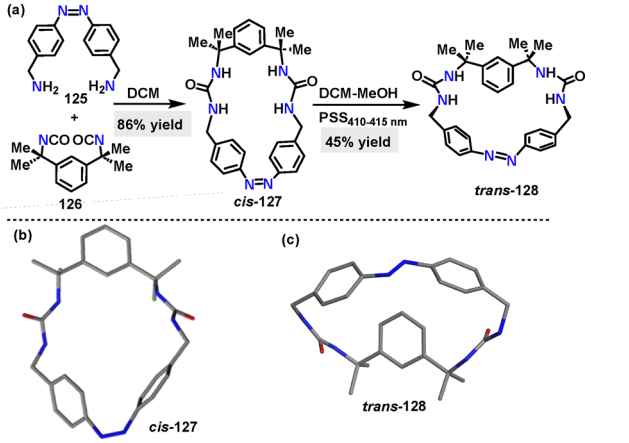

Scheme 37 (a) Synthesis and (b) crystal structures of azobenzene-based macrocycles **127** and **128**.

[Cd**121**] demonstrated notable 2,2-diphenyl-1-picryl-hydrazyl-hydrate (DPPH) radical scavenging activity, with IC_{50} values of 1.03 and 1.42 mg mL^{-1}, respectively, comparable with that of ascorbic acid.[66]

In 2025, Kwit[67] reported an efficient method for the synthesis of chair-type macrocyclic compounds **124**. Diverse macrocycles **124** were synthesized in 53–100% yields *via* [3+3] cyclocondensation reactions between equimolar dialdehydes **122** and chiral *trans*-1,2-diaminocyclohexane (DACH) **123** under mild conditions (Scheme 36a). Crystal structure analysis revealed that steric interactions dominate substituent arrangements, with dispersion effects playing a secondary role (Scheme 36b). The crystal structure of **124a** showed columnar aggregates stabilized by π–π stacking and C–H···S interactions, where phenyl rings from adjacent molecules intercalate into the macrocyclic cavities. In contrast, **124f** adopted a bowl-like conformation, with its trityl groups exhibiting distinct helicities influenced by combined steric and dispersive forces. Macrocycle **124g** featured solvent-filled intermolecular spaces and disordered bromine substituents, resulting in variable rim diameters (4.59–8.18 Å).

More recently, He[68] and coworkers designed and synthesized an azobenzene-based macrocycle **138** through a two-step synthetic sequence. Macrocycle ***cis*-137** was synthesized in 86% yield *via* the condensation of amine **135** and isocyanate **136** (Scheme 37a).

Irradiation of ***cis*-128** with 410–415 nm light to the photostationary state (PSS) converted it to the desired ***trans*-128** in 45% yield. Crystal structure analysis showed that ***cis*-127** adopted a V-shaped conformation with two urea units andCsp2–H forming a preorganized binding pocket (Scheme 37b). While ***trans*-128** exhibited a bow-shaped conformation with a bent azobenzene unit (49.19° angle between benzene rings) and a larger methylene distance (11.0 Å) (Scheme 37c).

3. O-doped macrocycles

The introduction of oxygen atoms endows macrocyclic compounds with unique capabilities in ion recognition, molecular inclusion, and dynamic response through lone pair electron coordination, hydrogen bonding, and polarity regulation.[69] In 1967, Pedersen discovered crown ethers,[70,71] after which oxygenated macrocycles,[72] including cyclodextrins and macrocyclic polyethers, have demonstrated significant potential at the intersection of chemistry, materials science, and life sciences. Many of their derivatives, now extensively studied and reported, have opened new avenues for supramolecular chemistry. Recently, numerous synthetic methods have been developed for fascinating O-doped macrocycles, enabling their broad applications across diverse fields.

3.1. Metal catalysis

3.1.1. Palladium catalysis. In 2021, Noonan[73] reported an efficient method for the synthesis of a six-membered oligofuran macrocycle **130**. Using the G3–Pd–SPhos catalyst system, macrocycle **130** was obtained in 34% yield *via* a cross-coupling reaction (Scheme 38). Electrochemical studies revealed two reversible reduction events at −1.49 V and −1.70 V, with no signs of instability observed after multiple reduction cycles. These potentials were cathodically shifted compared to those of the α,α′-tetramer of 2,2′-bifuran-3,3′dicarboximide[74] (−1.0 V) and cyclo[6]pyrrole[75] (−0.48 V).

3.1.2. Iron catalysis. In 2024, Chen[76] reported an $FeCl_3$-catalyzed one-pot condensation for the synthesis of dibenzofuran-[3]arene **132** in 33% yield. This functional macrocyclic arene **132** was further transformed into a macrocycle belt **133**, featuring a rigid ring-shaped structure (Scheme 39a). Crystal structure analysis showed that macrocycle **132** exhibited a structure with a high

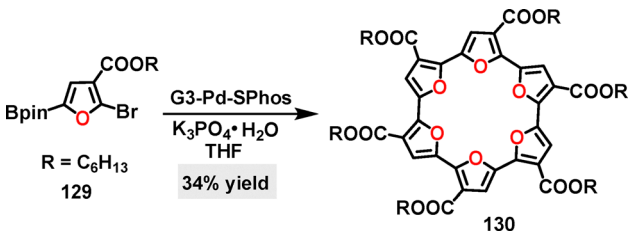

Scheme 38 Synthesis of six-membered oligofuran macrocycle **130**.

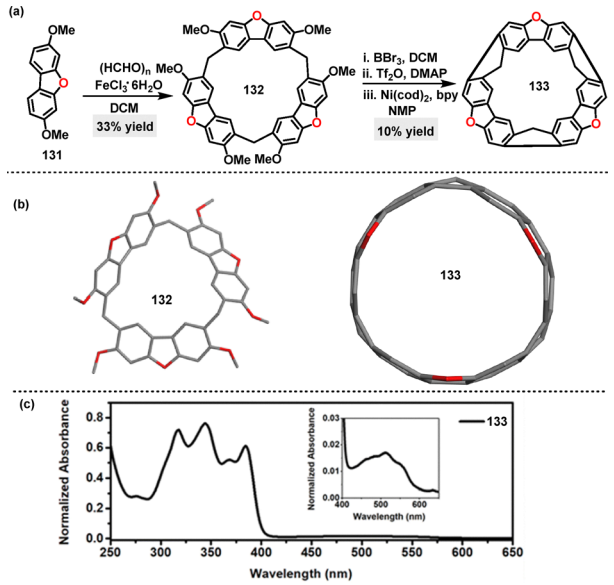

Scheme 39 (a) Synthesis and (b) crystal structures of dibenzofuran[3]arene **132** and macrocycle belt **133**, and (c) UV-vis absorption spectrum of macrocycle **133**. Adapted from ref. 76 with permission from The Royal Society of Chemistry, copyright 2024.

degree of symmetry, while the macrocycle belt **133** revealed a highly symmetrical barrel-like architecture (Scheme 39b). In DCM, macrocycle belt **133** exhibited a broad absorption band with four intense peaks at 316, 344, 369, and 384 nm, accompanied by a weak, broad absorption band spanning 400–600 nm (Scheme 39c). The optical band gap derived from the UV-vis spectrum (2.16 eV) was narrower than that of methylene-bridged [6]CPP[77] (2.66 eV) and slightly wider than the N-doped methylene-bridged [6]CPP[78] (2.02 eV). This phenomenon can be attributed to the incorporation of O-atoms, which was designed to enhance π-conjugation.

3.1.3. Tin catalysis. In 2021, Li[79] reported a F–C cyclization between substrate **134** and acetone **135** for the synthesis of a cylindrical furan-based macrocycle **136** in 36% yield (Scheme 40). Twelve C–C bonds were formed simultaneously using $SnCl_4$ as the Lewis acid catalyst in anhydrous DCM. In contrast, other Lewis acids (*e.g.*, $FeCl_3$, $AlCl_3$, and $BF_3{\cdot}OEt_2$) or Brønsted acids (*e.g.*, TFA, HCl, and H_2SO_4) either failed to promote the reaction or led to polymeric byproducts. Crystal structure analysis of **136** revealed that the internuclear distance between the bridging carbon atoms connected to furans *via* a single acetone bridge is 16.1 Å, whereas the corresponding distance for furans linked by bis-acetone bridges was 14.4 Å.

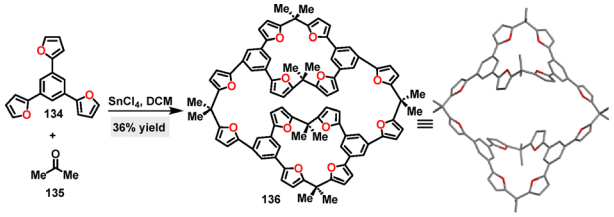

Scheme 40 Synthesis and crystal structure of furan-based macrocycle **136**.

3.2. Metal-free strategies

3.2.1. Lewis acid catalysis. In 2022, Li, Luo, and co-workers developed a F–C reaction for the synthesis of two endo-functionalized macrocycles **138** (Scheme 41).[80] Both products were demonstrated to enhance molecular recognition capabilities. Under $BF_3{\cdot}Et_2O$-catalyzed condensation conditions, the target macrocycles were obtained in 62% and 31% yields, respectively. Furthermore, the benzofuranyl groups in **138a** and **138b** likely function as endo-binding sites of hydrogen-bonding donors, making them well-suited for binding heterocyclic guests (*e.g.*, pyrrole and indole) through hydrogen-bonding interactions.

3.2.2. Brønsted acid catalysis. In 2021, Tiefenbacher[81] reported the synthesis of a series of xanthene[*n*]arenes **150** and **151** *via* a TFA-catalyzed macrocyclization of prefunctionalized xanthene monomers **149**, with yields ranging from 4% to 21% (Scheme 42a). Notably, the selective formation of **150** or **151** was governed by the steric hindrance at the C9-position of monomers **149**, which was modulated by different alkyl

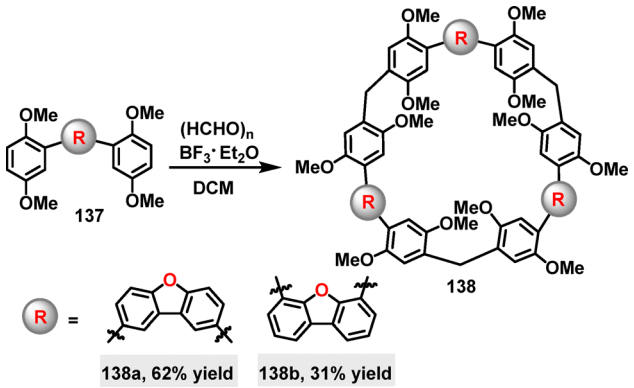

Scheme 41 Synthesis of benzofuran-based macrocycle **138**.

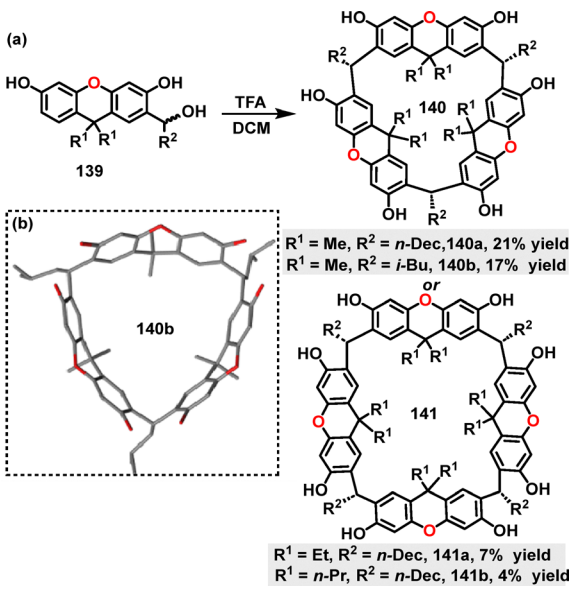

Scheme 42 (a) Synthesis of xanthene[*n*]arenes **140** and **141** and (b) crystal structure of **140a**.

substituents (methyl, ethyl, or *n*-propyl). For instance, smaller substituents (*e.g.*, methyl groups) favored the formation of **150** (17–21% yields), whereas larger substituents (*e.g.*, ethyl or *n*-propyl) promoted the generation of **151** (4–7% yields). Crystal structure analysis of macrocycle **140b** revealed a crown-shaped (bowl-like) conformation (Scheme 42b). Structural characterization showed tetrahedral angles of 109.4° between adjacent xanthene units and dihedral angles of 16.5° between the aromatic rings, a distortion attributed to macrocyclic strain. Additionally, the i-Bu substituents adopted an outward orientation, which minimized intramolecular steric hindrance and enhanced the compound's solubility.

In 2022, Jiang[82] reported the synthesis of a series of methylene-bridged naphthotube macrocycles **143** *via* a F–C reaction between alkoxy-substituted bisnaphthalenes **142** and paraformaldehyde (Scheme 43a). Using trifluoroacetic acid (TFA) as a critical catalyst, various three-membered macrocycles **143a–c** and four-membered macrocycles **143d–f** were obtained in 7–22% yields. In contrast, the use of other acids such as CF_3SO_3H, *p*-TsOH, and $BF_3{\cdot}OEt_2$ tended to induce polymer formation instead. Crystal structure analysis revealed that macrocycle **143a** exclusively adopted a C_3 symmetry (Scheme 43b). For **143d**, a double-cavity conformation, a D_{2d} symmetry was observed, where enantiomers underwent rapid interconversion in solution (Scheme 43c). Spectroscopic characterization highlighted distinct absorption maxima at 358 nm (**143a**) and 362 nm (**143d**). In DCE, these macrocycles displayed FQYs of 24.6% (**143a**) and 34.2% (**143d**), respectively.

3.2.3. Brønsted base catalysis. In 2021, Yang[83] and co-workers reported the synthesis of a tetra-cyanostilbene macrocycle **146** *via* a simple and rapid [2+2] condensation reaction (Scheme 44). Macrocycle **146** was obtained in 72% yield under NaOH-catalyzed conditions.

In the same year, Qu[84] designed and synthesized the crown-ether-based host–guest macrocycles **148**. Diverse products were obtained in 12–54% yields *via* a one-pot intramolecular etherification–cyclization reaction under Cs_2CO_3 conditions between ethylene glycol chains and diphenol motors (Scheme 45). Moreover, the observed higher yields for *cis* isomers, such as ***cis*-148b** (54%) compared to ***trans*-148b** (only 12%), can be attributed to the reduced strain associated with the *cis* configuration.

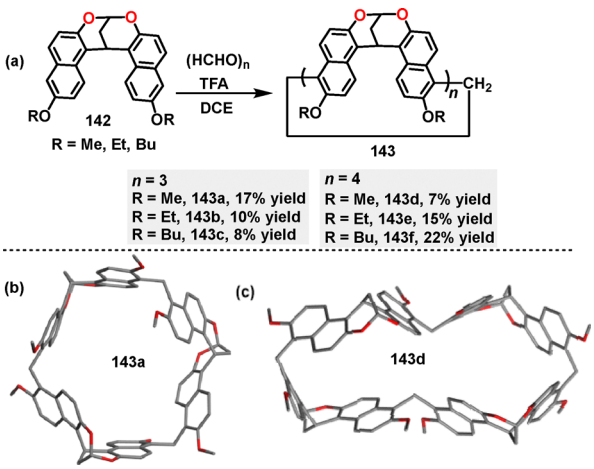

Scheme 43 (a) Synthesis of methylene-bridged naphthotube macrocycles **143** and (b) and (c) crystal structures of **143a** and **143d**.

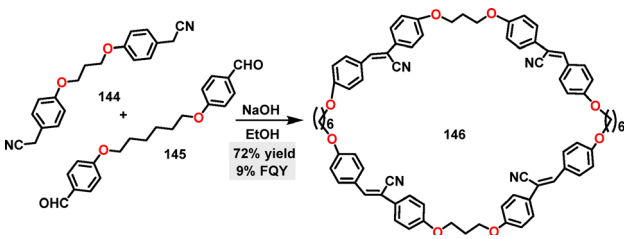

Scheme 44 Synthesis of tetra-cyanostilbene macrocycle **146**.

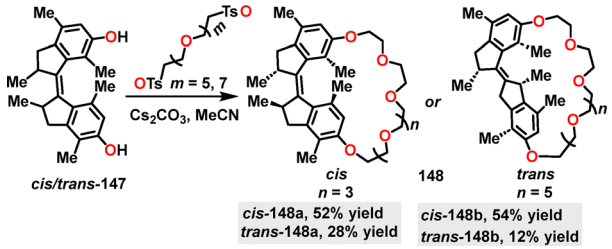

Scheme 45 Synthesis of crown-ether-based macrocycles **148**.

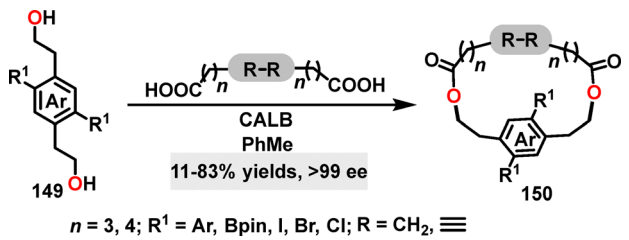

Scheme 46 Synthesis of chiral macrocycles **150**.

3.2.4. Other conditions. In 2020, Collins[85] reported a novel methodology for the synthesis of planar chiral macrocycles **150** (Scheme 46). Using *Candida antarctica* lipase B (CALB) as the catalyst, this approach enabled the generation of various chiral cyclophanes *via* sequential acylation of diols and diacids, affording yields ranging from 35% to 83% and excellent enantioselectivities (66–99% ee). Halogen-substituted derivatives (chloro and iodo) and systems incorporating rigidified bridges (diynyl and disulfide) exhibited comparable yields (63–78%) with consistently high enantioselectivities (>99% ee in most cases). Even when diverse substituents such as alkynyl groups were introduced, the enantiomeric excesses remained exceptionally high (>99% ee), underscoring the robustness of this biocatalytic strategy.

4. S-doped macrocycles

The incorporation of sulfur atoms has profoundly altered the electronic properties, coordination capabilities, self-assembly behavior, and application scope of macrocyclic compounds.[86] Owing to the unique electronic characteristics of sulfur (*e.g.*, low electronegativity and high polarizability) and its distinct

chemical attributes (such as the formation of polyvalent states and dynamic disulfide bonds), S-containing macrocycles exhibit exceptional functionalities. These properties are highly valuable in diverse fields including heavy metal adsorption, drug delivery systems, and optoelectronic devices.[87]

4.1. Metal catalysis

4.1.1. Palladium catalysis. In 2020, Liu[88] synthesized S-octulene **153** bearing two S-atoms *via* a palladium-catalyzed Suzuki coupling reaction between compounds **151** and **152**. Macrocycle **154** was obtained in 21% yield and could be further transformed into the fully fused macrocycle **154** through sequential treatment with *t*-BuOK and subsequent $Bi(OTf)_3$-catalyzed reactions (Scheme 47). DFT calculations revealed that S-octulene exhibited a large energy gap (3.19 eV), which implied that it may theoretically function as a solution-processable p-type organic semiconductor. Furthermore, the alkoxy-substituted heterocycloarene S-octulene demonstrated moderate solubility in common organic solvents such as DCM, chloroform, and toluene.

Later, the same research group reported a Suzuki coupling reaction for the synthesis of a macrocyclic structure, yielding macrocycle **156** in 32% yield (Scheme 48a).[89] This intermediate could then be converted into radical macrocycle **157** (84% yield) *via* mesitylmagnesium bromide/$BF_3{\cdot}Et_2O$-mediated F–C cyclization, followed by oxidative dehydrogenation. Crystal structure analysis revealed that radical macrocycle **157** adopted a rigid, slightly distorted coplanar backbone with a rectangle-shaped geometry (side lengths: 9.781 Å and 9.941 Å) (Scheme 48b). Compared to its all-carbon analogue **158** (Scheme 48c), radical macrocycle **157** displayed a reduced radical character (unpaired electron count 2.0 *vs.* 3.52 for **158**) and a larger singlet–triplet energy gap (−3.47 *vs.* −3.04 kcal mol^{-1} for **158**). These differences were attributed to stronger antiferromagnetic coupling through the dibenzothiophene (DBTh) units and electron donation from S-atoms.

In 2024, the π-conjugated macrocycle **160**,[90] composed of benzo[2,1-*b*:3,4-*b*′]dithiophene (BDTh) and Phen units, was synthesized in 8–14% yield *via* a palladium-catalyzed Suzuki coupling reaction. Furthermore, fused macrocycles **161** were generated in 32–41% yield through a sequence of base-promoted Wittig reaction and $Bi(OTf)_3$-catalyzed F–C reaction, starting from the aldehyde-based macrocycle **160c–d** (Scheme 49a). Crystal structure analysis revealed that **160a** adopted a nearly planar structure with polymorphic conformations. In contrast, **161b** crystals displayed a bowl-shaped dimer with a bilayer-wavy stacking pattern (Scheme 49b). Fluorescence emission spectra revealed

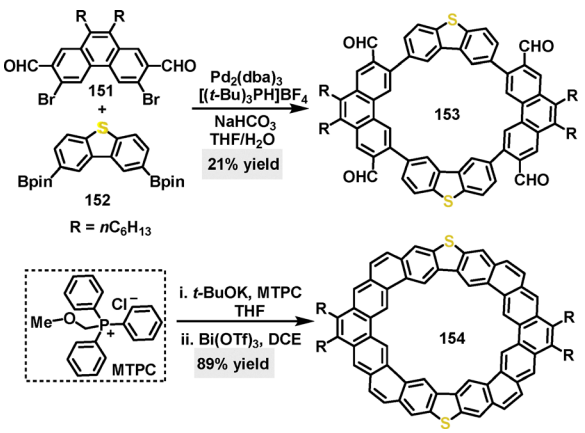

Scheme 47 Synthesis and modification of S-octulene **153**.

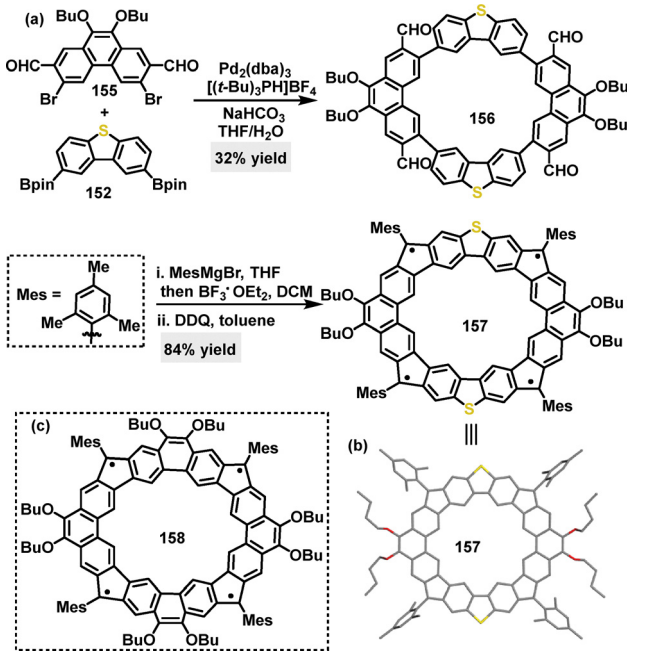

Scheme 48 (a) Synthesis and modifications of macrocycles **156**, (b) crystal structure of **157**, and (c) structure of **158**.

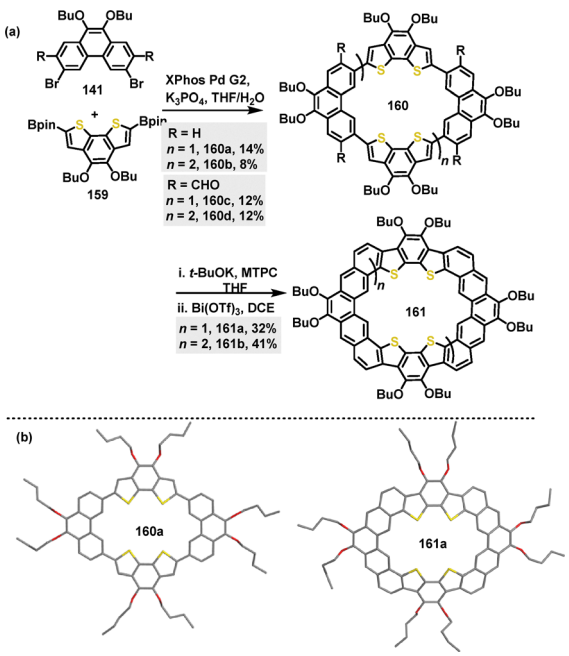

Scheme 49 (a) Synthesis and (b) crystal structures of macrocycles **160** and **161**.

a notably blue-shifted peak for **161b** at 470 nm compared to **161a** (509 nm), indicating a significant Stokes shift for **161b**.

4.1.2 Nickel catalysis. In 2021, Cong[91] synthesized a fully conjugated figure-of-eight macrocycle **163**, which integrates a flexible cyclooctatetrathiophene (COTh) core and two strained oligoparaphenylene loops. Macrocycle **163** was obtained in 17% yield *via* nickel-mediated Yamamoto homocoupling of compound **162**, and **163** was further transformed into nanohoop **164** under sodium naphthalenide conditions (Scheme 50a). ICT between the electron-rich COTh core and the paraphenylene loops in **164** resulted in a red-shifted emission at 342 nm, compared to [10]CPP (338 nm).[92,93] Additionally, nanohoop **164** exhibited an emission maximum at 520 nm (Stokes shift: 178 nm) (Scheme 50b), a notably shorter fluorescence lifetime (0.3 ns), and a reduced FQY (3%), indicative of charge transfer characteristics.

In 2023, Wu[94] reported the synthesis of π-conjugated multicyclic thiophene-based macrocycles through an intermolecular Yamamoto coupling, followed by oxidative dehydrogenation. When 1.1 equivalents of $Ni(cod)_2$ were used, a monocyclic macrocycle **166** containing four aromatic thiophene rings and a bithiophenequinodimethane moiety was obtained in an 85% yield. Notably, using 2.2 equivalents of $Ni(cod)_2$ and DDQ led to the formation of a tricyclic macrocycle **167** (80% yield) or a three-leaf clover-like tetracyclic macrocycle **168** (30% yield)

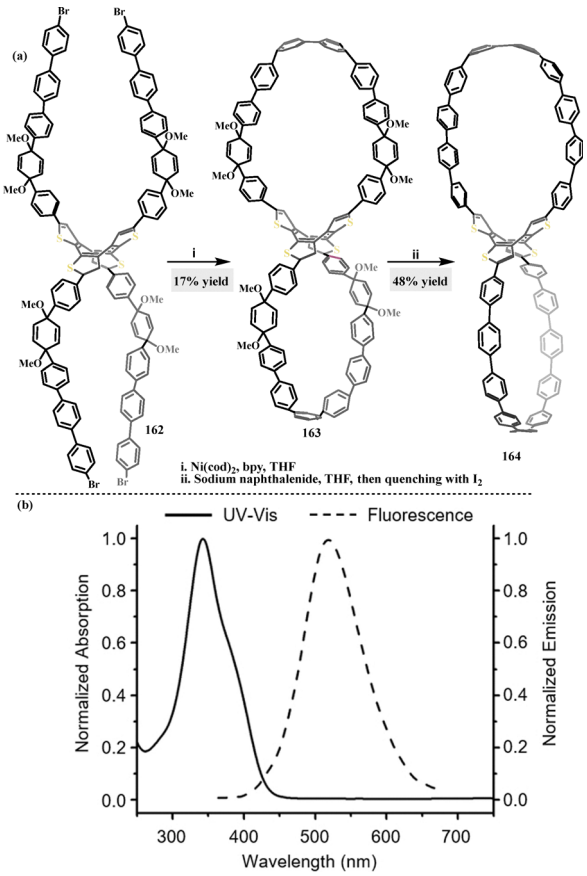

Scheme 50 (a) Synthesis of figure-of-eight macrocycles **163–164** and (b) UV-vis absorption and fluorescence of macrocycle **164** in DCM. Reproduced from ref. 91 with permission from Wiley-VCH, copyright 2021.

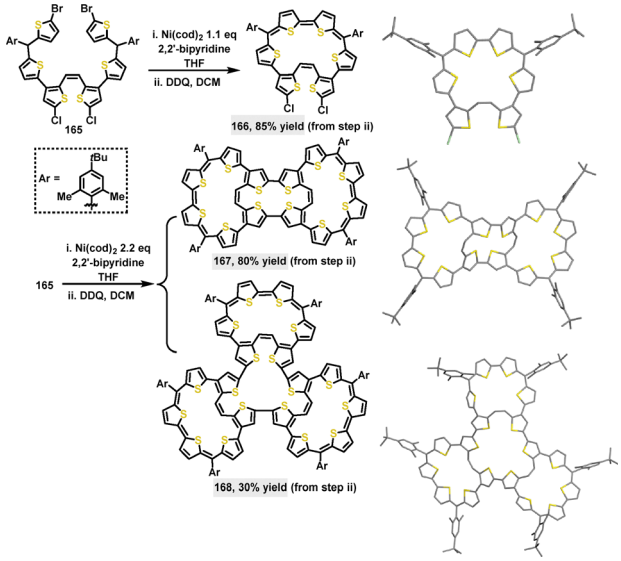

Scheme 51 Synthesis and crystal structures of thiophene-based macrocycles **166–168**.

(Scheme 51). The introduction of bulky 4-*tert*-butyl-2,6-dimethylphenyl substituents significantly enhanced the solubility and stability of these macrocycles. Crystal structure analysis showed that macrocycle **166** adopted a twisted conformation with a dihedral angle of 28.1° and significant bond length alternation (*e.g.*, 1.361 Å and 1.402 Å), indicative of antiaromaticity. The central ring of **167** exhibited an even more pronounced twist, with dihedral angles reaching up to 57.2°. Meanwhile, **168** displayed a bent three-leaf clover shape (length: 2.4 nm, width: 2.0 nm), characterized by dihedral angles at the crossing sites ranging from 14.8° to 70.7°.

Subsequently, Segawa[95] reported the synthesis of thiophene-containing polyarenes through a Ni-mediated homocoupling reaction. Under the catalytic conditions of $Ni(cod)_2$, penta(3,4-thienylene) **170a** and hexa(3,4-thienylene) **170b** were synthesized with yields of 36% and 1.5%, respectively (Scheme 52a). The low yield of **170b** was attributed to polymerization side reactions. Crystal structure analysis revealed that **170a** adopted a C_2-symmetric structure (Scheme 52b). In this structure, the thiophene moieties were connected at the 3,4-positions, forming a 10-membered ring. In contrast, **170b** exhibited a D_2-symmetric screw-like or helical structure, characterized by intramolecular π–π interactions, with a centroid distance of 3.4 Å (Scheme 52c). Both **170a** and **170b** showed size-dependent bathochromic shifts. The longest absorption maxima were observed at 273 nm for **170a** and 276 nm for **170b**. These shifts were ascribed to the decrease in the HOMO–LUMO gaps, as was supported by DFT calculations. The HOMO energy level decreased from −5.97 eV in **170a** to −5.76 eV in **170b**, while the LUMO energy level changed from −0.83 eV in **170a** to −0.82 eV in **170b** (Scheme 52d).

4.1.3. Titanium catalysis. In 2020, Iyoda[96] reported the synthesis of various macrocyclic π-extended thiophene skeletons through McMurry coupling of dialdehyde **171**. By using $TiCl_4$ as a catalyst, the π-conjugated macrocycles **172a** and **172b** were obtained with yields of 4% and 10%, respectively

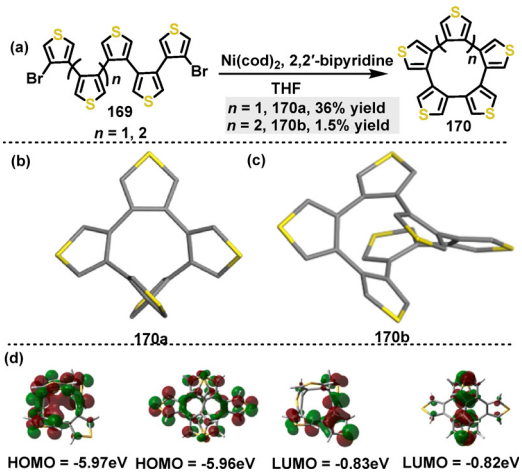

Scheme 52 (a) Synthesis and (b) and (c) crystal structures of thiophene-containing polyarenes **170**, and (d) Frontier molecular orbitals and the energy levels of **170**, calculated at the B3LYP-D3/6-31G(d) level. Reproduced from ref. 95 with permission from The Royal Society of Chemistry, copyright 2023.

(Scheme 53a). Additionally, macrocycle **173** could be prepared from macrocycle **172a** in a 60% yield under UV light irradiation. Crystal structure analysis of these macrocycles revealed their distinct geometries (Scheme 53b and c). UV-vis spectroscopy analysis showed that macrocycles **172a**, **172b**, and **713** exhibited maximum absorption wavelengths at 369 nm, 375 nm, and 409 nm, respectively (Scheme 53d). The redshift observed in macrocycle **173** implies an increased planarity. Furthermore, these compounds displayed low FQYs (**172a:** 0.74%; **172b:** 0.77%; **173:** 1.1%) due to their ring strain and conformational flexibility.

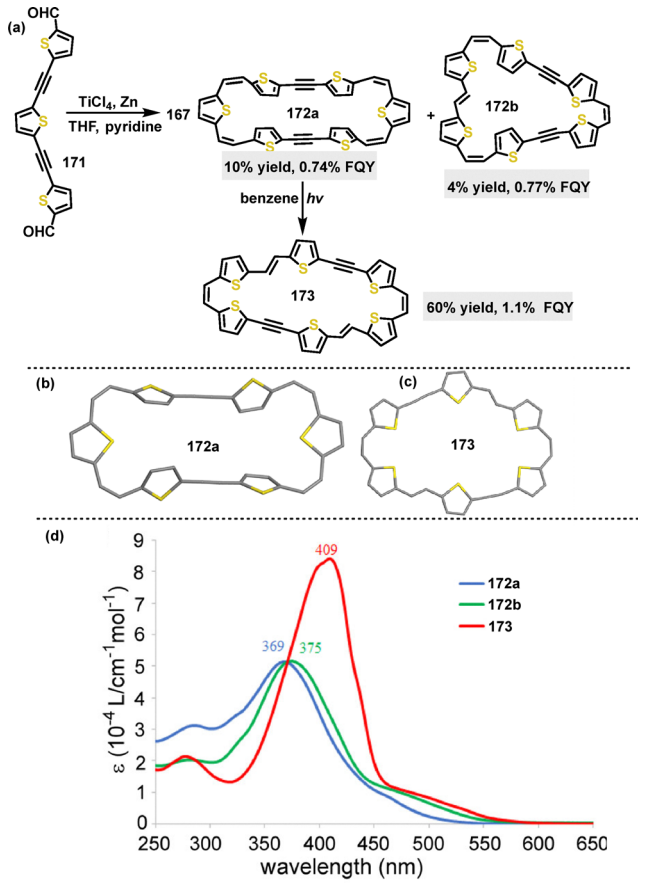

Scheme 53 (a) Synthesis of π-conjugated macrocycles **172–173**, and (b) and (c) crystal structures of **172a** and **173**, and (d) UV-vis spectra of **172 and 173** in DCM. Adapted from ref. 96 with permission from American Chemical Society, copyright 2020.

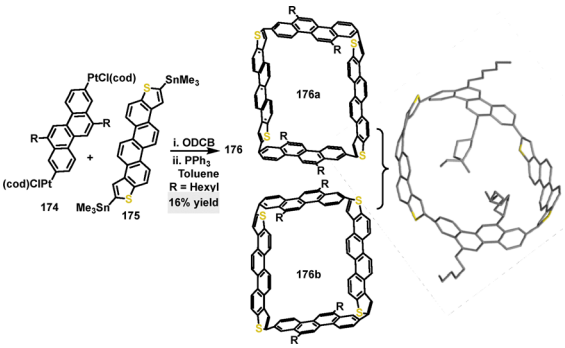

Scheme 54 Synthesis and crystal structure of thiophene-doped macrocycle **176**.

4.1.4. Platinum catalysis. In 2021, Isobe[97] reported a stereoselective cross-coupling macrocyclization. A thiophene-doped macrocycle **176** was obtained as a racemate in 16% yield through the reaction of tetrameric platinum complexes **174** and **175** in 1,2-dichlorobenzene (ODCB), involving triphenylphosphine ligand exchange and reductive elimination (Scheme 54). Crystal structure analysis of the racemate macrocycle **176** revealed an oval-shaped architecture, stemming from the pyramidalization of carbon atoms and twisted biaryl linkages with dihedral angles reaching up to 36°. CD spectroscopy revealed a strong molar ellipticity of **176a** (-317 M^{-1} cm^{-1}), indicative of a significant rotatory strength. Relaxed potential energy scans demonstrated that structural distortions increased the energy by less than 2 kcal mol^{-1}, suggesting that the structure exhibits high flexibility.

4.2. Metal free strategies

4.2.1. Lewis acid catalysis. In 2023, Zhu synthesized a trimeric macrocycle ***rac*-178** in 15% yield, *via* a one-pot Lewis acid-catalyzed condensation with paraformaldehyde.[98] Notably, only $BF_3{\cdot}Et_2O$ effectively promoted cyclization, whereas other Lewis acids (*e.g.*, $AlCl_3$, *p*-TsOH, and TFA) led to polymerization or recovered the starting material, indicating a specific acid-template effect essential for this cyclization. Crystal structure analysis of ***rac*-178** confirmed the helical belt-like structure, with a hexagonal prismatic cavity (Scheme 55).

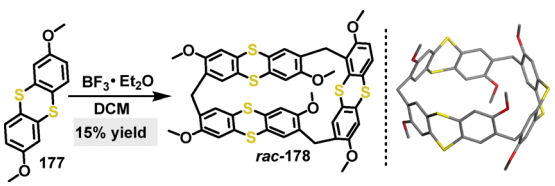

Scheme 55 Synthesis of chiral macrocycle ***rac*-178** and crystal structure of ***rac*-178**.

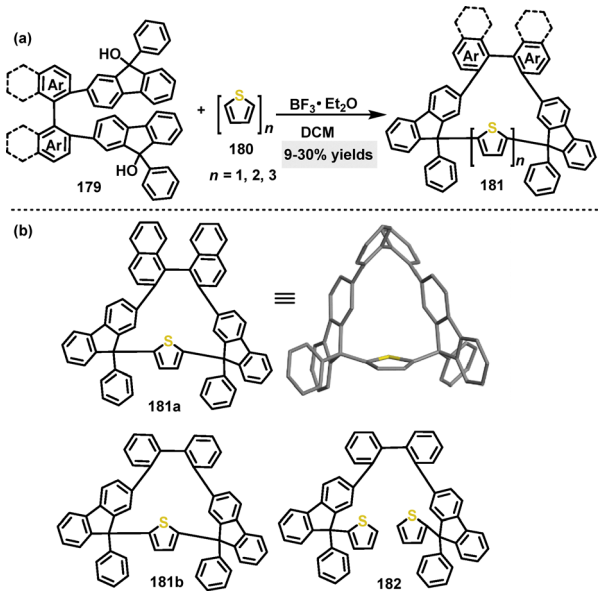

Scheme 56 (a) Synthesis of chiral nanogrids **181** and (b) crystal structure of **181a**.

In the same year, our group developed a one-pot strategy to construct axially and centrally chiral nanogrids (AGs) *via* F–C gridization.[99] By combining thiophene derivatives with difluorenyl biaromatic derivatives under $BF_3{\cdot}Et_2O$ catalysis, various macrocycles **181** were obtained in 9–30% yield (Scheme 56a). Crystal structure analysis of **181a** confirmed a C_2-symmetric molecular skeleton featuring waistline lengths of 1.11–1.12 nm and a biphenyl dihedral angle of 77.98° (Scheme 56b). The study compared the performance of the macrocyclic nanogrid **181b** with its ungridized **182**, highlighting the distinct advantage conferred by the rigid, well-defined nanogrid architecture.

4.2.2. Other conditions. In 2022, Swager[100] reported a green synthetic approach to construct thiapillar[6]arene *via* a thia-Michael addition of bis(cyclohexa-2,5-diene-1,4-dione) derivatives **183** and 4,4′-thiobisbenzenethiol **184**. The thiapillar[6]arene macrocycle **185** was obtained in 27% yield using isopropanol (i-PrOH) as solvent, and it could be further transformed into a sulfone macrocycle **186** in 55% yield *via* NaH-catalyzed alkylation, followed by $NaBO_3{\cdot}4H_2O$-catalyzed oxidation (Scheme 57a). Crystal structure analysis revealed that thiapillar[6]arene **185** featured a symmetrical macrocyclic cavity with a 12 Å distance between opposing sulfur atoms and 10 Å between phenyl rings, stabilized through weak intermolecular interactions (Scheme 57b). In contrast, **186** adopted a distorted "open book" conformation with reduced symmetry, characterized by alkoxy-substituted phenyl rings separated by 9 Å and a cavity width of 14 Å (Scheme 57c). In addition, **186** exhibited strong FQY (43%), attributed to D–A interactions between the appended groups and the electron-deficient sulfone cavity.

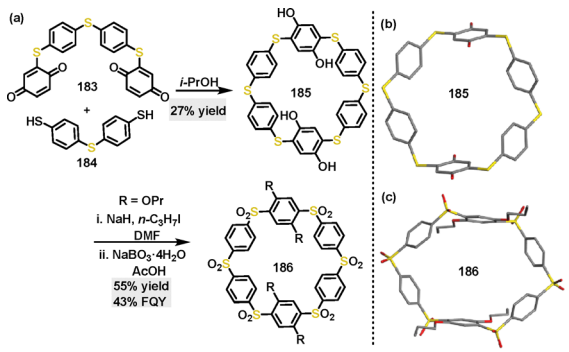

Scheme 57 (a) Synthesis and (b) and (c) crystal structures of **185 and 186**.

5. N,O- and N,S-doped macrocycles

The synergistic incorporation of two types of heteroatoms (*e.g.*, N,O- and N,S-pairs) can significantly tune the electronic structure, coordination selectivity, dynamic responsiveness, and functional applications of macrocyclic compounds.[101,102] Interactions among heteroatoms, including electronic effects, steric hindrance, and synergistic coordination, can overcome the limitations of single-heteroatom systems, enabling the integration of more complex functionalities. For instance, aza-18-crown-6-ethers[103] and diaza-18-crown-6 ethers[104] exhibit remarkable versatility in heavy metal adsorption, catalysis, sensing, supramolecular assembly, and biomedicine. Their unique properties arise from N,O-synergistic coordination and distinct electronic environments, offering advantages over traditional crown ethers such as enhanced metal selectivity, dynamic responsiveness, and biocompatibility.[105]

5.1. Metal catalysis and N,O-doped macrocycles

5.1.1. Palladium catalysis. In 2024, Singh[106] reported an oxidative homocoupling approach for the preparation of a D–A macrocycle in 18% yield under $Pd(PPh_3)_2Cl_2$ catalysis conditions (Scheme 58a). To address solubility issues during the subsequent macrocyclization, 2-ethylhexyl alkyl chains on substrate

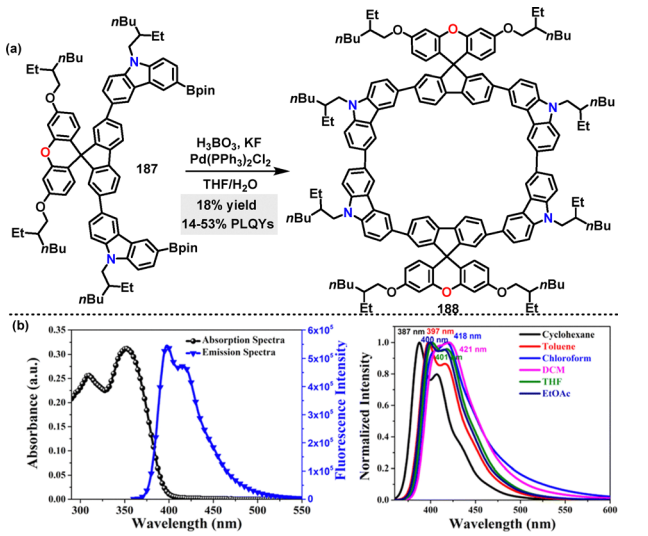

Scheme 58 (a) Synthesis of D–A macrocycle **188**, (b) UV-vis and fluorescence spectra of macrocycle **188** (left) and emission spectra in solvents of increasing polarity (right). Reproduced from ref. 106 with permission from The Royal Society of Chemistry, copyright 2024.

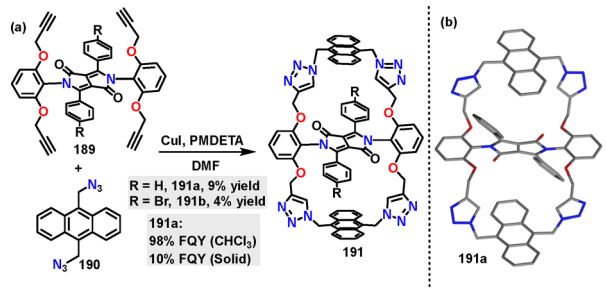

Scheme 59 (a) Synthesis and (b) crystal structure of diketopyrrolopyrrole-bridged bis-anthracene macrocycle **191**.

187 were employed for *O*-alkylation of the generated spiro-[fluorene-9,9′-xanthene] (SFX) core. Using the space-charge-limited current method, macrocycle **188** demonstrated nearly balanced charge carrier mobilities with a hole mobility of 4.75×10^{-3} $cm^2 V^{-1} s^{-1}$ and an electron mobility of 1.0×10^{-3} $cm^2 V^{-1} s^{-1}$. In optical studies, macrocycle **188** displayed absorption peaks at 397 nm and 416 nm in nonpolar solvents, which shifted to 421 nm in polar DCM (Scheme 58b), indicative of positive solvatochromism. Additionally, macrocycle **188** exhibited strong solvent-dependent PLQY, ranging from 14% in cyclohexane, to 53% in toluene.

5.1.2. Copper catalysis. In 2024, Wang[107] reported a Cu-catalyzed azide–alkyne cycloaddition (CuAAC) for constructing a diketopyrrolopyrrole (DPP)-bridged bis-anthracene macrocycle **191**. The targeted doubly anthracene-strapped DPP macrocycles bearing H and Br substituents were obtained in 9% and 4% yields, respectively (Scheme 59a). Crystal structure analysis revealed that macrocycle **191a** adopted a *Z*-shaped conformation, with anthracene straps shielding the DPP core (Scheme 59b). In $CHCl_3$ solution, **191a** exhibited a near-unity quantum yield (98%). In the solid state, thin films of **191a** showed a moderate FQY (10%).

5.2. Metal-free and N,O-doped macrocycles

5.2.1. Brønsted acid catalysis. In 2023, Ma[108] reported a streamlined synthesis of calix[3]phenoxazine *via* CF_3COOH-catalyzed one-pot F–C cyclization of phenoxazine monomers **192** with substituted aldehydes. The N,O-doped macrocycles **193** bearing alkyl chains or aromatic moieties were obtained in 30–70% yield using DCE as the solvent (Scheme 60a). Crystal structure analysis showed that **193a** adopted a cone-shaped conformation featuring a symmetrical cavity (7.7 Å) with phenoxazine units arranged in a butterfly configuration (Scheme 60b). The emission spectra of **193** exhibited maxima >500 nm with large Stokes shifts (100 nm), suggesting potential applications in laser materials and fluorescence-based dosimetry. Cyclic voltammetry of **193a** revealed three quasi-reversible oxidation waves, each corresponding to its three phenoxazine units, highlighting its utility in optoelectronic materials.

In 2025, Mao[109] developed a F–C alkylation of substituted phenoxazines **194** with paraformaldehyde for the construction of calix[*n*]phenoxazines. Macrocycles **195** bearing different substitutions on the N-atom were generated in 5–70% yields under CF_3COOH conditions (Scheme 61a). Crystal structure analysis

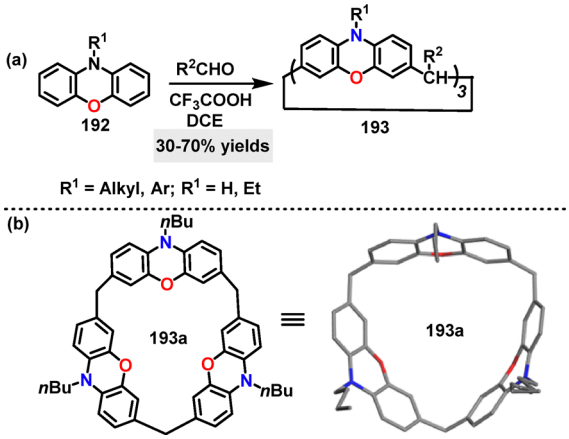

Scheme 60 (a) Synthesis of N,O-doped macrocycles **193** and (b) crystal structure of **193a**.

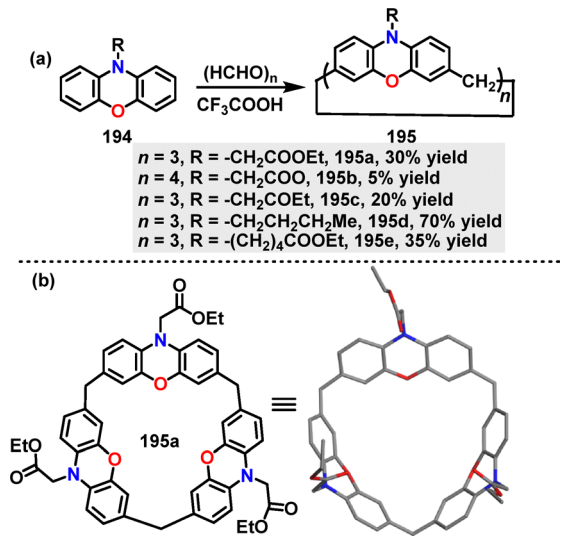

Scheme 61 (a) Synthesis of calix[*n*]phenoxazines **195** and (b) crystal structure of **195a**.

showed that **188a** adopted a symmetrical cone-shaped conformation with three ester carbonyl groups oriented toward the cavity, forming a pumpkin-shaped binding pocket (8.0 Å diameter, 4.8 Å height) (Scheme 61b).

5.2.2. Brønsted base catalysis. In 2020, Wang reported a novel N,O-doped macrocycle *via* a one-pot nucleophilic aromatic substitution reaction.[110] Under *N*,*N*-diisopropylethylamine (DIPEA) conditions, the trimeric macrocycle **198** was generated in 43% yield through C–O bond formation. Crystal structure analysis revealed that **198** adopted a nearly planar hexagonal arrangement with three tetrazine centroids forming an equilateral triangle (Scheme 62).

In 2021, Hirsch[111] reported the synthesis of perylene bisimide cyclophane macrocycles **200** *via* pyridine-promoted macrocyclization ($n + n$, $n = 2, 3, 4$). Macrocycles **200** with diverse ring sizes and flexible malonate linker moieties were obtained in 8.1%, 3.4%, and 1.3% yields, respectively (Scheme 63). Notably,

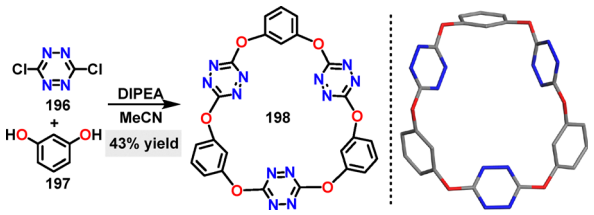

Scheme 62 Synthesis and crystal structure of macrocycle **198**.

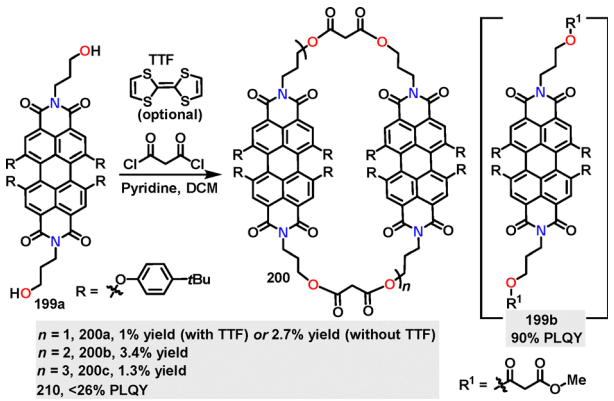

Scheme 63 Synthesis of perylene bisimide cyclophane macrocycles **200**.

employing electron-donating tetrathiafulvalene (TTF) as a template enhanced the yield of **200** from 2.7% to 8.1%. Monomeric **199b** displayed a vibrationally resolved absorption spectrum with a maximum at 603 nm and a shoulder at 655 nm, featuring a high PLQY of 90% in toluene. This behavior is attributed to minimal π–π interactions and efficient radiative decay. In contrast, macrocycles **200** exhibited a reduced PLQY (<26%) due to π–π stacking-induced excited-state quenching, accompanied by emission maxima redshifted to 610–615 nm.

In 2023, Kumagai[112] reported the synthesis of a novel oxa-triquinoline **202**, a macrocycle incorporating three quinoline units and three ether O-atoms in 43% yield, *via* one-pot trimerization of a 2-fluoro-8-quinolinol monomer **201** under K_2CO_3 conditions (Scheme 64a). Crystal structure analysis revealed a bent molecular conformation of **202** (Scheme 64b).

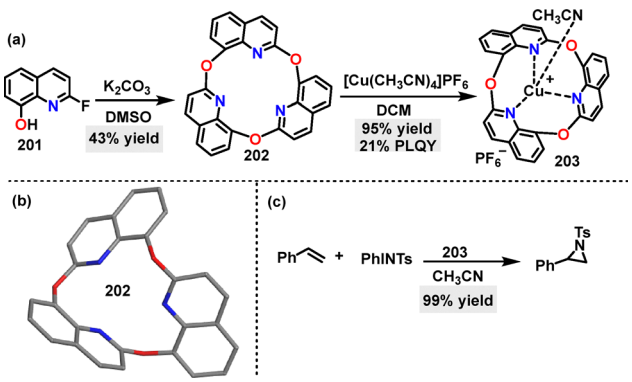

Scheme 64 (a) Synthesis of oxa-triquinoline **202** and Cu-complex **203**, (b) crystal structure of **202**, and (c) the catalytic activity of complex **203**.

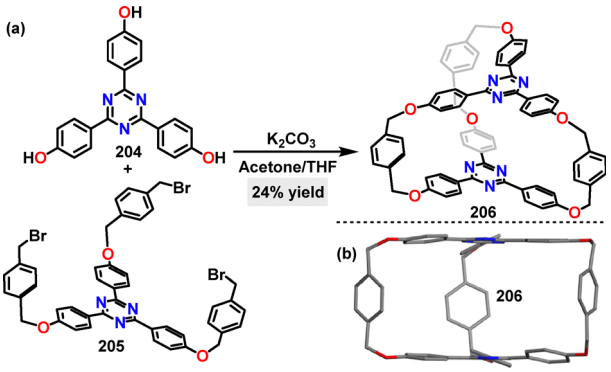

Scheme 65 (a) Synthesis and (b) crystal structure of cage-macrocycle **206**.

Notably, macrocycle **202** coordinated with $[Cu(CH_3CN)_4]PF_4$ in DCM, inducing a bowl-shaped geometry and forming the **203** complexes in 95% yield. Moreover, this complex served as an effective catalyst, competently mediating the reaction between styrene and PhINTs (Scheme 64c).

In the same year, Chou[113] reported the synthesis of a macrocyclic acceptor-cage in 24% yield *via* K_2CO_3-mediated F–C alkylation (Scheme 65a). Crystal structure analysis of the cage-macrocycle **206** revealed a threefold-symmetric structure featuring two triphenyltriazine "lids" flanked by three xylylene bridges (Scheme 65b).

Recently, Barendt[114] reported the synthesis of a chiral bis-perylene diimide macrocycle **208** in 6% yield *via* a [2+2] macrocyclization reaction using pyridine as the base (Scheme 66a).

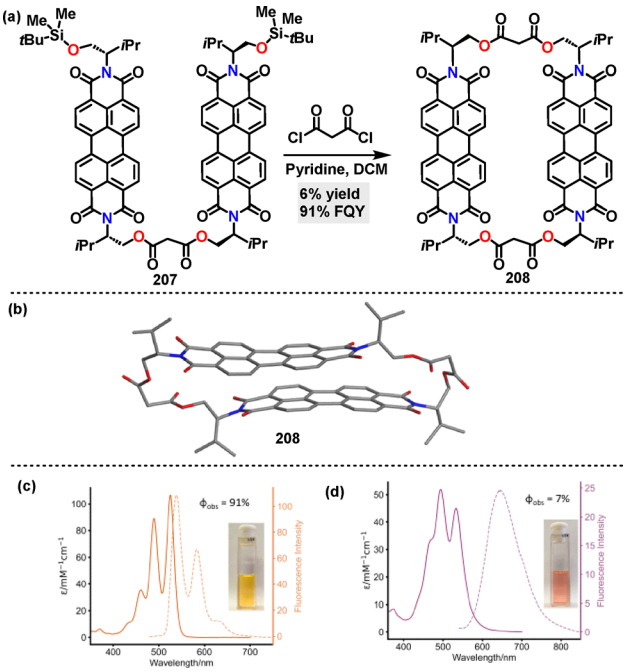

Scheme 66 (a) Synthesis and (b) crystal structure of chiral bis-perylene diimide macrocycle **208**, (c) absorption and emission spectra of macrocycle **208** in $CHCl_3$, and (d) absorption and emission spectra of macrocycle **208** in H_2O. Reproduced from ref. 114 with permission from Wiley-VCH, copyright 2025.

Crystal structure analysis of macrocycle **208** revealed a closed conformation with D_2 symmetry, characterized by a π–π stacking distance of 3.3 Å (Scheme 66b). This structure was stabilized by intramolecular π–π interactions and solvent molecules encapsulated within the cavity. Fluorescence spectroscopy revealed solvent and guest-dependent emission behavior for macrocycle **208**. In chloroform, the monomeric state exhibited high FQY (91%) and a small Stokes shift (13 nm) (Scheme 66c). In water, intramolecular π–π stacking induced the formation of an excimer, leading to broad emission with a large Stokes shift (130 nm) and significantly quenched emission (7%) (Scheme 66d).

5.2.3. Other conditions. In 2023, He[115] reported a one-pot strategy for constructing self-assembled macrocycles, where solvent polarity and solubility dictate the selective formation of distinct macrocycle architectures. Upon condensing dialdehyde and diamine, the desired [1+1] macrocycle **211** was obtained in 97% yield in MeOH, or in 98% yield in EtOH. Conversely, performing the same condensation in DMSO, DMF, or MeCN yielded the [2+2] macrocycle **212** in 91%, 75%, and 39% yields, respectively (Scheme 67a). Crystal structure analysis revealed that the [1+1] macrocycle **211** adopted a near-planar conformation with a bound water molecule in its cavity, stabilized by hydrogen bonds between pyrrolic NH protons and imine nitrogen atoms (Scheme 67b). In contrast, the [2+2] macrocycle **212** exhibited a chair-like geometry (Scheme 67c).

5.3. Metal catalysis and N,S-doped macrocycles

5.3.1. Palladium catalysis. In 2022, Liu, Lu, Zhao and coworkers[116] reported an efficient method for the construction of N,S-codoped macrocycles featuring branched alkyl substituents. Palladium-catalyzed Suzuki coupling reactions yielded diverse functional macrocycles **214** containing alternating dibenzo[*b*,*d*]thiophene and carbazole units in 12–14% yields.

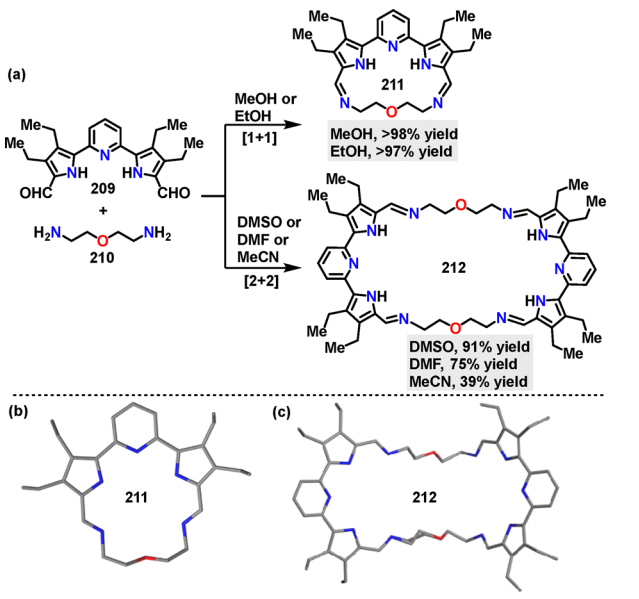

Scheme 67 (a) Synthesis and (b) and (c) crystal structures of chiral bisperylene diimide macrocycles **211 and 212**.

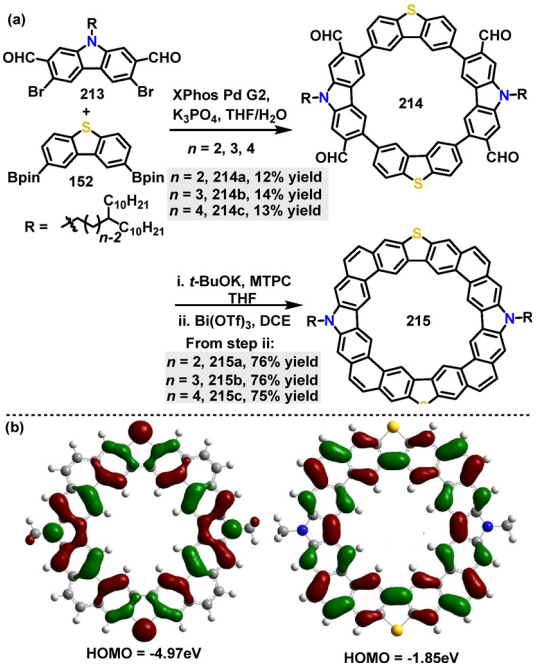

Scheme 68 (a) Synthesis and modification of N,S-codoped macrocycle **214** and (b) Frontier orbitals and energy levels of this series of N,S-embedded macrocycles **225**. Reproduced from ref. 116 with permission from American Chemical Society, copyright 2022.

Furthermore, alkyl-substituted fully fused macrocycles **215** were obtained in 75–76% yields *via* sequential base-catalyzed Wittig reactions and $Bi(OTf)_3$-catalyzed cyclization (Scheme 68a). DFT calculations revealed that the electron-rich N-atoms in these planar macrocycles elevate the energies of both the HOMO (−4.97 eV) and the LUMO (−1.85 eV), reducing the energy gap to 3.12 eV and identifying them as promising candidates for p-type semiconductors (Scheme 68b).

In 2023, Yuan[117] reported the synthesis of a cyclic conjugated macrocycle **218** featuring a multicomponent D–A architecture. The π-conjugated macrocycle **218** was efficiently synthesized in 60% yield *via* a palladium-catalyzed Stille coupling reaction (Scheme 69). Macrocycle **218** demonstrated a high PLQY of 11% in solution and 4% in the solid state, significantly higher

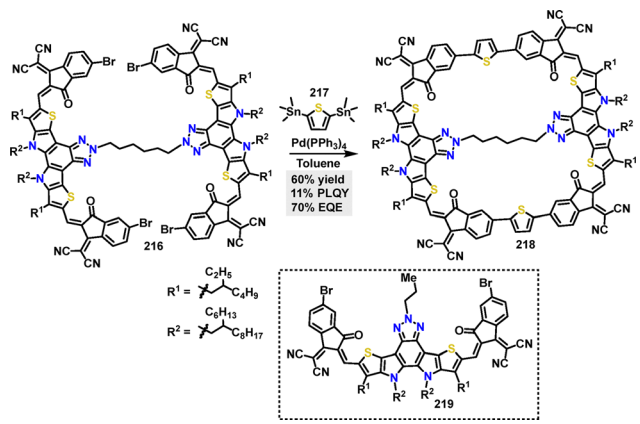

Scheme 69 Synthesis of cyclic conjugated macrocycle **218**.

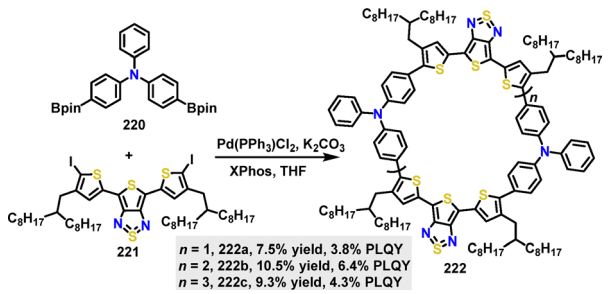

Scheme 70 Synthesis of D–A macrocycle **222**.

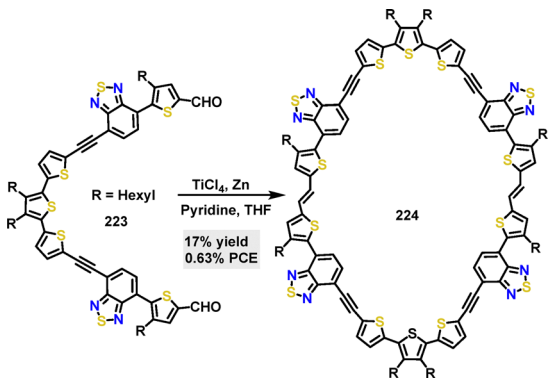

Scheme 71 Synthesis of D–A macrocycle **224**.

than its linear analogue **219** (2%). This enhancement was attributed to reduced molecular vibrations enabled by the rigid macrocyclic structure, which suppressed nonradiative decay. TGA revealed superior thermal stability for macrocycle **218**, with 5% weight loss occurring at 393.8 °C (*vs.* 330.3 °C for **219**).

In 2024, Wan[118] and co-workers reported a series of D–A macrocycles **222** *via* a one-pot Suzuki cross-coupling reaction. Under palladium catalysis, D–A dimeric macrocycle **222a**, trimeric macrocycle **222b**, and tetrameric macrocycle **222c** were selectively formed in [2+2], [3+3], and [4+4] cyclization pathways with yields of 7.5%, 10.5%, and 9.3%, respectively (Scheme 70). The trimeric macrocycle **222b** demonstrated an optimal balance between ring strain and conformational flexibility, achieving the highest PLQY of 6.4% due to mixed conformations and allowed electronic transitions. Smaller macrocycle **222a** suffered from high ring strain, resulting in lower PLQY (3.8%), while larger tetramers **222c** showed moderate PLQY (4.3%) attributed to the stability of transoid conformations.

5.3.2. Titanium catalysis. In 2021, Cooke[119] reported the synthesis of a thiophene-based conjugated macrocycle *via* a one-pot Sonogashira reaction. Using a $TiCl_4$/Zn reagent system, the D–A macrocycle **224** featuring electron-deficient benzothiadiazole (BT) units was obtained in 17% yield (Scheme 71).

5.4. Metal-free and N,S-doped macrocycles

5.4.1. Lewis acid catalysis. In 2022, Li[120] reported an efficient synthetic method for constructing a benzothiadiazole(BT)-based macrocycle. The target macrocycle **226**, incorporating a dimethoxyphenyl donor and 2,1,3-benzothiadiazole acceptor, was

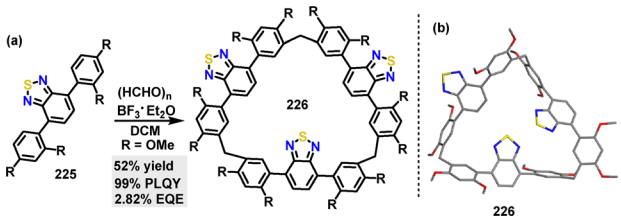

Scheme 72 (a) Synthesis and (b) crystal structure of benzothiadiazole-based macrocycle **226**.

synthesized in 52% yield *via* a one-pot condensation of BT precursors **225** with paraformaldehyde, using $BF_3{\cdot}Et_2O$ as a Lewis acid catalyst (Scheme 72a). Crystal structure analysis revealed that macrocycle **226** adopted a rigid triangular conformation, where C(sp^3) bridges restrict the rotation of benzothiadiazole and phenyl groups, thereby reducing conformational flexibility (Scheme 72b). Macrocycle **226** demonstrated an exceptionally high PLQY of 99%, significantly exceeding that of monomer **225** (65%). Additionally, macrocycle **226** showed a longer fluorescence lifetime (11.25 ns) than monomer **225** (8.45 ns), indicating reduced nonradiative relaxation in the macrocycle.

In 2023, Ravikanth[121] reported the synthesis of DBTh-containing thiacarbaporphyrinoids under acidic conditions. Macrocycles **229** were obtained in 7–8% yields *via* the condensation of pentapyrranes **227** with thiophene diols **228** in the presence of $BF_3{\cdot}OEt_2$, followed by DDQ-mediated oxidation (Scheme 73a). Crystal structure analysis of compound **229b** revealed a nonplanar macrocyclic structure (Scheme 73b).

In 2024, Lin[122] reported the synthesis of a calix[3]phenothiazine macrocycle **231** featuring rigid cavitand structures for guest encapsulation. Under $BF_3{\cdot}OEt_2$ catalysis, this macrocyclic donor molecule was obtained in 47.1% yield *via* a one-pot cyclization reaction (Scheme 74).

In 2025, Gokulnath[123] designed and synthesized two rigid dithienopyrrole (DTP)-based macrocycles **233** and **234** *via* a

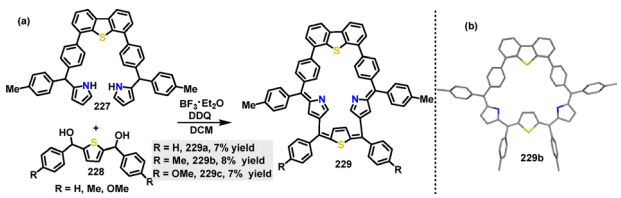

Scheme 73 (a) Synthesis of thiacarbaporphyrinoids **229** and (b) crystal structure of **229b**.

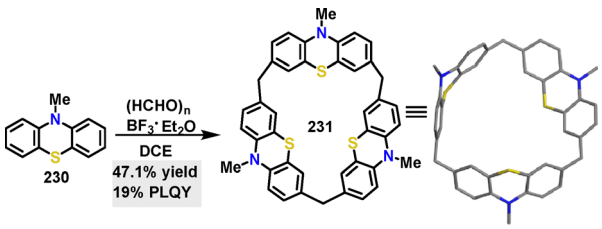

Scheme 74 Synthesis and crystal structure of macrocycle **241**.

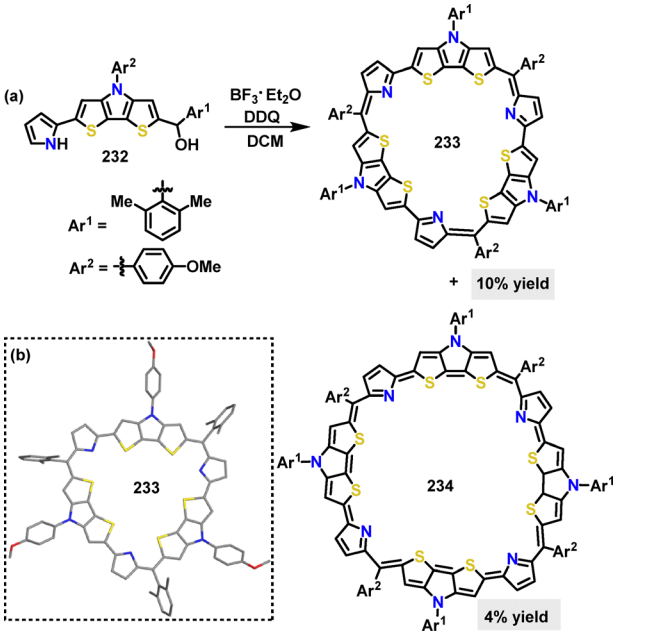

Scheme 75 (a) Synthesis of dithienopyrrole-based macrocycles **233** and **234**, and (b) crystal structure of **233**.

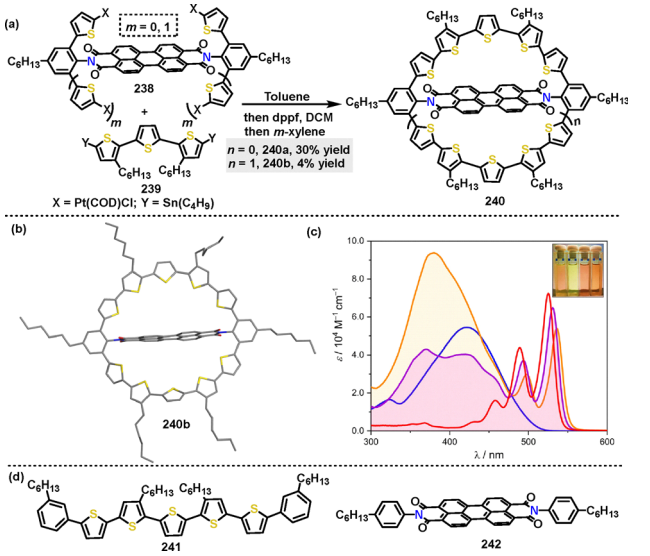

Scheme 77 (a) Synthesis of perylene bisimide-based macrocycle **240**, (b) crystal structure of **240b**, (c) UV-vis absorption spectra of **240a** (purple line), **240b** (orange line), **241** (blue line) and **242** (red line) in DCM, and (d) structures of compounds **241 and 242**. Reproduced from ref. 125 with permission from Wiley-VCH, copyright 2022.

macrocyclization reaction. Under $BF_3{\cdot}OEt_2$/DDQ conditions, the cyclotrimer **233** and cyclotetramer **234** were obtained in 10% and 4% yields, respectively (Scheme 75a). Crystal structure analysis of **233** revealed a fully planar conformation, with pyrrolic N-atoms and DTP S-atoms oriented toward the macrocyclic core (Scheme 75b).

5.4.2. Brønsted base catalysis. In 2023, Zhu[124] reported an efficient one-pot cyclization of **235** with 1,4-dibutoxy-2,5-dibromomethylbenzene **236** for the synthesis of a pyrrolodithiin-derived box-like cyclophane **237**. Using NaH as the base, macrocycle **237** was obtained in 21% yield (Scheme 76). Crystal structure analysis revealed that macrocycle **237** adopted a hex-nut-shaped geometry featuring a central cavity (width: 8.95 Å), which is capable of guest encapsulation.

5.4.3. Other conditions. In 2021, Würthner[125] reported a cross-coupling strategy for constructing macrocyclic architectures incorporating perylene bisimide (PBI) units. Macrocycles **240a** and **240b** were synthesized *via* a one-pot protocol in 30% and 4% yields, respectively (Scheme 77a). The lower yield of **240b** was attributed to its higher strain energy (30.6 kJ mol^{-1}) compared to **240a** (13.9 kJ mol^{-1}). Crystal structure analysis of **240b** revealed oligothiophene bridges adopting an all-syn, twisted S-shape that encloses a planar PBI core (Scheme 77b). This geometry exhibited moderate strain (30.6 kJ mol^{-1}), originating from thiophene torsion angles ranging from 68° to 158°, and featured symmetric and slightly deformed molecular motifs. S-atoms in the thiophene units point toward the PBI core, with close S–S distances of 3.37 Å. In UV-vis spectroscopy, the strong, low-energy absorption bands of **240a** and **240b** at 530–536 nm (54 000–64 800 M^{-1} cm^{-1}; Scheme 77c), originating from their PBI core and absent in **241** and **242**, collectively demonstrate the pivotal role of ring strain in both the synthesis and the resulting structure–absorption relationship of PBI-based oligothiophene macrocycles.

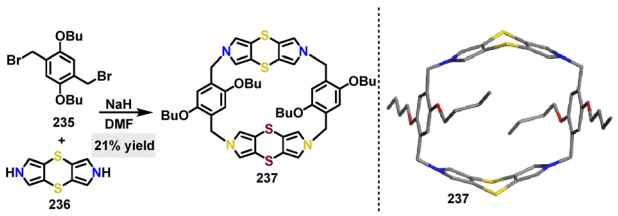

Scheme 76 Synthesis and crystal structure of **237**.

6. Applications of heteroatom-doped macrocycles

Benefiting from their heteroatom-doped architectures, novel macrocycles exhibit intriguing host–guest properties, enabling the selective recognition of diverse neutral, cationic, and anion molecules. Furthermore, their tunable photophysical characteristics allow them to serve as highly selective chemosensors, operating *via* distinct fluorescence turn-on or turn-off mechanisms. Beyond molecular recognition and sensing, these functional macrocycles have also found broad range of applications in organic electronic devices (*e.g.*, OLEDs, OFETs, and OSCs), catalysis, and molecular adsorption and separation applications.

6.1. Molecular recognition

6.1.1. Recognition of neutral guests. The design of synthetic macrocyclic hosts capable of selective molecular recognition is a central theme in supramolecular chemistry. In 2022, Komori reported the host–guest properties of acridone-incorporated

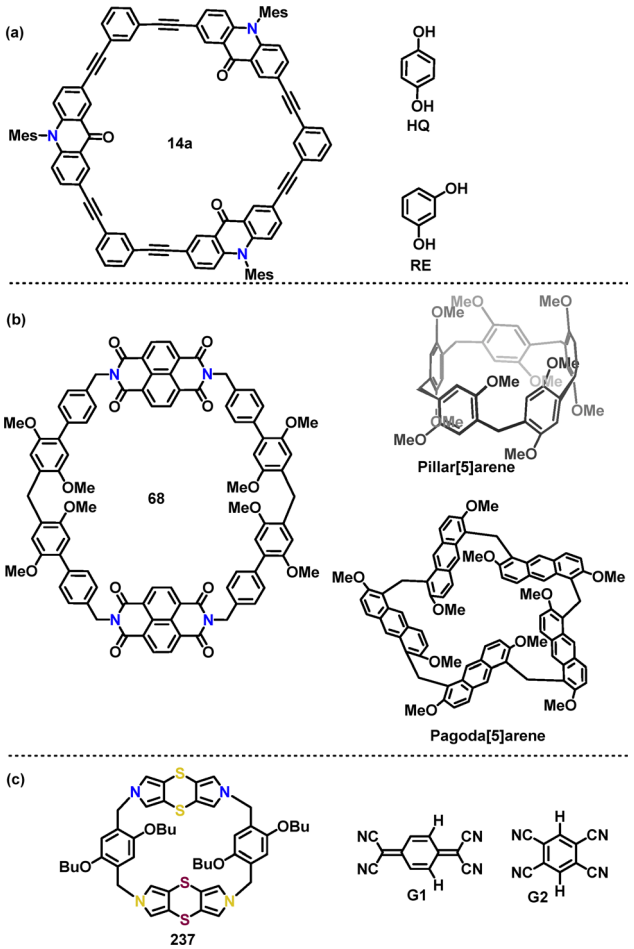

Fig. 2 Structures of (a) host **14a** and guests **HQ**, **RE**, (b) host **68** and guests pillar[5]arene, pagoda[5]arene, (c) host **237** and guests **G1** and **G2**.

arylene-ethynylene macrocycles **14a**, with a particular focus on their ability to bind dihydric phenolic guests (G) *via* hydrogen bonding (Fig. 2a).[31] The cyclic trimer **14a**, which featured a planar hexagonal cavity lined with three carbonyl groups, was found to form 1:1 host–guest complexes with phenolic species such as hydroquinone (**HQ**) of binding affinity (K_a) $(1.00 \pm 0.09) \times 10^3$) and resorcinol (**RE**) of K_a $(0.99 \pm 0.14) \times 10^3$).

In 2023, Zeng's group designed a giant electron-deficient macrocycle, naphthalene diimide-extended-pillar[6]arene **68**. In contrast to its negligible interaction with pillar[5]arene, macrocycle **68** displayed exceptional selectivity for pagoda[5]arene, forming a 1:1 inclusion complex with a K_a of $(1.77 \pm 0.04) \times 10^5$ M^{-1} (Fig. 2b). The complexation process was marked by a significant color change and the rise of a new broad absorption feature at 600–800 nm, underscoring the formation of a charge-transfer complex stabilized by strong intermolecular interactions.[47]

Later, Zhu demonstrated the host–guest binding behavior of macrocycle **237**, exhibiting remarkable adaptability toward electron-deficient guests **G1** and **G2** with varying sizes and geometries (Fig. 2c), with K_a values of 1.2×10^4 M^{-1} and 1.6×10^4 M^{-1}, respectively (Scheme 72c).[124] In the presence of **G2**, the cyclic voltammetry (CV) profile of **237** changed significantly (from −0.50 to 0.60 V), indicating a two-electron oxidation process that led to the release of the guest due to charge repulsion. This redox-triggered dissociation demonstrated the potential of macrocycle **237** as a switchable molecular host for controllable supramolecular systems.

In 2024, Chen, Lin, and coworkers introduced a pioneering supramolecular strategy to construct efficient organic scintillators, moving beyond traditional covalent synthesis by leveraging programmable host–guest interactions.[122] When complexed with guests **G3** and **G4** (Fig. 3a), macrocycle **231** formed supramolecular co-crystals **G3@231** (K_a: 540 M^{-1}) and **G4@231** (K_a: 2.9×10^4 M^{-1}) that exhibited TADF properties (Fig. 3c). **G3@231** emitted green light at 541 nm with CIE coordinates (0.36, 0.56), whereas **G4@231** displayed orange emission at 633 nm (CIE: 0.39, 0.58). The red-shifted emission in **G4@231** was attributed to the heavy-atom effect of bromine in the guest molecule (Fig. 3b). Notably, under N_2, the PLQY values of **G3@231** (73%) and **G4@231** (34%) were significantly higher than that of macrocycle **231** (19%). This enhancement arose from molecular structure rigidification and suppression of nonradiative decay mediated by strong noncovalent host–guest interactions.

Recently, Wong and Chou presented a detailed thermodynamic analysis of inclusion complexes between a macrocyclic, triazine-based electron-accepting host **206** and various electron-donating guests, with K_a ranging from 852 M^{-1} to 1.5×10^3 M^{-1} (Fig. 4a). Moreover, **G5@206** was found to be an endothermic and entropy-driven process, which was attributed to the release of solvent molecules (*e.g.*, DCM) from the host cavity upon guest inclusion.[113]

In 2025, Barendt presented the intrinsic cavity and conformational flexibility of the chiral bis-perylene diimide (PDI) macrocycle **208**, making it an exceptional host for studying tunable host–guest interactions.[114] Macrocycle **206** demonstrated strong binding to **G9** (K_a: 3.8×10^4 M^{-1}) through cavity-based π–π stacking, forming 1:1 host–guest complexes (Fig. 4b). These

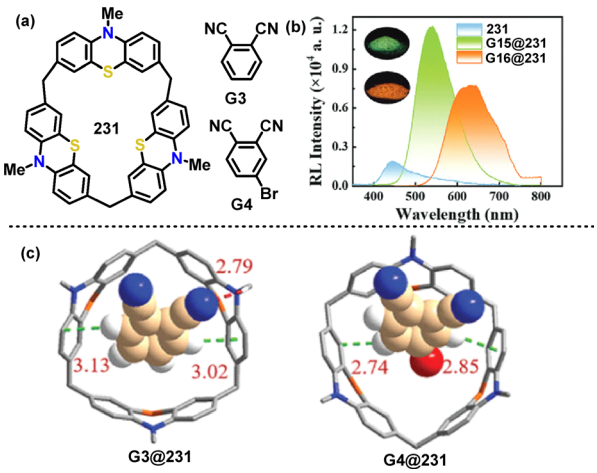

Fig. 3 (a) Structures of host **231** and neutral guests **G3** and **G4**, (b) radioluminescence spectra of **231**, **G3@231**, and **G4@231**, and (c) diagram of crystal structures of **G3@231** and **G4@231**. Adapted from ref. 122 with permission from Wiley-VCH, copyright 2024.

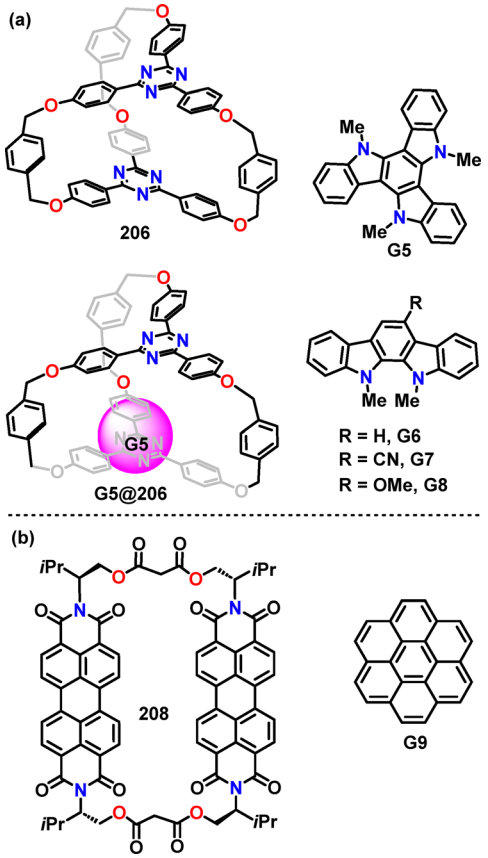

Fig. 4 Structures of (a) **206**, **G5@206**, and guests **G5**–**G8**, (b) **208,** and guest **G9**.

complexes exhibited charge-transfer exciplex emission with a significant emission shift (116 nm), highlighting the macrocycle's ability to modulate photophysical properties through guest inclusion.

The recognition of fullerenes such as C_{60} and C_{70} by macrocyclic hosts is well-established. In 2020, Yang and coworkers reported the saddle-shaped, S-containing heterocycloarene S-octulene **154**.[88] Its distinctive three-dimensional geometry, which possessed a vertical extent of 4.6 Å, provided a complementary cavity for the curved surfaces of fullerenes. This structural complementarity was quantitatively confirmed by binding studies in toluene, which revealed a higher association constant for C_{60} (K_a: 1.25 × 10^6 M^{-1}) than that for C_{70} (K_a: 9.49 × 10^6 M^{-1}), indicating a discernible preference and stronger host–guest interaction with C_{60} (Fig. 5a).

Later, Zhan introduced the fully conjugated nanohoop **164**, which featured a unique architecture combining strained oligo-paraphenylene loops and a flexible COTh core.[91] This synergy endowed it with guest-adaptive cavities, a property spectacularly demonstrated by X-ray structures of its 2C_{60}@**164** and 2C_{70}@**164** complexes (Fig. 5b). These peanut-like assemblies constituted the first isolable 1:2 complexes of their kind, wherein the host's cavities underwent distinct unsymmetrical distortions to encapsulate the different fullerenes, stabilized by significant π–π interactions between the complementary curved surfaces.

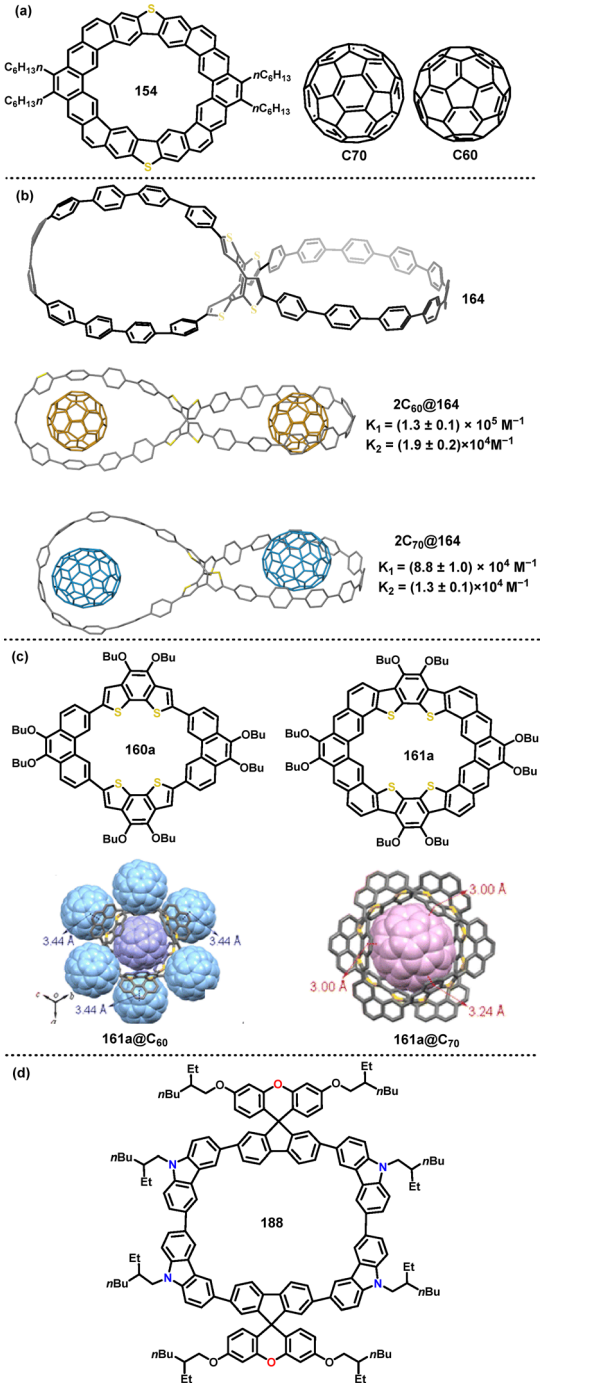

Fig. 5 Structure of (a) **154** and guests C_{60}, C_{70}, (b) **164**, and co-crystals 2C_{60}@**164**, 2C_{70}@**164**, (c) **160a**, **161a**, and co-crystals **161a**@C_{60}, **161a**@C_{70}, (d) **188**. Reproduced from ref. 90 with permission from The Royal Society of Chemistry, copyright 2024.

In 2024, Liu, Lu and coworkers investigated the host–guest properties of π-conjugated macrocycle **160a** and its fully fused heterocycloarene analogue **161a**, revealing pronounced size- and geometry-dependent binding preferences toward C_{60} and C_{70}.[90] For instance, **160a** showed stronger binding to C_{70} (K_a: 2.44 × 10^5 M^{-1}) than to C_{60}, attributed to better geometric complementarity. Conversely, **161a** exhibited higher affinity for

C_{70} (K_a: 1.62 × 10^5 M^{-1}) due to its bowl-shaped cavity, which accommodated the ellipsoidal C_{70} guest (Fig. 5c). In the same year, Singh and co-workers reported macrocycle **188**, an ambipolar system constructed from alternating spirofluorene-9,9′-xanthene (SFX) and carbazole units.[106] This nanoring possessed a well-defined cavity with internal dimensions suitable for guest encapsulation, and it exhibited strong host–guest binding with C_{60} (K_a: 9.95 × 10^4 M^{-1}), which was primarily mediated by noncovalent interactions (Fig. 5d).

6.1.2. Recognition of cationic guests. In 2021, Qu and Feringa introduced two macrocyclic hosts by integrating a first-generation molecular motor into a crown-ether-like structure.[84] The stable-***cis*-148b**, adopting a folded conformation, exhibited strong and selective 1:1 binding with dialkylammonium guests (*e.g.*, K_a: 219.0 M^{-1} for **G10**, K_a: 162.4 M^{-1} for **G11**) *via* hydrogen bonds and ion–dipole interactions (Fig. 6a). In stark contrast, the stable-***trans*-148b**, which adopted a more linear and stretched conformation, showed negligible binding affinity (K_a < 1 M^{-1}) for the same guests. In the same year, Li reported that macrocycle **136** exhibited selective binding for cationic guests (Fig. 6b),[79] driven by cation–dipole interactions (between cationic centers and electron-rich furan O-atoms) and CH–π interactions (between alkyl protons of the guests and π-electron clouds of the furan rings). For instance, **G12** binds most strongly due to its optimal size, which fitted well within the macrocycle's cylindrical cavity of (4.1 ± 1.4) × 10^3 M^{-1} (K_a). In contrast, **G13** was too large, leading to steric repulsion and a weaker binding K_a of (1.2 ± 0.2) × 10^3 M^{-1}.

Later, the group of Jiang systematically investigated the host–guest complexation behaviour of methylene-bridged naphthotubes (Fig. 6c).[82] For example, **143a** exhibited strong binding affinity toward organic cations **G14** and **G15** (*e.g.*, K_a: (1.7 ± 0.2) × 10^5 M^{-1} for **G14**; (5.1 ± 0.2) × 10^3 M^{-1} for **G15**), attributed to its rigid, electron-rich cavity (Scheme 41d). In contrast, **143d** showed weaker binding (K_a: 10^2–10^3 M^{-1} for **G14**) due to double-cavity distortion and charge repulsion.

In 2023, Yang systematically investigated the host–guest chemistry of N-embedded cubarene **61** (Fig. 6d).[43] The macrocycle was found to form stable, intramolecular complexes with a series of quaternary ammonium salts. Notably, high binding affinities were quantified for specific guests, with K_a values reaching (5.33 ± 0.70) × 10^5 M^{-1} for **G16** and (5.31 ± 0.50) × 10^5 M^{-1} for **G17**.

Recently, Ma and colleagues demonstrated that the cone-shaped calix[3]phenoxazine **193a** formed 1:1 host–guest complexes with quaternary ammonium salts, leveraging its electron-rich, well-defined cavity (Fig. 6e).[108] The binding affinity was critically dependent on guest size and structure, with the K_a for ammonium salt **G18** (featuring a trimethylammonium head and a hexyl chain) being (1.66 ± 0.15) × 10^3 M^{-1}. In sharp contrast, the significantly weaker binding for the smaller guest **G19** (14.6 ± 1.1) M^{-1}) underscored this pronounced size selectivity. Building on this, the same group engineered an ester-functionalized analogue **195a**, in which the pendant carbonyl groups served as auxiliary binding sites.[109] This strategic modification yielded a superior binding affinity (2.61 ± 0.22) × 10^3 M^{-1}) with guest **G19** compared to the non-ester parent macrocycle **193a**, underscoring

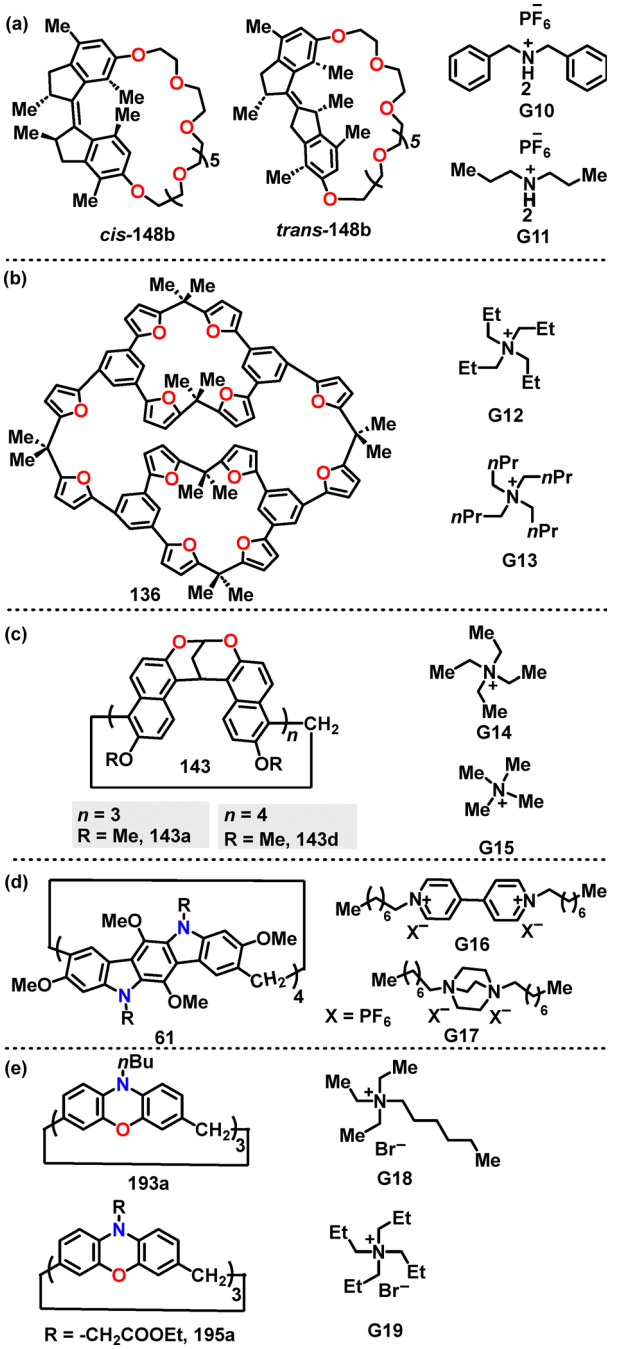

Fig. 6 Structures of ***cis*-148b**, ***trans*-148b**, **136**, **143a**, **143d**, **61**, **193a**, and **195a** and cationic guests **G10–G19**.

the efficacy of side-chain functionalization in enhancing molecular recognition.

6.1.3. Recognition of anion guests. In 2020, Wang reported a novel N,O-doped macrocycle **198**.[110] It showed strong selectivity for nitrate (NO_3^-) (K_a ≈ 2.2 × 10^5 M^{-1}) through a combination of anion–π interactions and hydrogen bonding, forming an [NO_3·**198**]$^-$ complex (Fig. 7a). Later, He and colleagues demonstrated that *cis*-**127** exhibited high selectivity and a K_a of 1.93 × 10^3 M^{-1} for the hydrogen pyrophosphate (HPPi) anion (Fig. 7b), whereas *trans*-**128** showed considerably weaker

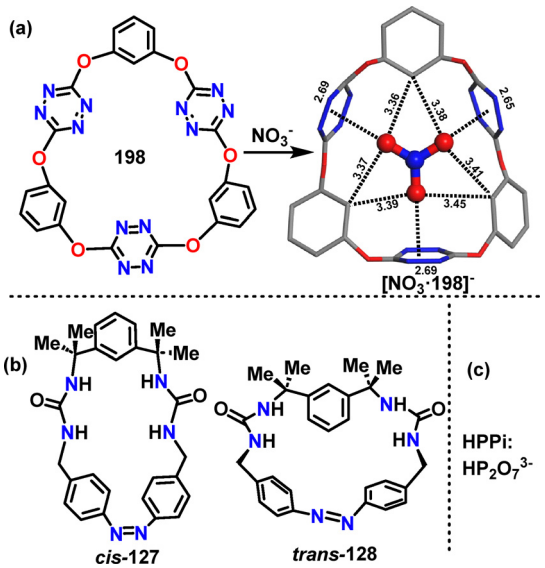

Fig. 7 (a) Single-crystal X-ray molecular structures of **198** complexes with nitrate, (b) structures of *cis*-**127** and *trans*-**128**, and (c) anion guest HPPi.

K_a (2.82×10^2 M^{-1}) for HPPi.[68] DFT calculations revealed that V-shaped *cis*-**127** perfectly complemented the HPPi anion by multiple cooperative hydrogen bonds, engaging all available hydrogen bond donors in the macrocycle. In contrast, the bow-shaped conformation of *trans*-**128** was far less complementary, resulting in fewer hydrogen bonds and a significantly weaker interaction with the guest.

6.2. Molecular sensing

6.2.1. Fluorescence turn-on sensing. In 2021, the Panda group demonstrated that macrocycle **7** served as a highly selective fluorescent sensor for the fluoride ion (F^-) in acetonitrile (Fig. 8).[28] Upon complexation with F^-, the host exhibited a distinct "turn-on" fluorescence response with an emission maximum at 421 nm. This signal enhancement was accompanied by a measured FQY of 30%. Furthermore, the sensor displayed excellent selectivity for F^- over a range of competing anions, including Cl^-, Br^-, I^-, and AcO^-. Fluorimetric titration experiments and Job's plot analysis revealed that the host–guest complexation follows a 1 : 1 stoichiometric ratio.

In 2023, Gong reported a novel tetra-cyanostilbene-based macrocycle **146** that functioned as a "turn-on" blue fluorescence

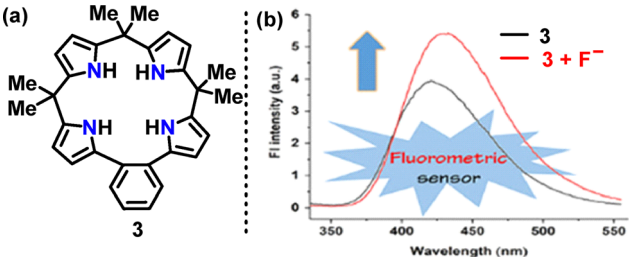

Fig. 8 (a) Structure of macrocycle **3**, and (b) emission spectra of its fluoride complex in acetonitrile. Adapted from ref. 28 with permission from American Chemical Society, copyright 2021.

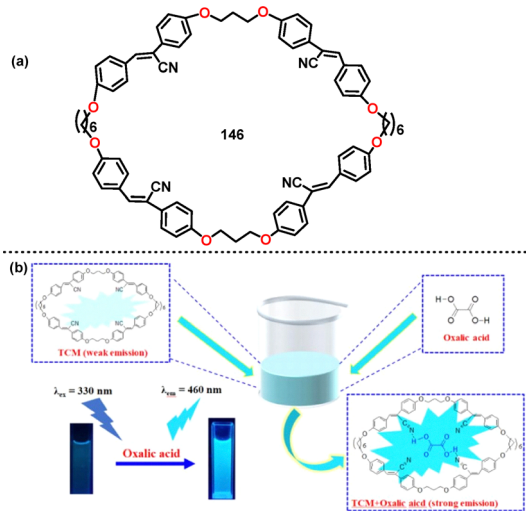

Fig. 9 (a) Structure of macrocycle **146** and (b) the proposed detecting mechanism of **146** for oxalic acid. Reproduced from ref. 83 with permission from Elsevier, copyright 2023.

response for sensing oxalic acid (OA) in aqueous media (Fig. 9).[83] This behavior was attributed to restricted intramolecular rotation (RIR), a characteristic of the AIE effect. The absolute FQY increased from 9% (free **146**) to 55% upon binding with OA. DFT calculations further clarified that the HOMO–LUMO energy gap decreased from 3.50 eV (free **146**) to 3.33 eV (**146**-OA complex), accounting for the observed fluorescence red shift.

In 2024, Keypour and co-workers developed a novel pyrrole-based macrocyclic Schiff base **121** that served as a highly selective fluorescent sensor for Cd^{2+} ions (Fig. 10a).[65] Coordination with Cd^{2+} triggered a distinct "turn-on" response, marked by a 3-fold enhancement in emission intensity at 430 nm, with excellent selectivity over 18 competing metal ions. Later, the group of Yang and Jiang developed a novel D–A phenazine-based

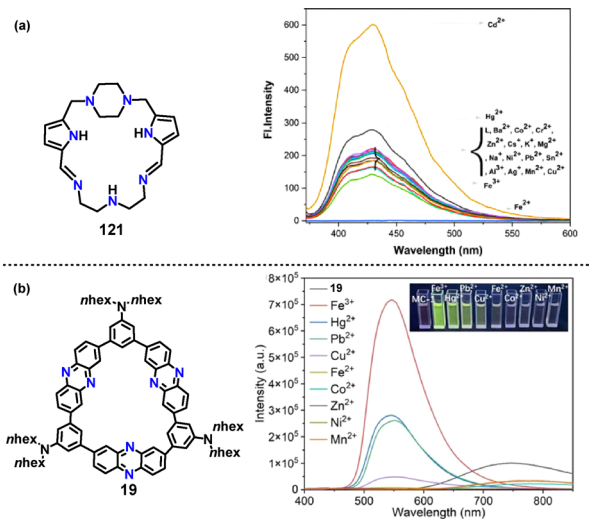

Fig. 10 Structures and fluorescence responses of macrocycles (a) **121** and (b) **19** upon interaction with different metal ions. Reproduced from ref. 65 with permission from Elsevier, copyright 2024.

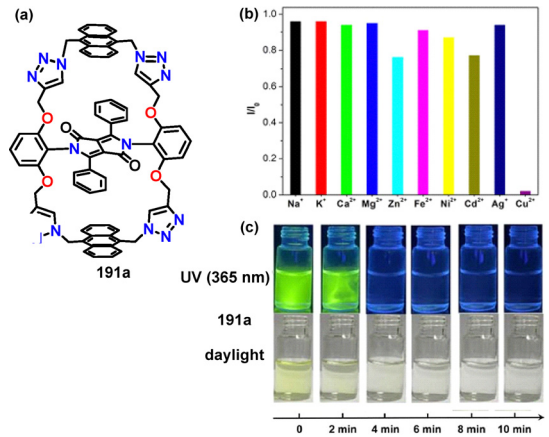

Fig. 11 (a) Structure of macrocycle **191a**, (b) relative fluorescence intensities of **191a** measured upon addition of various metal ions, and (c) the addition of 5 equivalents of Cu^{2+} to acetonitrile solutions of **191a** induced a clear color change. Reproduced from ref. 107 with permission from The Royal Society of Chemistry, copyright 2025.

macrocycle that served as a dual-channel fluorescent sensor for transition metal ions.[32] While most tested ions quenched its near-infrared (NIR) emission, the addition of Fe^{3+} triggered a distinct turn-on response, marked by a strong, blue-shifted emission band at 545 nm (Fig. 10b).

6.2.2. Fluorescence turn-off sensing. In 2025, Sessler reported a highly selective fluorescence turn-off sensor for Cu^{2+} based on a unique diketopyrrolopyrrole (DPP)-centered macrocycle **191a** (Fig. 11a).[107] The addition of 100 equivalents of other metal ions, including Na^+, K^+, Ca^{2+}, Mg^{2+}, Zn^{2+}, Fe^{2+}, Ni^{2+}, Cd^{2+}, and Ag^+, resulted in negligible changes to its fluorescence (Fig. 11b). In stark contrast, the introduction of only 5 equivalents of Cu^{2+} led to an almost complete and rapid quenching of the strong green fluorescence (Fig. 11c).

6.3. Organic electronic devices

6.3.1. OLEDs. In 2020, Minakata developed the novel TADF D–A–D–A π-conjugated macrocycle **43**.[37] An OLED device using macrocycle **43** as the emitter achieved a high EQE of 11.6%, significantly exceeding the 6.9% EQE of devices employing the linear analogue **44** as the fluorescent emitter. This indicated that macrocycle **43** exhibited more efficient TADF than its flexible linear counterpart (Fig. 12a). Later, the group of Yasuda reported the successful implementation of a novel D–A π-conjugated macrocycle **6** as an efficient emitter in OLEDs (Fig. 12b).[29] OLEDs incorporating macrocycle **6** achieved an external quantum efficiency (EQE) of up to 15.7%, *i.e.* four times higher than that of devices using linear **7**. This enhanced EQE arises from macrocycle **6**'s strong TADF capability and favorable molecular orientation in the film, which improves light out-coupling efficiency.

In 2022, Zheng, Zang, and co-workers reported a breakthrough in chiral light-harvesting systems that held significant promise for the development of circularly polarized (CP)-OLEDs.[62] In the chiral 1,1′-bi-2-naphthol-di-octadecylamide BDA/**113**/NiR system (Fig. 13), the circularly polarized luminescence (CPL) signal was transferred to NiR, enabling the generation of bright white-light-emitting CPL

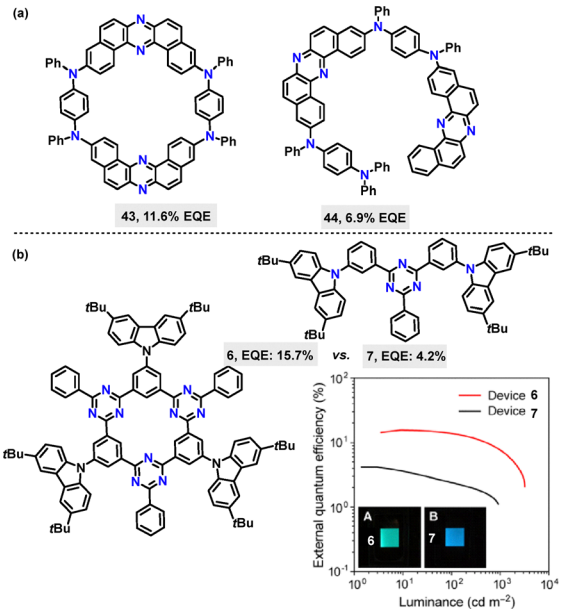

Fig. 12 (a) Structures of macrocycle **43** and linear analogue **44**, (b) structures of macrocycle **6** and linear analogue **7** with their spectra of external EQE. Reproduced from ref. 29 with permission from Wiley-VCH, copyright 2021.

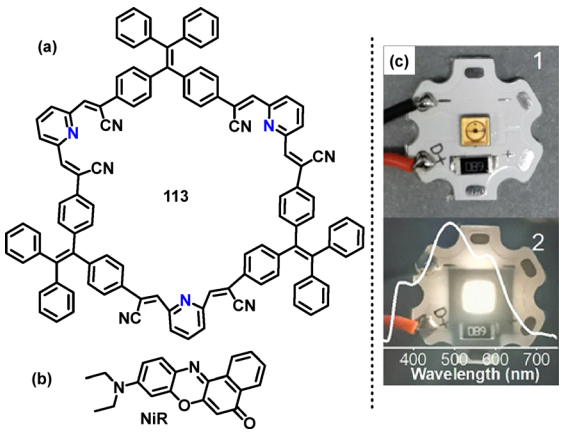

Fig. 13 (a) Structures of macrocycle **113**, (b) compound NiR and (c) photographs of the WLED assembly: a 300 nm UVB LED is coated with BDA/TPEM/NiR (1 and 2: the coated UVB LEDs are turned off and turned on). Reproduced with permission. Reproduced from ref. 62 with permission from American Chemical Society, copyright 2021.

with CIE coordinates of (0.33, 0.34), a QY of 37.3% and a dissymmetrical factor (glum) of 0.025. Moreover, a prototype white-light-emitting diode (WLED) was constructed by depositing the BDA/TPEM/NiR composite onto a commercial ultraviolet B (UVB) LED chip ($\lambda_{ex} \approx 300$ nm), which subsequently emitted bright white light upon operation at 5.5 V.

Later, Li, Bai, and Cui introduced a novel macrocyclization-induced emission enhancement (MIEE) to significantly boost the solid-state luminescence efficiency of organic chromophores.[120] Owing to its D–A structure, macrocycle **226** exhibited a red-shifted emission at 562 nm (orange-red), compared to **225**, which emitted

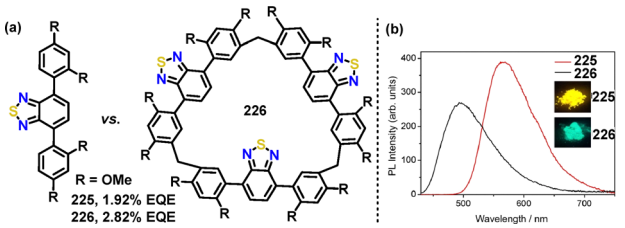

Fig. 14 Structures of (a) compound **225** and macrocycle **226**, and (b) their PL spectra in a solid state. Adapted from ref. 120 with permission from Springer Nature, copyright 2022.

at 491 nm (green) (Fig. 14). An OLED device employing the macrocycle **226** emitter demonstrated superior electroluminescence performance compared to monomer **225**, achieving a 47% enhancement in maximum EQE (2.82% for **226** *vs.* 1.92% for **225**) and 84% higher peak brightness (4355 cd m^{-2} for **226** *vs.* 2369 cd m^{-2} for **225**).

In 2023, Wong and Chou reported a groundbreaking strategy for achieving highly efficient TADF in OLEDs through entropy-driven charge-transfer complexation.[113] The OLED device incorporating the **G10@206** complex displayed bright green electroluminescence (EL) with a main peak at 522 nm (Fig. 15a) and a full-width at half-maximum of 91 nm (at 4 V). It featured a low turn-on voltage (2.6 V) and a maximum EQE of 15.2% (at 4.2 V).

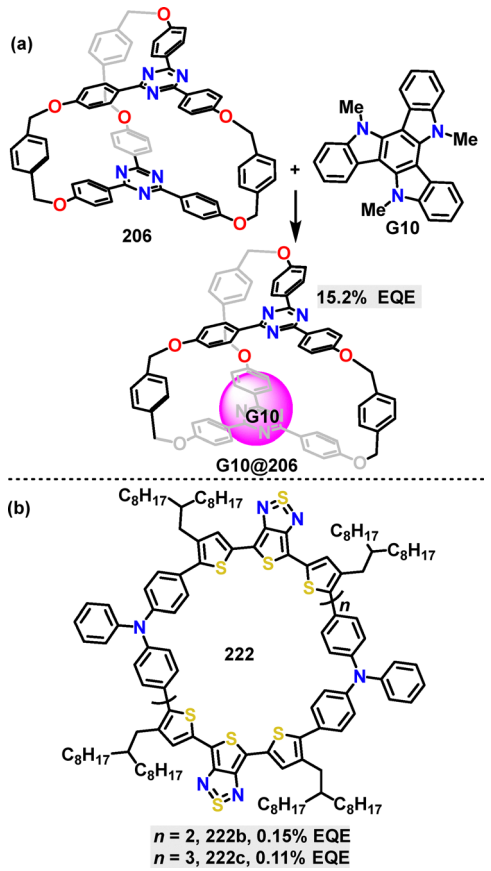

Fig. 15 (a) Structures of macrocycle **206**, **G10**, and the **G10@206** complex and (b) structures of macrocycles **222b–c**.

Recently, Yi, Wu and Wan reported the fabrication and characterization of near-infrared (NiR) OLEDs based on a series of D–A cyclic oligomers **222** (Fig. 15b).[118] Notably, OLEDs incorporating macrocycle **222b** achieved efficient NIR electroluminescence exceeding 900 nm, with an EQE of 0.15% and a high radiance of 2897 mW sr^{-1} m^{-2}. The **222c** device showed a slight red-shift at 907 nm and a higher maximum radiance of 2897 mW sr^{-1} m^{-2}, though with a lower EQE of 0.11%.

6.3.2. OFETs. In 2020, Lu, Wu, and Liu synthesized a novel saddle-shaped S-containing heterocycloarene **154**.[88] Consequently, the bottom-gate, bottom-contact (BGBC) OFET device of **154** (Fig. 16a) exhibited a hole mobility of 1.08×10^{-3} cm^2 V^{-1} s^{-1} and an on/off ratio of 5.6×10^3.

Later, Iyoda studied the OFET behavior of macrocyclic π-extended thiophene hexamers.[96] The OFET properties of these macrocycles showed a strong dependence on their structural planarity (Fig. 16b). For instance, macrocycle **172a** with a twisted geometry had a hole mobility of 1.2×10^{-5} cm^2 V s^{-1}, and macrocycle **172b** with an *E*,*Z*,*Z*,*Z* configuration had a hole mobility of 7.9×10^{-5} cm^2 V^{-1} s^{-1}. In contrast, **173**, featuring a

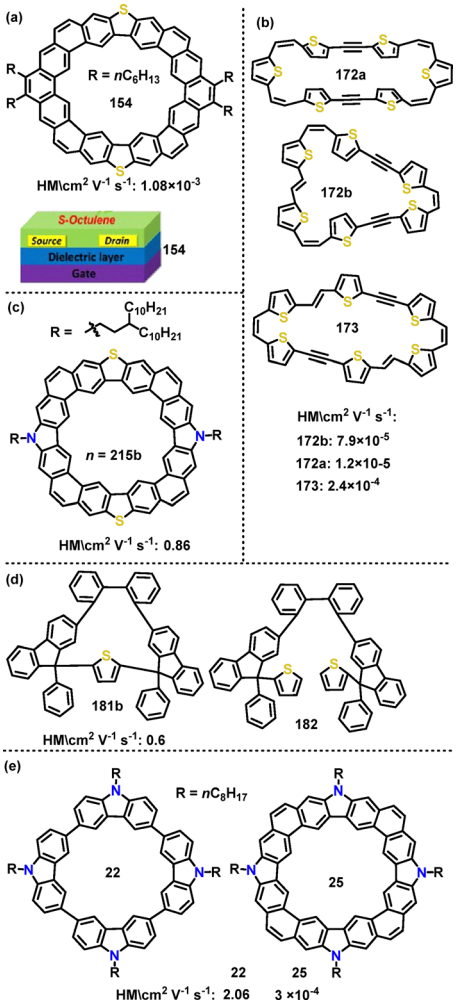

Fig. 16 Structures of macrocycles (a) **154**, (b) **172a**, **172b**, and **173**, (c) **215b**, (d) **181b** and **182**, (e) **22** and **25**. Reproduced from ref. 88 with permission from The Royal Society of Chemistry, copyright 2020.

rigid planar *E*,*Z*,*E*,*Z* structure, exhibited the highest mobility of 2.4×10^{-4} cm^2 V^{-1} s^{-1}, which can be attributed to its inherent columnar stacking. In 2022, Liu, Lu and Zhao designed and synthesized a novel series of N,S-embedded heterocycloarenes (Fig. 16c),[116] which featured a fully coplanar aromatic backbone. Notably, OFET devices incorporating **215b** exhibited an on/off current ratio of 10^7 and thermal stability up to 100 °C. Additionally, the charge carrier mobility of the N,S-embedded macrocycle **215b** (0.86 cm^2 V^{-1} s^{-1}) was significantly enhanced by two orders of magnitude compared to its S-embedded macrocycle **154** (1.08×10^{-3} cm^2 V^{-1} s^{-1}).[113] This stark contrast underscores how molecular geometry engineering effectively boosted charge carrier mobilities in organic semiconductors.

In 2023, Xie and Huang explored the application of a novel class of axially and centrally chiral A-type nanogrids in OFET memory devices (Fig. 16d).[99] OFET memory device measurements of **181b** revealed a significantly larger memory window (28.3 V) compared to **182** (12.7 V) and an on/off ratio over 10^4. This performance disparity was attributed to the rigid nanogrid architecture of **181b**, which enabled efficient electron/hole trapping through its well-defined chiral framework. In the same year, Zhao, Lu, and co-workers demonstrated a periphery fusion strategy to significantly enhance charge transport in OFET devices.[33] The device based on **25** displayed typical p-type characteristics with a maximum hole mobility (HM) of 2.06 cm^2 V^{-1} s^{-1} (Fig. 16e), which is four orders of magnitude higher than that of the device based on **22** (3×10^{-4} cm^2 V^{-1} s^{-1}). DFT calculations further indicated that both **22** and **25** possessed delocalized HOMO/LUMO distributions, highlighting their potential as p-type semiconductor materials.

6.3.3. OSCs. In 2021, Skabara, Samuel, and Cooke investigated the performance of thiophene-based conjugated macrocycle **224** in organic electronic devices (Fig. 17a), including bulk heterojunction (BHJ) OSCs.[119] Macrocycle **224** was employed as an electron donor in BHJ OSCs, which demonstrated a maximum power conversion efficiency (PCE) of 0.63%, highlighting the macrocycle's potential in low-bandgap photovoltaic materials. Later, Yuan presented a significant advancement in the use of cyclic thiophene-based conjugated molecules for photovoltaics (Fig. 17b).[117] Notably, OSCs fabricated with macrocycle **218** achieved a record-breaking (PCE) of 14.2%. The devices exhibited an EQE of up to 70% across the 400–800 nm spectral range, highlighting the macrocycle's exceptional optoelectronic performance and potential for advanced photovoltaic applications.

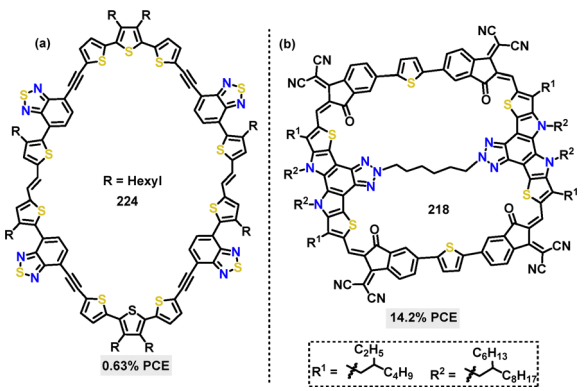

Fig. 17 Structures of macrocycles (a) **224** and (b) **218**.

6.4. Catalysis

In 2023, Kobayashi and Kumagai demonstrated the catalytic efficacy of complex **203**,[112] which exhibited high activity in the aziridination of styrene with (*N*-tosylimino)phenyliodinane (PhINTs), affording the corresponding aziridine in 99% yield (Fig. 18c). Although complex **203** showed negligible emission in solution, adding H_2O to its methanol solutions enhanced PL intensity with orange emission, indicative of AIE properties. In the solid state, the complex displayed strong emission (Em: 592 nm, PLQY: 21%) and long PL lifetimes (τ: 10–30 μs), suggesting phosphorescence *via* ISC facilitated by the Cu(I) cation.

Recently, Tang reported the construction of a novel supramolecular artificial light-harvesting system (ALHS) employing an AIE-active macrocycle **36** for applications in photocatalysis.[36] The emission spectra of **34** (460 nm) and **36** (450 nm) showed good overlap with the absorption profile of the orange-emitting acceptor **37**, enabling efficient Förster resonance energy transfer (FRET). In the **36**/**37** system, a one-step FRET process achieved an energy transfer efficiency (ETE) of 82.6% at a D/A ratio of 1000 : 40, outperforming the **34**/PBTB system with ETE 77.9%. Rigid macrocyclic **36**-based ALHSs exhibited significantly higher ETE (82.6%) compared to **34**-based counterparts. Notably, under white light irradiation, the **36**-based ALHSs demonstrated superior photocatalytic activity toward the cross-dehydrogenative coupling reaction in water, generating product **40** in 87% yield (Fig. 19b). In contrast, **34**-based systems showed substantially lower catalytic activity (36%), underscoring the structural advantage of macrocyclic architecture.

6.5. Molecular adsorption and separation

6.5.1. Molecular adsorption. In 2023, Wang, Jiang, and co-workers developed a novel class of Tröger Base-derived macrocycles **70a–b** and demonstrated their exceptional performance as adsorbents for iodine vapor capture.[48] In vapor-phase adsorption tests (Fig. 20), **70a** adsorbed up to 4.02 g g^{-1} (402 wt%), while **70b** achieved an adsorption capacity of 3.65 g g^{-1} (365 wt%). These

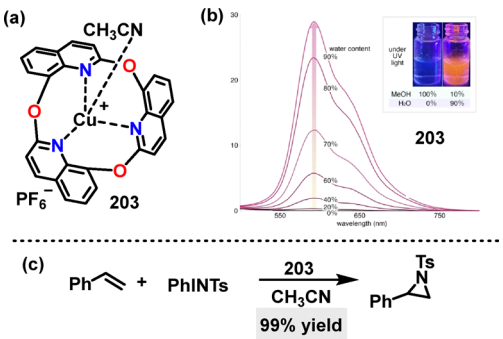

Fig. 18 (a) Structure of macrocycle **203**, (b) PL emission spectra of the **203** complexes in MeOH/H_2O, and (c) the catalytic activity of Cu-complex **203**. Adapted from ref. 112 with permission from Wiley-VCH, copyright 2023.

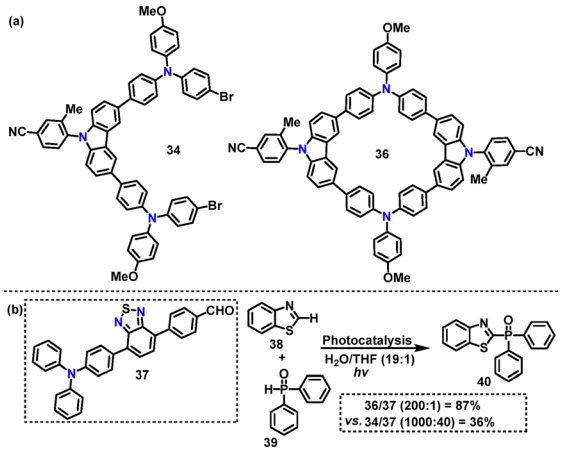

Fig. 19 (a) Structures of macrocycles **34**, **36**, and **37** and (b) a comparison of the catalytic performance for systems **34**/**37** and **36**/**37**.

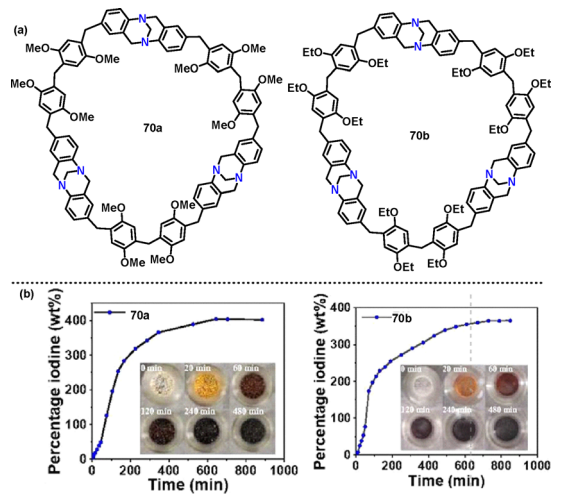

Fig. 20 (a) Structures of macrocycles **70a** and **70b**, and (b) their time-dependent iodine capture behaviours. Adapted from ref. 48 with permission from The Royal Society of Chemistry, copyright 2023.

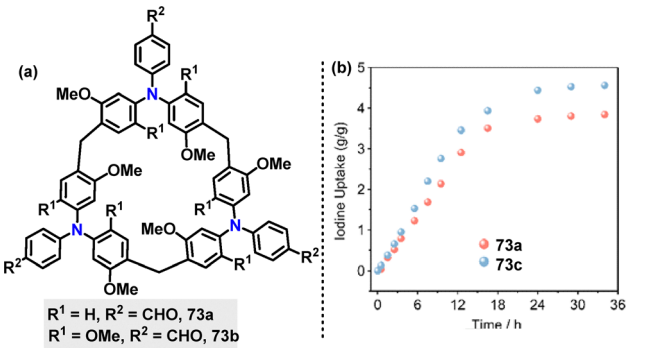

Fig. 21 (a) Structures of macrocycles **73a** and **73b**, and (b) their static iodine adsorption. Reprinted (naming of compounds adapted) with permission. Reproduced from ref. 49 with permission from Wiley-VCH, copyright 2024.

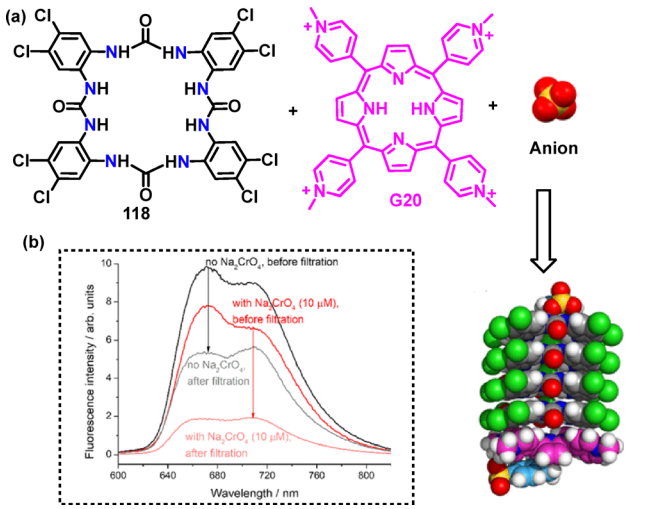

Fig. 22 (a) MD simulations of **118** co-assemblies with **G20**, and (b) fluorescence spectra of the solutions containing **118** and **G20** in the absence and presence of CrO_4^{2-}. Reproduced from ref. 64 with permission from American Chemical Society, copyright 2025.

values were significantly higher than those of many previously reported N-free macrocyclic adsorbents,[50,51] such as cyclotrixylohydroquinoylene derivatives, terphen[*n*]arenes, and quaterphen[*n*]arenes.

In 2024, Zhang, Zhao, Sue, and co-workers established triphenylamine[3]arene macrocycles **73a and b** as a highly efficient and versatile platform for iodine adsorption,[49] with their superior performance originating from the strong electron-donating character of the intrinsic triphenylamine (TPA) moieties. For example, at 343 K under ambient pressure, these materials achieved iodine uptake capacities of 3.74 and 4.44 g g^{-1} after 24 h, peaking at 3.85 and 4.56 g g^{-1} after 34 h (Fig. 21b). Over five days under ambient conditions, they showed gradual weight loss, indicating stable yet reversible interactions with iodine.

6.5.2. Molecular separation. In 2025, Gale, Wu, Félix and co-workers developed a novel supramolecular strategy for the molecular separation of toxic anions from water, using an ion-pair assembly **118–G20** composed of macrocycle **118** and **G20** (Fig. 22a).[64] The **118–G20** system exhibited pronounced binding affinity for anions such as CrO_4^{2-}, SO_4^{2-}, and Cl^-, with particularly strong interactions toward multicharged oxoanions. Notably, the assembly enabled the removal of CrO_4^{2-} from aqueous solutions at concentrations ranging from 2.5 to 20 μM, achieving efficiencies between 78% and 32% through simple syringe filtration (Fig. 22b).

Conclusion

In recent years, numerous innovative methods have emerged for the synthesis of heteroatom-doped macrocycles, which play a crucial role in organic chemistry, materials science, catalysis, and medicine. Techniques such as acid- or base-catalyzed cycloaddition and condensation reactions are commonly employed to construct macrocyclic frameworks. Transition metal-catalyzed cyclization reactions further facilitate the incorporation of

heteroatoms into macrocycles, thereby improving selectivity and yields. For example, Pd-catalyzed cross-coupling, Ni-catalyzed Yamamoto polymerization, Cu-mediated azide–alkyne cycloaddition, Fe-catalyzed cyclization, and other cyclization reactions have proven effective in synthesizing diverse complex heteroatom-doped macrocyclic compounds. These macrocycles exhibit unique physical and chemical properties due to heteroatom incorporation, which alters the electronic distribution within the macrocycle, thereby influencing its reactivity and stability. For instance, N-doped macrocycles are widely used as catalysts in organic synthesis, while the ability of nitrogen to interact with specific ions or small molecules enables the development of selective sensors. O-doped macrocycles can detect specific ions or small molecules (*e.g.*, heavy metals) through selective binding, making them effective tools for environmental monitoring. S-doped macrocycles have been employed in the development of advanced materials, such as OFETs and host–guest materials. Moreover, the presence of polar heteroatoms often enhances solubility in various solvents, increasing their versatility in applications such as the construction of metal–organic frameworks (MOFs)/covalent organic frameworks (COFs), optoelectronic devices, sensing, and drug delivery.

To propel the field of heteroatom-doped macrocycles forward, the development of more efficient, selective, and general synthetic strategies is of critical importance. This necessitates a concerted effort to overcome three primary challenges, including enantioselective synthesis, generality and structural diversity, and scalability and efficiency. (1) The construction of well-defined chiral macrocycles remains a significant bottleneck, limiting applications in asymmetric catalysis, enantioselective sensing, and chiroptical materials. Pioneering catalytic asymmetric macrocyclization strategies, such as synergistic systems combining transition metals (*e.g.*, Pd, Cu, and Ni) with chiral ligands or organocatalysts, are essential to achieve precise stereochemical control. (2) Achieving greater structural diversity and expanding substrate scope will rely on transformative methods, such as photoredox-mediated annulations for novel bond formation, and the strategic use of multicomponent reactions (*e.g.*, A^3-coupling and Ugi reaction) in macrocyclization. (3) To truly transition these molecules from the laboratory stage to industrially relevant materials, synthetic routes must be fundamentally optimized for yield and scalability. Integrating robust catalytic methods, continuous-flow processes, and other process intensification techniques will be vital for enabling large-scale production and unlocking their full practical application potential.

The advancement of innovative synthetic methodologies will be the key to unlocking a new generation of applications that fully leverage the unique properties of heteroatom-doped macrocycles. Their well-defined, functionalized cavities position them as ideal platforms for supramolecular catalysis and biomimetics, enabling the design of artificial enzymes and catalysts for high-selectivity transformations under mild conditions. Concurrently, these macrocycles are emerging as essential components in advanced functional materials, such as those for molecular separation, organic electronics, and stimuli-responsive membranes, where their tunable host–guest chemistry and porosity can be precisely exploited. Furthermore, their tailored biocompatibility, molecular recognition capabilities, and unique spectroscopic signatures open significant avenues in biomedical translation, including targeted drug delivery, biosensing, and bioimaging, thereby creating a vital bridge between supramolecular chemistry and biomedical science.

In conclusion, developing new synthetic strategies for heteroatom-doped macrocycles, paired with rigorous property and application studies, will drive progress in supramolecular chemistry, catalysis, biology, and materials science. We anticipate that this review will offer valuable insights and directions for researchers navigating these interdisciplinary Frontiers.

Author contributions

Writing (original draft): CL, SL, XC and TY; writing (reviewing and editing): YW, LX, EVVdE and WH; funding acquisition: CL, YW, LX, EVVdE and WH; the final manuscript has been read and approved by all authors.

Conflicts of interest

There are no conflicts to declare.

Data availability

Data sharing is not applicable to this article as no new data were generated or analyzed in this review.

Acknowledgements

This work was supported by the Natural Science Research Start-up Foundation of Recruiting Talents of Nanjing University of Posts and Telecommunications (Grant No. NY224034; recipient CL, writing), the National Key R&D Program of China (Grant No. 2024YFB361260; recipient LX, writing), the National Natural Science Foundation of China (22275098, 62288102 and 22071112; recipients YW, LX, and WH, writing), and the Basic Research Program of Jiangsu (BK20243057; recipient LX, writing). The authors acknowledge the FWO [Fund for Scientific Research-Flanders (Belgium)] for financial support (recipient EVVdE, writing) and the Research Council of the KU Leuven (recipient EVVdE, writing). This paper has been prepared with the support of the "RUDN University Strategic Academic Leadership Program" (recipient EVVdE, writing).

Notes and references

1 S. Zhang, S. Fan, H. He, J. Zhu, L. Murray, G. Liang, S. Ran, Y. Zhu, M. J. Cryle, H.-Y. He and Y. Zhang, *Chem. Soc. Rev.*, 2025, **54**, 396–464.
2 X. Q. Ma, H. P. Xiao, Y. Chen, Q. S. Lai, X. X. Li and S. T. Zheng, *Coord. Chem. Rev.*, 2024, **510**, 215818.
3 K. T. Mortensen, T. J. Osberger, T. A. King, H. F. Sore and D. R. Spring, *Chem. Rev.*, 2019, **119**, 10288–10317.

4 X. Y. Lou, S. Zhang, Y. Wang and Y. W. Yang, *Chem. Soc. Rev.*, 2023, **52**, 6644–6663.
5 H. T. Feng, Y. X. Yuan, J. B. Xiong, Y. S. Zheng and B. Z. Tang, *Chem. Soc. Rev.*, 2018, **47**, 7452–7476.
6 C. D. Zhao, H. Yao, S. Y. Li, F. Du, L. L. Wang and L. P. Yang, *Chin. Chem. Lett.*, 2024, **35**, 108879.
7 Q. Feng, S. Zhu, B. Wang, F. Yu, H. Li, M. Yu, M. Xu and L. Xie, *Adv. Funct. Mater.*, 2024, **34**, 2312622.
8 X. N. Han, Y. Han and C. F. Chen, *Chem. Soc. Rev.*, 2023, **52**, 3265–3298.
9 R. Paolesse, S. Nardis, D. Monti, M. Stefanelli and C. Di Natale, *Chem. Rev.*, 2017, **117**, 2517–2583.
10 R. Kumar, A. Sharma, H. Singh, P. Suating, H. S. Kim, K. Sunwoo, I. Shim, B. C. Gibb and J. S. Kim, *Chem. Rev.*, 2019, **119**, 9657–9721.
11 S. Bleus and W. Dehaen, *Coord. Chem. Rev.*, 2024, **509**, 215762.
12 C. D. Gutsche, *Calixarenes: An Introduction*, Royal Society of Chemistry, Cambridge, UK, 1989.
13 G. W. Gokel, W. M. Leevy and M. E. Weber, *Chem. Rev.*, 2004, **104**, 2723–2750.
14 Z. Q. Wang, X. Wang and Y. W. Yang, *Adv. Mater.*, 2024, **36**, 2301721.
15 J. R. Wu, G. Wu and Y. W. Yang, *Acc. Chem. Res.*, 2022, **55**, 3191–3204.
16 Z. Liu and Y. Liu, *Chem. Soc. Rev.*, 2022, **51**, 4786–4827.
17 M. Votava and B. J. Ravoo, *Chem. Soc. Rev.*, 2021, **50**, 10009–10024.
18 Y. Li, H. Kono, T. Maekawa, Y. Segawa, A. Yagi and K. Itami, *Acc. Mater. Res.*, 2021, **2**, 681–691.
19 T. M. Fukunaga, C. Sawabe, T. Matsuno, J. Takeya, T. Okamoto and H. Isobe, *Angew. Chem., Int. Ed.*, 2021, **60**, 19097–19101.
20 Y. Wu, S. Li, H. Li, R. Ye and Z. Lu, *J. Mater. Chem. C*, 2023, **11**, 7144–7158.
21 Y. Qin, X. Liu, P. P. Jia, L. Xu and H. B. Yang, *Chem. Soc. Rev.*, 2020, **49**, 5678–5703.
22 M. Toganoh and H. Furuta, *Chem. Rev.*, 2022, **122**, 8313–8437.
23 H. Lu and N. Kobayashi, *Chem. Rev.*, 2016, **116**, 6184–6261.
24 M. D. Tomczyk, N. Kuźnik and K. Walczak, *Coord. Chem. Rev.*, 2023, **481**, 215047.
25 Y. Matano and H. Imahori, *Acc. Chem. Res.*, 2009, **42**, 1193–1204.
26 R. Sengupta, M. Ravikanth and T. K. Chandrashekar, *Chem. Soc. Rev.*, 2021, **50**, 13268–13320.
27 P. Li, D. Shimoyama, N. Zhang, Y. Jia, G. Hu, C. Li, X. Yin, N. Wang, F. Jäkle and P. Chen, *Angew. Chem., Int. Ed.*, 2022, **61**, e202200612.
28 B. S. Kumar, B. Chandra, K. V. Jovan Jose and P. K. Panda, *J. Org. Chem.*, 2021, **86**, 10536–10543.
29 S. Shikita, G. Watanabe, D. Kanouchi, J. Saito and T. Yasuda, *Adv. Photonics Res.*, 2021, **2**, 2100021.
30 M. Zhao, S. H. Pun, Q. Gong and Q. Miao, *Angew. Chem., Int. Ed.*, 2021, **60**, 24124–24130.
31 T. Komori, E. Tsurumaki and S. Toyota, *Chem. – Asian J.*, 2023, **18**, e202201003.
32 H. Li, X. Zhang, J. Peng, S. Yang, R. Hu and X. Jiang, *J. Mater. Chem. C*, 2024, **12**, 10127–10134.
33 N. Zhang, W. Li, J. Zhu, T. Wang, R. Zhang, K. Chi, Y. Liu, Y. Zhao and X. Lu, *Adv. Mater.*, 2023, **35**, 2300094.
34 F. F. Wang, Y. X. Wang, Q. Wu, L. Chai, X. W. Chen and Y. Z. Tan, *Angew. Chem., Int. Ed.*, 2024, **136**, e202315302.
35 Y. Shi, X. Li, J. Di, Y. Xue, N. Zhang, T. Jin, C.-F. Chen and P. Chen, *CCS Chem.*, 2025, **7**, 1–17.
36 J. C. Yang, K. Chen, G. L. Zhang, C. Qi, H. T. Feng and B. Z. Tang, *Chem. Sci.*, 2025, **16**, 4741–4748.
37 S. Izumi, H. F. Higginbotham, A. Nyga, P. Stachelek, N. Tohnai, P. D. Silva, P. Data, Y. Takeda and S. Minakata, *J. Am. Chem. Soc.*, 2020, **142**, 1482–1491.
38 F. Picini, S. Schneider, O. Gavat, A. Vargas Jentzsch, J. Tan, M. Maaloum, J.-M. Strub, S. Tokunaga, J.-M. Lehn, E. Moulin and N. Giuseppone, *J. Am. Chem. Soc.*, 2021, **143**, 6498–6504.
39 J. Ayuso-Carrillo, F. Fina, E. C. Galleposo, R. R. Ferreira, P. K. D. Mondal, B. D. Ward and D. Bonifazi, *J. Am. Chem. Soc.*, 2024, **146**, 16440–16457.
40 H. Zhu, I. Badía-Domínguez, B. Shi, Q. Li, P. Wei, H. Xing, M. C. R. Delgado and F. Huang, *J. Am. Chem. Soc.*, 2021, **143**, 2164–2169.
41 Y. Yoshigoe, H. Shimada, T. Takaki, Y. Imai and S. Saito, *Chem. – Eur. J.*, 2024, **30**, e202304059.
42 C. Brouillac, N. McIntosh, B. Heinrich, O. Jeannin, O. De Sagazan, N. Coulon, J. Rault-Berthelot, J. Cornil, E. Jacques, C. Quinton and C. Poriel, *Adv. Sci.*, 2024, **11**, 2309115.
43 H. Zhang, H. Li, S. Sun, L. Tan, H. Shen, B. Lin and P. Yang, *Org. Lett.*, 2023, **25**, 2078–2083.
44 F. Zhang, X. S. Du, D. W. Zhang, Y. F. Wang, H. Y. Lu and C. F. Chen, *Angew. Chem., Int. Ed.*, 2021, **60**, 15291–15295.
45 Y. Li, Y. Segawa, A. Yagi and K. Itami, *J. Am. Chem. Soc.*, 2020, **142**, 12850–12856.
46 H. Y. Zhou, D. W. Zhang, X. N. Han, Y. Han and C. F. Chen, *Chem. Commun.*, 2022, **58**, 12180–12183.
47 F. Zeng, L. L. Tang, M. H. Ding and W. Dessie, *Org. Lett.*, 2023, **25**, 6290–6294.
48 P. Niu, C. Shi, J. Jiao, W. Xie, H. Qiu, Z. Yang, J. Jiang and L. Wang, *Chem. Commun.*, 2023, **59**, 10960–10963.
49 J. Jiao, W. Xie, Y. Li, C. Lin, J. Jiang and L. Wang, *Chem. – Eur. J.*, 2022, **28**, e202201933.
50 B. Li, B. Wang, X. Huang, L. Dai, L. Cui, J. Li, X. Jia and C. Li, *Angew. Chem., Int. Ed.*, 2019, **131**, 3925–3929.
51 W. Fang, J. Zhang, M. Guo, Y. Zhao and A. C. H. Sue, *Angew. Chem., Int. Ed.*, 2024, **63**, e202409120.
52 Y. Liu, H. Wang, P. Liu, H. Zhu, B. Shi, X. Hong and F. Huang, *Angew. Chem., Int. Ed.*, 2021, **133**, 5830–5834.
53 A. Kalaiselvan, I. S. Vamsi Krishna, A. P. Nambiar, A. Edwin, V. S. Reddy and S. Gokulnath, *Org. Lett.*, 2020, **22**, 4494–4499.
54 D. Lin, Y. Wei, A. Peng, H. Zhang, C. Zhong, D. Lu, H. Zhang, X. Zheng, L. Yang, Q. Feng, L. H. Xie and W. Huang, *Nat. Commun.*, 2020, **11**, 1756.
55 G. Ouyang, J. Rühe, Y. Zhang, M. J. Lin, M. Liu and F. Würthner, *Angew. Chem., Int. Ed.*, 2022, **134**, e202206706.
56 H. Chen, X. Shi, Y. Lun, Y. Xu, T. Lu, Z. Duan, M. Shao, J. L. Sessler, C. Yu and H. Lei, *J. Am. Chem. Soc.*, 2022, **144**, 8194–8203.

57 N. Halder, R. Naryanasamy, D. Usharani and H. Rath, *Org. Chem. Front.*, 2022, **9**, 2333–2342.
58 J. Q. Zhao, L. L. Mao, G. H. Zhang, S. Z. Zhan, H. Xiao, S. Zhang, C. H. Tung, L. Z. Wu and H. Cong, *J. Mater. Chem. A*, 2023, **11**, 4672–4678.
59 S. Li, C. Zhu, L. Mao, X. Zhang, Z. Ye, C. Li and D. Ma, *Sci. China: Chem.*, 2025, **68**, 3116–3122.
60 Y. Shen, X. Liang, T. Ma, D. Zhou, W. Li, J. Ma, J. Ma, W. Wu, Z. Yu and C. Yang, *Angew. Chem., Int. Ed.*, 2025, **137**, e202504211.
61 S. X. Nie, H. Guo, T. Y. Huang, Y. F. Ao, D. X. Wang and Q. Q. Wang, *Nat. Commun.*, 2020, **11**, 6257.
62 Y. X. Yuan, J. H. Jia, Y. P. Song, F. Y. Ye, Y. S. Zheng and S. Q. Zang, *J. Am. Chem. Soc.*, 2022, **144**, 5389–5399.
63 K. Kihara, T. Kobayashi, W. Xu and N. Kumagai, *Chem. – Eur. J.*, 2024, **30**, e202304176.
64 J. Li, O. Catal, I. Marques, D. A. McNaughton, R. M. Maklad, W. G. Ryder, M. J. S. Hill, A. Seddo, W. Lewis, D. J. Adams, V. Félix, X. Wu and P. A. Gale, *J. Am. Chem. Soc.*, 2025, **147**, 3392–3401.
65 H. Keypour, M. Abdollahi-Moghadam, H. Zeynali, R. Karamian and N. B. Hamedani, *J. Mol. Struct.*, 2024, **1295**, 136803.
66 R. Singla, A. Ganguli and M. Ghosh, *Int. J. Food Prop.*, 2010, **13**, 1290–1299.
67 N. Prusinowska, A. Czapik, J. Szymkowiak and M. Kwit, *Sci. Rep.*, 2025, **15**, 890.
68 S. Xiong, Y. Zhang, Y. Jiang, F. Wang, W. Zhou, A. Li, Q. Zhang, Q. Wang and Q. He, *Chem. Commun.*, 2023, **59**, 12994–12997.
69 S. K. M. Nalluri and J. F. Stoddart, *Chem. Soc. Rev.*, 2017, **46**, 2459–2478.
70 C. J. Pedersen, *J. Am. Chem. Soc.*, 1967, **89**, 2495–2496.
71 C. J. Pedersen, *J. Am. Chem. Soc.*, 1967, **89**, 7017–7036.
72 G. W. Gokel, L. J. Barbour, L. Stephen and E. S. Meadows, *Coord. Chem. Rev.*, 2001, **222**, 127–154.
73 A. J. Varni, M. Kawakami, S. A. Tristram-Nagle, D. Yaron, T. Kowalewski and K. J. Noonan, *Org. Chem. Front.*, 2021, **8**, 1775–1782.
74 S. V. Mulay, O. Dishi, Y. Fang, M. R. Niazi, L. J. W. Shimon, D. F. Perepichka and O. Gidron, *Chem. Sci.*, 2019, **10**, 8527–8532.
75 T. Köhler, D. Seidel, V. Lynch, F. O. Arp, Z. Ou, K. M. Kadish and J. L. Sessler, *J. Am. Chem. Soc.*, 2003, **125**, 6872–6873.
76 Y. Han, W. C. Guo, X. S. Du and C. F. Chen, *Chem. Commun.*, 2024, **60**, 5719–5722.
77 X. S. Du, D. W. Zhang, Y. Guo, J. Li, Y. Han and C. F. Chen, *Angew. Chem., Int. Ed.*, 2021, **60**, 13021–13028.
78 F. Zhang, X. S. Du, D. W. Zhang, Y. F. Wang, H. Y. Lu and C. F. Chen, *Angew. Chem., Int. Ed.*, 2021, **60**, 15291–15295.
79 D. Zhu, S. Fang, L. Tong, Y. Lei, G. Wu, T. Chudhary and H. Li, *Chem. Commun.*, 2021, **57**, 4440–4443.
80 K. Xu, B. Li, S. Yao, Z. Li, Y. Lu, M. Dong, J. Qiu, L. Luo and C. Li, *Angew. Chem., Int. Ed.*, 2022, **134**, e202203016.
81 J. Pfeuffer-Rooschuz, L. Schmid, A. Prescimone and K. Tiefenbacher, *JACS Au*, 2021, **1**, 1885–1891.
82 Y. F. Wang, H. Yao, L. P. Yang, M. Quan and W. Jiang, *Angew. Chem., Int. Ed.*, 2022, **134**, e202211853.
83 Y. Gong, S. Fang, Y. Zheng, H. Guo and F. Yang, *J. Photochem. Photobiol., A*, 2023, **435**, 114307.
84 Y. Liu, Q. Zhang, S. Crespi, S. Chen, X. K. Zhang, T. Y. Xu, C. S. Ma, S. W. Zhou, Z. T. Shi, H. Tian, B. L. Feringa and D. H. Qu, *Angew. Chem., Int. Ed.*, 2021, **133**, 16265–16274.
85 C. Gagnon, É. Godin, C. Minozzi, J. Sosoe, C. Pochet and S. K. Collins, *Science*, 2020, **367**, 917–921.
86 T. Yang, T. Wang, F. Deng, S. Ma, F. Yang, Y. Wei, C. Zhong and L. Xie, *Sci. Bull.*, 2025, **70**, 1902–1906.
87 A. Jana, S. Bähring, M. Ishida, S. Goeb, D. Canevet, M. Sallé, J. O. Jeppesen and J. L. Sessler, *Chem. Soc. Rev.*, 2018, **47**, 5614–5645.
88 L. Yang, N. Zhang, Y. Han, Y. Zou, Y. Qiao, D. Chang, Y. Zhao, X. Lu, J. Wu and Y. Liu, *Chem. Commun.*, 2020, **56**, 9990–9993.
89 X. Lu, D. An, Y. Han, Y. Zou, Y. Qiao, N. Zhang, D. Chang, J. Wu and Y. Liu, *Chem. Sci.*, 2021, **12**, 3952–3957.
90 D. An, R. Zhang, J. Zhu, T. Wang, Y. Zhao, X. Lu and Y. Liu, *Chem. Sci.*, 2024, **15**, 4590–4601.
91 L. Zhan, C. Dai, G. Zhang, J. Zhu, S. Zhang, H. Wang, Y. Zeng, C. H. Tung, L. Z. Wu and H. Cong, *Angew. Chem., Int. Ed.*, 2022, **61**, e202113334.
92 T. C. Lovell, Z. R. Garrison and R. Jasti, *Angew. Chem., Int. Ed.*, 2020, **59**, 14363–14367.
93 C. Zhao, F. Liu, L. Feng, M. Nie, Y. Lu, J. Zhang, C. Wang and T. Wang, *Nanoscale*, 2021, **13**, 4880–4886.
94 L. Ren, Y. Han, X. Hou, Y. Ni, Y. Zou, T. Jiao and J. Wu, *J. Am. Chem. Soc.*, 2023, **145**, 12398–12406.
95 M. Nagase, S. Nakano and Y. Segawa, *Chem. Commun.*, 2023, **59**, 11129–11132.
96 K. Shirahata, M. Takashika, K. Hirabayashi, M. Hasegawa, H. Otani, K. Yamamoto, Y. Le, T. Shimizu, A. Shinobu and M. Iyoda, *J. Org. Chem.*, 2020, **86**, 302–309.
97 T. M. Fukunaga, C. Sawabe, T. Matsuno, J. Takeya, T. Okamoto and H. Isobe, *Angew. Chem., Int. Ed.*, 2021, **60**, 19097–19101.
98 M. Lin, L. Bian, Q. Chen, H. Xu, Z. Liu and K. Zhu, *Angew. Chem., Int. Ed.*, 2023, **62**, e202303035.
99 Y. Wei, X. Du, W. X. Huang, M. Y. Fu, Z. Zhang, C. X. Zhong, Y. Wang, H. F. Ling, L. H. Xie and W. Huang, *Chin. J. Chem.*, 2023, **41**, 2969–2974.
100 S. I. Etkind, S. Ichii, N. A. Romero and T. M. Swager, *Synlett*, 2022, 1532–1538.
101 A. Ovsyannikov, S. Solovieva, I. Antipin and S. Ferlay, *Coord. Chem. Rev.*, 2017, **352**, 151–186.
102 X. Sun, J. Bai, X. Y. Wang and H. Y. Gong, *Coord. Chem. Rev.*, 2024, **518**, 216063.
103 A. M. Camp, M. R. Kita, P. T. Blackburn, H. M. Dodge, C. H. Chen and A. J. Miller, *J. Am. Chem. Soc.*, 2021, **143**, 2792–2800.
104 C. H. Wei, S. Dong, Z. Xu, M. Li, T. Zhang, Z. Xu, M. Li, T. Zhang, Z. Xu, S. Lan, S. Wang and L. Mao, *Angew. Chem., Int. Ed.*, 2024, **63**, e202412253.
105 J. F. Stoddart, A Platform for Change, *Supramol. Chem.*, 2015, **27**, 567–570.

106 P. K. Kodali, S. Choppella, D. Kumar, U. K. Pandey, M. K. Ravva and S. P. Singh, *Chem. Commun.*, 2024, **60**, 11726–11729.
107 H. Zhou, Y. Zhang, Z. Zheng, J. Wan, H. Zhang, K. Lin, J. L. Sessler and H. Wang, *Chem. Sci.*, 2025, **16**, 910–919.
108 L. Mao, F. Li, L. Huang, X. Qu, K. Wang, Y. Zhang and D. Ma, *Org. Lett.*, 2023, **25**, 5597–5601.
109 L. Wang, Y. Zhang, J. Chen, S. Jongaksorn, Z. Lu, X. Zhang, S. Li, C. Zhu, D. Ma and L. Mao, *J. Org. Chem.*, 2025, **90**, 1671–1677.
110 S. Y. Zhuang, Y. Cheng, Q. Zhang, S. Tong and M. X. Wang, *Angew. Chem., Int. Ed.*, 2020, **132**, 23924–23931.
111 I. Solymosi, S. Krishna, E. Nuin, H. Maid, B. Scholz, D. M. Guldi, M. E. Pérez-Ojeda and A. Hirsch, *Chem. Sci.*, 2021, **12**, 15491–15502.
112 T. Kobayashi and N. Kumagai, *Angew. Chem., Int. Ed.*, 2023, **135**, e202307896.
113 C. Y. Lin, C. H. Hsu, C. M. Hung, C. C. Wu, Y. H. Liu, E. H. C. Shi, T. H. Lin, Y. C. Hu, W. Y. Hung, K. T. Wong and P. T. Chou, *Nat. Chem.*, 2024, **16**, 98–106.
114 D. Hartmann, S. E. Penty, M. A. Zwijnenburg, R. Pal and T. A. Barendt, *Angew. Chem., Int. Ed.*, 2025, **64**, e202501122.
115 F. Wang, X. Shi, Y. Zhang, W. Zhou, A. Li, Y. Liu, J. L. Sessler and Q. He, *J. Am. Chem. Soc.*, 2023, **145**, 10943–10947.
116 N. Zhang, L. Yang, W. Li, J. Zhu, K. Chi, D. Chang, Y. Qiao, T. Wang, Y. Zhao, X. Lu and Y. Liu, *J. Am. Chem. Soc.*, 2022, **144**, 21521–21529.
117 W. Liu, H. Zhang, S. Liang, T. Wang, S. He, Y. Hu, R. Zhang, H. Ning, J. Ren, A. Bakulin, F. Gao, Y. Jun and Y. Zou, *Angew. Chem., Int. Ed.*, 2023, **62**, e202311645.
118 W. Zhang, W. Liu, Z. Xu, K. An, Q. H. Li, Z. Wang, P. Lei, Q. Zeng, N. Li, Y. P. Yi, H. Wu and J. H. Wan, *Adv. Funct. Mater.*, 2024, **34**, 2411745.
119 J. M. dos Santos, L. K. Jagadamma, J. Cameron, A. A. Wiles, C. Wilson, P. J. Skabara, I. D. W. Samuel and G. Cooke, *J. Mater. Chem. C*, 2021, **9**, 16257–16271.
120 S. Li, K. Liu, X. C. Feng, Z. X. Li, Z. Y. Zhang, B. Wang, M. Li, Y. L. Bai, L. Cui and C. Li, *Nat. Commun.*, 2022, **13**, 2850.
121 G. Kaur, N. Rawat and M. Ravikanth, *J. Org. Chem.*, 2023, **88**, 14989–14997.
122 G. Zhang, F. Chen, Y. Di, S. Yuan, Y. Zhang, X. Quan, Y. Chen, H. Chen and M. Lin, *Adv. Funct. Mater.*, 2024, **34**, 2404123.
123 J. Ajay, T. Sulfikarali, A. Edwin, M. Sasi, S. Mori and S. Gokulnath, *Org. Lett.*, 2025, **27**, 2128–2132.
124 Z. Lu, W. Lv, H. Liu, Y. Liu, S. Liao, X. Wang and K. Zhu, *Org. Lett.*, 2023, **25**, 3508–3511.
125 K. Bold, M. Stolte, K. Shoyama, M. Holzapfel, A. Schmiedel, C. Lambert and F. Würthner, *Angew. Chem., Int. Ed.*, 2022, **61**, e202113598.